Measuring Photometric and Spectral Radiometric Bi-directional Transmission and Reflection in a Video-goniospectrometer

Eleanor Stokes

A.B. Math and Studio Art (2004)
Dartmouth College

Submitted to the Department of Mechanical Engineering
in Partial Fulfillment of the Requirements for the Degree of
Master of Science in Mechanical Engineering

at the
Massachusetts Institute of Technology

June 2008

Signature of author..
Department of Mechanical Engineering
May 9, 2007

Certified by..
Dr. Marilyne Andersen
Assistant Professor of Building Technology
Thesis Supervisor

Certified by..
Leon R. Glicksman
Professor of Building Technology and Mechanical Engineering
Thesis Reader

Accepted by..
Lallit Anand
Graduate Committee Chairman
Department of Mechanical Engineering

Measuring Photometric and Spectral Radiometric Bi-directional Transmission and Reflection in a Video Goniospectrometer

by
Eleanor Stokes

Submitted to the Department of Mechanical Engineering on May 9, 2008
in Partial Fulfillment of the Requirements for the Degree of
Master of Science in Mechanical Engineering
at the Massachusetts Institute of Technology

Acknowledgements

I would like to thank my advisor, Dr. Marilyne Andersen, for her support, infectious optimism, and deep knowledge and guidance.

I would also like to thank Nick Gayeski for all of his collaboration and his continued generous dedication to this project.

Thank you to the other daylighting Illuminati, especially Jason Ku, Javier Burgos, Dan Vo, Keith Molina, and Samuel Kronick, for their valuable work on the mechanical, electrical, and computer programming components of the Heliodome.

Also thank you to Mark Schuetz at Replex Plastics for his work forming and coating the final spheroid.

To Mike Rubin, from Lawrence Berkley National Lab, for providing sample glazing materials and guiding the direction of the Heliodome project.

I am also very grateful to Professor Alan Edelman, Chad Lieberman, and all of the 18.337 spring term students for their critical and timely parallel processing assistance.

And a special thanks to all of the professors and students of the Building Technology Group for their invaluable insights and interest in this project. Especially to Leon Glicksman for reviewing this work and offering constructive feedback.

Finally, thanks to my friends for their flexibility, humor, and patience with my late night rantings about spheroidal geometry. And to my family, who always lovingly supports me in every endeavor--especially to my father, for his critical eye, and my mother, for her unconditional advocacy. Finally, I am most grateful for God's ample provision of joys, challenges, and growth in regard to this research over the past two years.

This thesis work was supported by Lambda Research Corporation, whose donation of TracePro licenses enabled much of the analysis and graphics included in this document.

The Heliodome project and this research endeavor was jointly funded by the Massachusetts Institute of Technology and the National Science Foundation under Grant No. 0533269. Any opinions, findings, and conclusions or recommendations expressed in this material are those of the author(s) and do not necessarily reflect the views of the National Science Foundation (NSF).

Abstract

The effective use of complex fenestration systems (CFS) in buildings requires a detailed knowledge of their optical spectral and directional properties. Bidirectional scattering functions (BSDFs), either in transmission (BTDFs) or reflection (BRDFs), are used to assess these properties and gather information vital to CFS design and analysis.

To enable this analysis in a time and budget conscious manner, an innovative video goniospectrometer, called the Heliodome, has been developed. The Heliodome relies on filtered digital imaging, mathematical methods, and the use of a unique semi-transparent hemispheroidal light collection system to investigate the spectral and angular selectivity of CFS across the visible and near infrared portions of the solar spectrum.

This thesis seeks to describe the most recent advancements in the development of the Heliodome—the completion and characterization of the spheroidal mirror component, the integration of a spectral estimation method, the photometric calibration of the camera, and the final automation and validation-- enabling the measurement of both spectral radiometric BSDFs and photometric BSDFs. The completion of this research should support the advancement of CFS that improve the use of daylighting in a space, reducing energy consumption and managing solar gains while improving visual comfort in buildings.

Thesis supervisor: Marilyne Andersen, Assistant Professor of Building Technology

Contents

8. Validation

List of Figures

Chapter 2

Chapter 3

Chapter 4

Chapter 5

Chapter 6

Chapter 7

Chapter 8

Appendix A

List of Tables

Chapter 5

Chapter 8

Appendix B

1. Introduction

The architectural tradition grew out of an era when daylighting was the only clean and safe means for illumination. As proves true with many design trends, the relationship between natural illumination and architectural form was most intimate when there was no competing lighting technology. In his article *Electrician*, Sir Joseph Swan, the developer of the electric lamp, marvels at the advancements since the days of his youth, when "the rushlight, the tallow dip or the solitary blaze of the hearth were the common means of indoor lighting" (Swan 1893). However, it wasn't until fifty years later in the 1950s and 60s when the full momentum of artificial lighting would dominate design movements. Daylighting would begin to be seen as a heating and cooling liability, with some states even abandoning minimum illumination requirements in their lighting codes (Heschong 2002a).

The solar-apathetic design trends of forty years ago are a far cry from the accepted architectural ideal of today. Premiums are paid for well-daylit spaces, and abundant glazing has become a design status symbol in modern architecture. Certainly, this switch signifies a rejection of the artificial lighting rhetoric and a fervent mandate for naturally-lit spaces.

1.1 Daylighting Benefits

Society has extensively profited from the rediscovery of daylight and its celebration in design. The following section overviews some of the findings on the benefits of daylight for psychological and physiological health, for addressing energy and economic concerns, and for architectural expression.

1.1.1 Psychological and Physiological Benefits

Certainly the most intuitive use of light is for vision. It is well known how lighting conditions can impact our sight, and thus our ability to perform visual tasks. In fact, through a model of vision performance (Rea and Ouellette 1991), the ability to perform a certain visual task can be predicted very accurately depending on target size, target contrast, observer age, and illuminance levels.

The effect of different light spectra on visual task performance has also been studied extensively. A light's emittance spectrum is known to effect visual performance when luminance contrasts are low (Eklund 1999), or, more obviously, in chromacity-dependent tasks (Williams, 1966). Other data suggests that light spectra that produce small pupil sizes improve retinal image quality for tasks close to the visual threshold (Boyce et. al 2003b). At the very least, it is accepted that color temperature alters the average value of preferred illuminance level on a task plane (Kruithoff 1941).

Because the link between light and vision is so predictable, it is easy to assess daylight as a means of illumination. As illuminance optimality depends on the task, in some cases, daylight can enhance performance, while in other tasks it may diminish performance. Most visual tasks, though, are performed better in high illumination. While these levels can usually be achieved with artificial lighting, electrically lit spaces often target the minimum task-based illumination levels as a result of lighting codes and economics. Thus, inadvertently, daylit spaces often achieve a higher level of illumination than electrically lit buildings (Leslie 2003), often aiding in visual performance.

Additionally, one of the characteristics that makes daylight such a tough lighting competitor is its broad spectral range. The spectral power distribution of daylight covers the entire visible spectrum, affording better color rendering than most artificial lighting. In fact, daylight is often used in art galleries and high-end retail stores for this purpose. This broad spectrum also improves some task performance, as subjects perform better in fine color discrimination tasks or in discrimination of low levels of color contrast when they are tested in daylit spaces (Nickerson 1948, ASTM 1996, Williams 1966, Eklund 1999). However, for most task applications, adequate color rendering can be achieved in artificially lit spaces.

However, an increasingly strong link between daylit interiors and health and productivity, implies that optimal lighting environments cannot solely be determined by illumination levels. While thoughtful artificial lighting schemes can achieve high levels of visual performance for certain tasks, several studies have analyzed the physiological and psychological effects of daylighting on humans. Though it is difficult to pinpoint daylight as the causational variable in some of these studies, they imply reasonable doubt in the adequacy of previous building practices.

Firstly, the difference in the spectral distribution and quality of light between artificial lighting and daylight can have an important impact on human health. Poor lighting conditions can cause a number of ailments, including eyestrain, seasonal affective disorder and sleep disorders. Eyestrain, for example, is caused by inadequate illuminance levels and excessive contrast, and can lead to fatigue, lack of concentration, and permanent eye damage (Simonson and Brozek 1948, Wibom and Carlsson 1987). Because daylight is such an effective illuminator, the causes of eyestrain are often less common in daylit spaces. Also, artificial lighting can induce other health problems caused by, sometimes unperceivable, rapid fluctuations in electric light output (Wilkins 1995), leading to migraines and seizures.

Other disorders more directly result from the lack of exposure to daylight. SAD, or seasonal affective disorder, may have detrimental effects on populations that don't get adequate exposures to high levels of certain spectral portions of daylight. In a small community in Russia at the 70 degree N latitude, 27% of 3736 studied inhabitants reported problems with depression and sleeping linked to the dark season, while very few had these same problems in the summer (Hansen et. al 1998). While SAD is most prevalent in high altitudes, it also occurs in environments where daylight is available, but under-utilized. In total, SAD is experienced by about 5% of the population, many whose symptoms could be tempered through exposure to daylight. (Kasper et. al. 1989, Wehr and Rosenthal 1989).

Sleep phase disorder and sleep maintenance insomnia can also be lessened by exposure to high illuminance levels (2500 to 10000 lux) and wide ranges of spectral distributions (Terman et al 1995). While certain artificial lights and sunlamps can accomplish these goals, they are often expensive, less visually appealing, highly energy intensive, and only practical for therapeutic purposes, not for general illumination. Since sleep problems affect 65% of the population (National Sleep Foundation 2008), daylighting in buildings can be a convenient means of health maintenance.

These disorders insinuate that daylight may be more extensively entwined with human vitality than was previously thought. The existence of a deeper relation between daylight and human alertness has been bolstered over the last six years, through examinations of the retinal ganglion cells in the eye and their connection with the suprachiasmatic nucleus, or circadian pacemaker. This research linked regular daylight exposure to the body's ability to maintain certain hormone levels and healthy sleep-wake cycles (Bearson et al. 2002). Lighting conditions affect the circadian system both through its power to shift the rhythm's phase (Dijk et. al. 1995), and through the suppression of melatonin (Campbell et al. 1995), a hormone secreted during sleep. Both of these effects can enhance alertness (Badia et al. 1991), which in turn increases cognitive performance (Boyce et al., 1997).

In fact, circadian studies have even incited luminaire companies to design artificial lighting schemes with dynamic light levels and tints to mimic the sun (van Bommel 2006). To be effective, artificial lighting must recreate the high illumination levels (two to three orders of magnitude higher than normal electric lighting) that are required to suppress melatonin (Ed. Rea 2000) in a tight solar waveband (440-500nm) linked to inciting alertness(Thapan et al. 2001, Rea et al. 2001, Brainard et al. 2001). However, to limit power consumption, artificial lighting restricts these high illumination levels to the small effective waveband, creating a blue tinted illumination that is not attractive or very useful for other visual tasks.

Additional studies have suggested that the eye was designed to regulate the circadian rhythm with daylight. Circadian regulation is more affected by light in the inferior retina, which is the part of the eye that receives skylight (Glickman et al. 2003). It also requires longer exposure to light for activation (McIntyre et al. 1989a-b, Rea et al. 2002) and varies in sensitivity to light depending on the time of day (Jewett et al., 1997). Regulation of the circadian rhythm is one of the stronger physiological arguments for the consideration of the spectral aspects daylight.

Daylight has also been connected to human psychological health, especially as a result of satisfied personal preference. Surveys and studies have repetitively found that building occupants prefer daylit spaces over their artificially lit counterparts (Cuttle 1983, Heerwagen and Orians 1986, Veitch 1993), indicating a strong preference for windows in their office, especially when windows had access to direct sunlight (Puleo 1991, Collins 1975). Daylighting has been connected to improved general satisfaction among building occupants (Heerwagen and Heerwagen 1986), and loosely to positive moods. A small reduction in negative mood was found for persons spending 20 minutes during the day in an office with a large window, whereas there was no improvement at night (Dasgupta 2003). While moods and satisfaction are hard to quantify, preference is an important metric when it comes to correlating daylight with psychological wellbeing.

The views that often accompany daylit spaces also influence an occupant's preferences, and are an important player in psychological health. Workers in office buildings with no connection to their outside space increased images of nature on their walls (Heerwagen and Orians 1986). Views of natural landscape have also been connected to fewer sick calls in prison infirmaries (Moore 1981), and in combination with daylight, lower recovery times in hospitals (Ulrich 1984). In fact, a study on the Sacramento Municipal Utility District's customer service call center found that workers in offices with good views processed calls 6-12% faster and had 10-25% superior memory recall than workers with no view. These workers also reported better health conditions and sense of well-being (Heschong-Mahone Group 2003). Likewise, another study on computer programmers found that workers with a view spent 15% more time on their primary tasks, instead of diverting their time elsewhere (Heschong-Mahone Group 2003).

Perhaps because of these satisfied preferences and health benefits, daylight has also been correlated to increased productivity. Studies were performed in offices (Figueiro et al. 2002) and in schools (Heschong-Mahone Group 1999a), both of which suggested this correlation, though there was insufficient evidence to determine a clear association between daylighting and student learning (NRC 2007). Nevertheless, the physiological, psychological, and health advantages of daylight are continuously being unearthed and better understood.

1.1.2. Energy and Economic Benefits

Apart from the human-scale advantages, daylighting can also have a profound influence over the lighting, cooling, and heating loads in a building. With CO_2 on the rise and a seemingly limitless demand for energy resources, there is a growing urgency to reduce the excessive energy consumption dominated by the commercial and residential building sectors. This is an important opportunity, as electricity consumption in the average home generates twice the carbon dioxide as the average car (USDOE 2007). Electric lighting directly accounts for 20-25% of the total electricity consumption in the United States and 37% of the commercial sector consumption (Ander, 1995). Adding in heating (22% of building energy consumption) and cooling (11% of total building energy consumption), the trinity adds up to a staggering 20% of total US energy consumption (USDOE 2007).

There is great promise that, with new fenestration technologies, daylighting strategies could temper this consumption. Using daylighting to curb the lighting loads would affect energy consumption most directly. The Pew Center for Climate Change estimates potential reductions in annual lighting energy use to be between 30% and 60% in buildings employing effective daylighting strategies. Case in point—for the design of the recent New York Times headquarters, researchers from the Lawrence National Berkeley Lab mocked up planned offices and recorded lighting loads before and after advanced daylighting strategies were applied. From this comparison, the researches deduced a potential reduction in perimeter-zone lighting to be as high as 60-70%, or 10-30% total building energy (Chen 2004).

Another report asserts that the effective use of well-designed windows could inhibit solar gains and foster natural ventilation, while reducing the waste heat output of electric lighting. Together, the lighting and cooling efficiency savings are estimated to add up to 5% of total annual U.S. energy consumption (Loftness 2004). Depending on climate, fenestration technology, and application, these savings will vary considerably, but they are large enough to be significant players in the climate change conversation.

These numbers are hard to verify through actual experimentation due to vast differences between buildings. However, it is intuitive that, especially in the lighting arena, daylit spaces would provide great energy savings over artificially lit spaces. For heating and cooling cutbacks, a window's insulation and heat redirection properties are most important. An experiment by the Energy Center of Wisconsin compared eight identical rooms, four with advanced fenestration technologies and four with standard clear glass glazing to quantify the savings of high-performance glazings. The lighting and HVAC operating costs were compared between the rooms, yielding a total 22% savings over summer, fall, and winter. Of these savings, 32% was from reduced lighting loads, 25% from reduced cooling load, and 24% from demand charges (mostly due to reduced cooling requirements in warm months). Heating savings were negligible, as the high performance systems limited solar gains for all months (ECW 2005).

As an added environmental bonus, building energy demands peak at the same times when daylight availability is at its max, during sunny afternoons. Since renewables usually supplement the base electricity infrastructure, shaving off peak loads would reduce the impact of more carbon intensive sources (Leslie 2003). Also, in the event that dynamic pricing schemes are passed to foster demand side management, these peak periods would become more expensive, granting great economic benefits to occupants of daylit buildings.

Apart from energy cost savings, there are a number of studies that identify the economic benefits of daylighting. While the capital costs of installing windows is higher than for concrete and brick walls (Boyce et al. 2003a), there are several economic reasons for investing in daylighting including higher rental values, lowered health costs for employers, and an increase in retail sales.

While it is hard to draw causational conclusions between daylighting and higher rental values, interviews with property professionals estimated an approximate 20% reduction in rental value for structures with a noticeable absence of windows (Boyce et al. 2003a). Daylight is a valued commodity, as evidenced by the demand for fully glazed facades in office buildings and "light and airy" residences. Even for owners who do not occupy a building, this preference is an economic concern, as tenant retention has been loosely tied to daylighting and air-conditioning performance (BOMAI 1988).

Daylit spaces also might have an effect on retail markets. Both in a bakery (Boyce et al. 1996) and a chain operating 108 stores (Heschong-Mahone Group 1999b; Heschong et. al, 2002b), daylighting had a small but significant effect in inciting an increase in sales, as compared to other identical stores that were artificially lit.

Also, a less intuitive economic concern for employers ties back to the productivity findings in the previous section. Companies have a vested economic interest in their employees' physiological and psychological health. Considering one hour of salary is equivalent to the annual lighting energy cost for that worker (Leslie 2003), the capital costs of daylighting would be highly justified if they were connected to a more productive space. As "time is money", the effect of daylighting strategies on improved productivity, increased job satisfaction, reduced absenteeism, and lack of disruption during power outages could have important economic implications.

1.1.3 Architectural and Aesthetic Benefits

As mentioned in section 1.1.1, one of the qualities of daylight that most appealing and hardest to replicate is its broad spectral make-up. This quality emboldens a space with enhanced color rendering, and is one of the many unquantifiable reasons daylit spaces are so alluring. In a survey given to office occupants, 79% preferred the appearance of their office, and 70% preferred the color of people and furnishings in their office when lit by daylight (Heerwagen and Heerwagen

1986). Again, these preferences, though aesthetic in nature, can have effects on psychological health and visual comfort in a space.

Architecturally, daylight can be a powerful artistic medium. Unlike most artificial light, the variations in the spectral make-up of daylight, the seasonal and daily changes in sun angle, and the illuminance range for different sky conditions can sculpt forms in dynamic ways, adding intrigue to a space. Frank Lloyd Wright called daylight "the beautifier of the building", and other celebrated architects such as Norman Foster and Renzo Piano have built their practices around employing daylight to enliven their designs. When daylighting schemes are carefully considered at the start of the design process, the results can be, not only practical, but also beautiful.

1.2 Daylight Delivery

The catch is that most of these benefits are highly reliant on the effectiveness of daylight delivery. For example, daylighting is not always a promoter of visual performance and comfort. Shadowing, glare, and overheating from direct or diffuse radiation can create a distracting and incommodious working environment. In fact, in one study with 300 subjects, workers in offices with high glare potential scored 15-20% lower in three out of five mental function assessment tests (Heschong-Mahone Group 2003). Other research insists that glare, when generated by direct sunlight reaching an occupant's eye or bouncing off of reflective surfaces, can be a serious obstacle to productivity and comfort (Osterhaus 2004).

Similarly with energy, the ineffective use of daylight can result in solar heat gains, nullifying the energy savings for lighting and cooling. Energy savings are dependent on the ability to control light effectively (Johnson et al. 1984). A lack of attention to daylight delivery can obliterate lighting savings by requiring permanent blinds, can dampen cooling savings with excessive solar gains, and can amplify heating loads in the winter through leakiness, lack of glazing insulation, and inadequate utilization of solar thermal energy.

To realize the benefits of daylighting, the existing installed window stock must be smarter. A smart fenestration system must use the visible portions of the daylight spectrum to address lighting needs in specific spaces. For deep rooms, fenestration systems could redirect visible light to a reflective ceiling, redirecting usable illumination to the back corners of the space. If the room is organized around various task planes, the system must redistribute daylight to improve illuminance levels in those regions of the room.

Simultaneously, windows need to respond to the different seasonal sun angles appropriately, allowing solar gains in the winter to offset heating energy needs, while rejecting them in the summer to reduce cooling loads. While all portions of the solar spectrum contribute to heat gains, humans only use the visible portion for sight. Thus, fenestration technologies combine angular and spectral components to target the near-infrared portion of the spectrum--rejecting it in the summer and admitting it in cool winter months. They also must respond to properties of the space, directing the admitted solar energy to a thermal mass in the winter so as to achieve maximal heat benefit.

One can quickly see that the effective use of daylighting is far more complex than plastering building facades with copious amounts of glass. Even advanced glazing alone, such as heavily insulated aerogels and argon gas filled glazings, will not satisfy the range of functions a daylighting scheme demands. Recently complex fenestration systems (CFS), or systems that angularly and spectrally modify daylight to assist its appropriate distribution, have become more prevalent. These systems are designed to fully glean the diverse benefits of daylighting catalogued in the previous section, while avoiding daylighting liabilities. In this section, two components of complex fenestration systems will be discussed, as they are most interesting to the topic of this thesis.

1.2.1 Angular Systems

One of the simplest ways to control the delivery of daylight is to adjust its direction. Angularly selective fenestration systems are designed to modify the incident angle (azimuth and altitude) of sunlight in beneficial ways. A simple example of these systems would be Venetian blinds or diffuse translucent sun shades. In both of these examples, the incident angle of sunlight is altered to block glare or control the amount and distribution of daylight as it enters a room.

The challenges of angularly selective systems are similar to those of any new complex fenestration system—minimizing summer heat gain and maximizing winter heat gain while still effectively illuminating the space and ensuring visual comfort. These fenestration systems could greatly reduce the lighting, heating, and cooling loads of a building. In one study, integrated angular facades were compared with the existing commercial building stock through DOE2 models that simulated daylighting and weather conditions throughout the year. The results concluded that the angular system could save 1.0 quads of electricity through lighting improvements, 1.10 quads of electricity through heating improvements, and 0.52 quads in cooling savings for the US commercial building sector (Arasteh et al. 2006). Along with these energy savings, the integrated angular facades still maintained views while not jeopardizing the listed benefits associated with daylight's spectral make-up.

Most existing angular fenestration systems are primarily designed to control direct sunlight using fins, blinds, louvers, overhangs, or other types of light rejection and redirection mechanisms. However, few do a good job of actually controlling contrast within a space, spreading the distribution of light more evenly throughout a room (Selkowitz and Lee 1998). Silvered blinds, prismatic glazings, laser cut panels, and holographic coatings have been designed with this purpose in mind, though most of these products sacrifice views or visible transmittance and thus do not take advantage of all of the benefits daylight has to offer (Selkowitz and Lee 1998). Directional light control is described as the new frontier of fenestration systems, a field "ripe for new technical breakthroughs" (Selkowitz 1999), and especially in combination with spectral systems, these innovative systems could be revolutionary in the way buildings use daylight in space.

1.2.2 Spectral Systems

Spectrally selective glazings are those that selectively modify the spectral power distribution of solar energy in intentionally beneficial ways. These spectral materials allow architects to incorporate more glazing area in their designs, as buildings can stay cooler as an effect of admitting less radiation. In conjunction with angular systems, spectral materials can have very interesting effects, controlling heat gain or purposefully selecting parts of the solar spectrum for each angular element to redistribute appropriately, depending on the seasonal and daily angle of the sun and the properties of the space.

Spectral fenestration grew out of the postwar era, as glass was tinted to absorb heat, or later coated with highly reflective particles to reject solar gains. Reflection of radiation was more efficient, as absorbed radiation continued to emit heat into a building's interior (USDOE 1998). These fenestration systems, while innovative at the time, rejected most of the visible light in conjunction with the solar gains they were combating. However, improvements over the past 25 years, have enabled low cost multi-layer thin film coatings, emerging from specialty optical applications, to overtake 1/3 of the glazing market (Selkowitz 1999). One such spectrally selective film, low-e coatings, have been developed with great improvements in daylight transmittance, and glazings with spectral coatings and applied films are now available that effectively reject NIR portions of the spectrum, while admitting visible light and keeping daylight color unaltered.

By utilizing multilayer coatings or selective absorbers or reflectors, some low-E windows have been modified with an exterior silver layer enabling it to reject 50% of total incident radiation, the portion lying in the NIR and UV portions of the solar spectrum (Selkowitz and Lee 1998). The coatings are applied using a sputtering process, where soft metals or chemical combinations are sprayed onto a glass substrate, which is then insulated in a glass unit or laminated to protect the longevity of the coating (USDOE 1998). As these coatings have dropped from \$500/m^2 to less than \$5/ m^2, they are great materials for the design of systems aiming to control solar gains (Selkowitz 1999). In fact, in conjunction with highly insulated glass units, these windows can now outperform an insulating wall in the winter (Selkowitz 1999).

Coatings can also be deposited as a thin polymer film that is suspended over the substrate (USDOE 1998). Compared with the transmittance of its predecessors, spectrally selective films allow 70% transmittance of daylight, almost twice of the transmittance of tinted and reflective film glazings. They also maintain an average around 45% transmittance of solar gains, which is comparable to reflective films and slightly lower than tinted glass at 64% (Watts 2005).

Some tinting technologies are still used to increase spectral selectivity while increasing transmittance, specifically green and aqua tinted glass. These colors are most prevalent because of their ability to absorb NIR and UV portions of the solar spectrum, while transmitting a broad portion of the spectrum. Usually a combination of ferrous oxide and ferric iron is used for these tints (Pilkington 2008), compounds which also absorb parts of the red and blue spectral ranges, transmitting or reflecting slightly green light. The tinted units are most effective when placed on the exterior of an insulating glass unit, and combined with a low-E coating to avoid re-radiation of absorbed heat into the space (USDOE 1998).

Still, these tints alter the color rendering capabilities of daylight, and have been known to incite occasional uneasiness in occupants, making them less desirable alternatives to other spectrally selective glazing options.

Other new spectrally-selective materials on the market include electrochromic technologies, touted as the most promising of the new switchable window technologies (LBL 2008). In electrochromics, multi-layered thin films are controlled via low voltage signals to change from high transmission to low transmission, ranging between 5 to 60% in visible transmittance and 10 to 45% in solar heat gain coefficient (Selkowitz and Lee 1998). These coatings respond to varying sky conditions, and have the capability of lowering peak electric loads by 20-30% in many commercial buildings (Carmody et al. 2004). Electrochromic coatings are, thus, very versatile, and can control glare, illuminance levels, heat gains, and even privacy.

Spectrally selective glazings have many benefits over their tinted counterparts. Unobstructed views, a clearer connection to the outdoors, and increased glazing area (from 15-20% to 50% (USDOE 1998)) are some of the aforementioned benefits. Also, spectrally selective glazings, clear from both the outside and inside, don't inflict glare and solar loads on adjacent buildings and vegetation (USDOE 1998). Spectrally selective glazings can also preserve the colors of fabrics and interior furnishings by limiting UV transmittance (USDOE 1998).

Finally, there are the expected energy and economic benefits. Selective glazings have a pay back within 4 to 10 years, and thus are a cheap technology to employ for the respective energy reductions. A study by the DOE in 1998 showed that an $8 million investment in low-e coating systems in the United States would allow manufacturers to produce 1.86 million m^2 of low e windows each year for 10 years. As a result of the installation of this improved window stock, the US would conserve 36 M barrels of oil equivalent over the lifetime of the windows (20 years). The same amount of oil would cost $300 million to produce, over ten years, through means of a conventional oil platform in Santa Barbara. In total savings, without even considering oil spills, carbon dioxide emittance, and other environmental and political costs, this was a 97% savings (USDOE 1998). Even greater savings could be earned today, as glazing technology prices have decreased and oil prices have increased. Thus, the proliferation of spectrally selective glazings, especially as a material within angular systems, could be of escalating importance in the near future.

2. Measuring Bi-Directional and Spectral Distributions

The development and urgent deployment of these complex fenestration systems requires a thorough investigation of their properties. To facilitate CFS design, it is important to be able to test and describe the directional and spectral modifications of a light beam after it has been reflected off or transmitted through a fenestration sample. The complications of this characterization process bottleneck the introduction of CFS into new commercial building stock.

2.1 Bidirectional Distribution Functions

Advanced fenestration systems are difficult to characterize because of their multidirectional distribution properties and complex spectral effects. While most simple glazings can be characterized using solar heat gain coefficients, U-factors, and visible transmittance coefficients, these metrics are ineffectual for angular systems, as their properties no longer vary predictably (Arasteh et al. 2001). As a result, CFS must be described by quite involved functions, whose parameters should include the incident and emerging (transmitted or reflected) light direction and spectral power distribution (SPD).

These functions are called bidirectional scattering distribution functions (BSDF), and they can be measured for samples that reflect light (BRDF) or transmit it (BTDF). A BSDF measures the distribution of light that results after a beam hits a fenestration sample in a certain incident direction.

2.1.1 Mathematical description of BSDFs

In photometric terms, BSDFs are defined as the “quotient of the luminance of the medium by the illuminance on the medium” (CIE 1977), or mathematically:

$$BSDF(\theta_i,\phi_i,\theta_r,\phi_r) = \frac{L_{sample}(\theta_i,\phi_i,\theta_r,\phi_r)}{E(\theta_i,\phi_i)} \qquad (2.1)$$

where the symbols used are described as follows:

(θ_i,ϕ_i) are the polar coordinates of the incident beam, with θ_i as the altitude angle (°) and ϕ_i as the azimuth angle (°)

(θ_r,ϕ_r) are the polar coordinates of the resulting reflected or transmitted radiation distribution

$L_{sample}(\theta_i,\phi_i,\theta_r,\phi_r)$ is the luminance emerging from the tested material, defined for each incident and emerging angle (Cd/m^2-sr)

$E(\theta_i,\phi_i)$ is the illuminance on the sample plane due to the incident beam's flux (lux), including any angular or spectral modifications of the beam before it reaches the sample.

Since the beam, in the case of sunlight and sources replicating the sun, is generally collimated, E (θ_i, ϕ_i) is considered constant across the sample section.

As shown in Figure 2.1 (taken from Andersen and Scartezzini 2004a), one complete BSDF (measured in sr^{-1}) would characterize the flux distribution for any chosen angle of incidence after a beam has been reflected off, or in this case, transmitted through a sample.

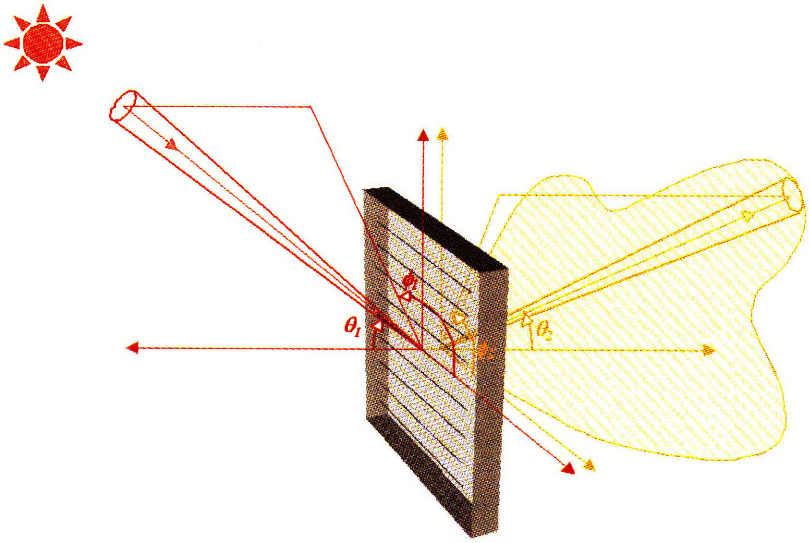

Figure 2.1: Bidirectional transmission distribution function of fenestration material (Andersen and Scartezzini 2004a)

Similarly, these functions can be measured in spectral quantities. A spectral BSDF would yield a vector for each angle set (instead of a scalar as in a photometric BSDF), describing the reflectance or transmittance of a sample measured at wavelength increments of λ for the chosen incident and emerging angle. A spectral BSDF is defined as the quotient of the spectral radiance from a sample by the spectral irradiance on the sample, mathematically:

$$BSDF_{\lambda}(\theta_i,\phi_i,\theta_r,\phi_r,\sigma)=\frac{L_{e,sample,\lambda}(\theta_i,\phi_i,\theta_r,\phi_r,\sigma)}{E_{e,\lambda}(\theta_i,\phi_i,\sigma)} \tag{2.2}$$

where the symbols used are described as follows:

(θ_i, ϕ_i) are the polar coordinates of the incident beam, and (θ_r, ϕ_r) are the polar coordinates of emerging radiation, with θ referring to altitude angle (°) and ϕ to the azimuth angle (°)

σ is the polarization state of the incident and emerging radiation

$L_{e,sample,\lambda}(\theta_i,\phi_i,\theta_r,\phi_r,\sigma)$ is the spectral bidirectional radiance emerging from the sample in each direction(μW/m^2-sr), discretized in λ wavelength increments

e(subscript) denotes a radiometric quantity

$E_{e,\lambda}(\theta_i,\phi_i,\sigma)$ is the spectral irradiance on the sample plane due to the incident beam's flux (μW/m^2), discretized in λ wavelength increments

Spectral radiometric BSDFs describe the distribution of radiance for a beam of given irradiance and angle of incidence, for any wavelength or polarization state. Since the sun emits randomly polarized light, the effect of polarization should be minimal, and thus will be excluded in the final calculation of BSDFs for the purposes of this thesis. However, a more in depth analysis of the effect of polarization on actual BSDF measurements will be described in chapter 7.

Spectral radiometric BSDFs would require the ability to measure the spectral distribution of radiance at each emerging direction and the spectral irradiance for a given incident direction. Thus, they are most informative in the characterization of fenestration systems that are simultaneously angular and spectral, as these systems could modify the spectral power distribution of incident light differently for different emerging angles. If total radiometric BSDFs were used to characterize such samples, their distributions may show a change in total radiance levels among emerging angles, but would provide no information on whether this effect was caused by the angular components or the spectral components of the system. Furthermore, total BSDFs would offer no information about what parts of the spectrum were being modified for each angle, making it impossible to determine whether the spectral elements of the system were operating as designed.

Another limitation of using total BSDFs instead of spectral BSDFs is that total BSDFs are only valid in characterizing a sample for a particular incident spectrum. For example, if the source spectrum for a BSDF measurement has a bluish-green spectral power distribution between 400 and 600nm, the results would not be applicable to an application using sunlight as the source. For total BSDFs, the relative spectra of the light source used for measurement and the light source used in actual application must be very similar in order to achieve meaningful results.

2.1.2 The Use of BSDFs

These functions, once measured, will help foster the increased use of complex fenestration systems. While BSDFs are used in a broad range of fields, from computer rendering to texture studies to luminaire characterization, in the field of daylighting, they are required for systems with angularly selective components. Knowledge of spectral BSDFs will aid fenestration designers to invent more efficient and holistically beneficial commercial products and encourage their integration into usable software for architects and engineers.

Indeed, complex fenestration systems have not yet been incorporated into modeling software as their directional and spectral properties are largely undocumented. While available building energy simulation software, like BLAST and DOE2, have the capability of simulating conventional windows whose optical properties are well known, they are confined to specular materials, or ones with essentially no angular scattered radiation component (McCluney 1998). This is unfortunate, as modeling software has been known to make a significant impact on the design and increased utilization of fenestration products (Arasteh et al. 2001). Other simulation tools such as DElight, in combination with EnergyPlus, have the capability of modeling the effects of complex fenestration systems, as long as the BSDFs for these systems have been pre-measured before being integrated into the software(Hitchcock and Carroll 2003).

BSDF information could also be useful in early design stage tools and databases. Because CFS simulations of spatial and time variant indoor lighting conditions could easily get complicated, and thus expensive, designers need tools to identify which CFS could be suitable for their specific needs (Andersen 2006a). The incorporation of CFS information into informative databases, such as Windows 5 (Versluis et al. 2007) and D-LITE (Urbano and Andersen 2008), that could plug into early stage daylight simulation tools, such as LightSolve (Andersen et. al 2008) and its associated rendering engine (Cutler et. al 2008), would make CFS selection simpler for architects considering their use.

While the usefulness of BSDFs is easy to demonstrate, the major challenge remains how to measure them. There are different methods for determining the BSDFs of fenestration systems and no absolute standards to compare the results of these different methods (Andersen 2006b). The two most promising methods, ray tracing and direct measurement with a tool called a bi-directional goniophotometer, differ in their complexity but could be combined to achieve a very successful assessment method.

Ray-tracing based calculation methods are less expensive and more available than direct measurement methods. In a ray tracing calculation, the geometry of the fenestration system is modeled and then illuminated such that a defined grid of rays passes through the sample to demonstrate its angular properties. The collection of emerging rays creates a flux map, which can be simulated for different angles of incidence. For spectral samples, this calculation can be re-simulated at each wavelength to produce spectral maps (McCluney 1998).

Three of these "virtual" goniophotometers have been developed using three different ray-tracing softwares, and are described in (Andersen and de Boer 2006a). These virtual methods have been mostly successful in the determination of BSDFs for systems with repeated, and already known components. However, their utility is limited for systems using new materials or innovative (but undocumented) coatings. Because this method is highly sensitive to input details about angular scattering properties, deficiencies in the input information would result in great variance in the output results from the model (McCluney 2002).

Thus, the argument becomes circular, as detailed bidirectional information is needed for each of the elements in a CFS to achieve detailed bidirectional information about the whole system. When this information is available, ray tracing models have had great success replicating results achieved through direct measurement methods (Andersen et. al 2004b). The results have been shown to be sufficient for complex fenestration system evaluation (Andersen 2005a), and the feasibility of ray tracing characterization promises its success in provoking a surge in complex fenestration markets and computer modeling integration.

2.2. Existing Goniophotometers and Goniospectrometers

To use ray tracing models successfully, the preliminary characterization of most complex materials must first be ascertained experimentally. The experimental determination of BSDFs is the function of an instrument called a bidirectional goniophotometer --"gonio" meaning angle, and "photo" meaning light. A goniophotometer becomes a goniospectrometer when it acquires the ability to assess the spectral properties of light as well. There have been several iterations of goniophotometers and goniospectrometers designed specifically for the analysis of advanced fenestration systems.

Most of these existing goniophotometers are based on a scanning method, where a detector gathers BSDF information at a series of predetermined points forming a hemisphere around the reflecting (or transmitting) sample (Andersen and de Boer 2006a). This technique is both time intensive and discrete, creating the possibility of missing certain narrow spikes in areas between measurement points. However, more time efficient approaches have been developed using a Charge-Coupled Device (CCD) camera as a detector, which records the distribution of light from all emerging angles at the same time (Andersen et. al 2005b, Ward 1992). These devices correlate pixel values with radiometric (or luminous) quantities from different solid angles, so the bidirectional distribution of radiation can be reconstructed in a time efficient manner. The pros and cons of both methods will be outlined in the following sections.

2.2.1 Scanning Goniophotometers and Goniospectrometers

Scanning goniophotometers all operate under the same principle. A sample is illuminated by a light source at a chosen incident direction, while a detector gathers total luminance or total radiance measurements around the sample. Either the source, the sample, or both can move to accommodate these different angles of incidence. Generally, the two biggest drawbacks to this type of system are its time expensive detection process (which escalates when fine resolution measurements are required) and the discrete nature of its investigation.

Scanning methods have aimed to lower the likelihood of missing specular peaks or incidents of glare that could occur between detection points by incorporating a preliminary assessment scan of the sample's radiance distribution for all incident angles (Apian-Bennewitz 1994b). Unfortunately, this solution only compounds the time required to assess the BSDF of the sample.

Still, scanning goniophotometers have improved considerably since their introduction in the late eighties at Lawrence Berkley National Lab (Papamichael et. al 1988). Notable innovations include the ability to make adaptive refinements in angular resolution (Apian-Bennewitz 1994a, Apian-Bennewitz and von der Hardt, 1998), using multiple sensors to cut down on data collection time (Aydinli 1996), and significant mechanical improvements in regards to the movement of the detector (Apian-Bennewitz, 2006).

Perhaps the most significant innovation, at least in regards to the scope of this thesis, is the incorporation of the spectral characterization of CFS into scanning goniophotometry for daylighting applications. Both a scanning goniospectrometer at Cardiff University (Breitenbach and Rosenfeld 1998) and one from the consultancy company, *pab-opto,* have innovated new methods for analyzing spectral BSDFs (Apian-Bennewitz, 2006). The Cardiff instrument, now at the Technical University of Denmark (DTU), utilizes two scanning spectrometers, one with a silicon detector measuring wavelengths between 300 to 1100nm and one indium-gallium arsenide detector (InGaAS) measuring wavelengths between 900 and 2100nm. The spectrometers are attached to an off axis parabolic mirror used for light collection, which focuses transmitted or reflected radiation on the end of the spectrometer's optical fibre bundle. These optical fibres take measurements at every emerging direction in a hemisphere around the sample.

The Cardiff goniospectrometer has been used to measure the spatial and spectral transmittance of window components like holographic optical element (HOE), which is a type of spectrally selective filmed glazing. For certain angles of incidence, HOEs split transmitted radiation into two components of varying spectral distributions--a component scattered 45 degrees forward and a color image transmitted directly through the element. The results of this measurement are shown in Figure 2.2 (Breitenbach and Rosenfeld 1999), and demonstrate the type of data achievable with this new spectral innovation. Figure 2.2a depicts the total luminous transmittance for the HOE at each emerging angle (α,β) in the Cardiff coordinate system when illuminated at normal incidence. The angle (α,β) corresponds to a shifted version of the (θ_r,ϕ_r) from Eqn. 2.1, where (α,β) $=(90°,90°)$ refers to the emerging angle of normal specular transmission. The two different components can be seen in this graph, each associated to a different spectral power as shown in 2.2b. This example clearly demonstrates the utility of spectral information, since without the information shown in 2.2b, the scattered component's color (slightly green) and the colored image's appearance (yellow) would remain unknown. The two components also should be treated very differently because of their different NIR spectral properties.

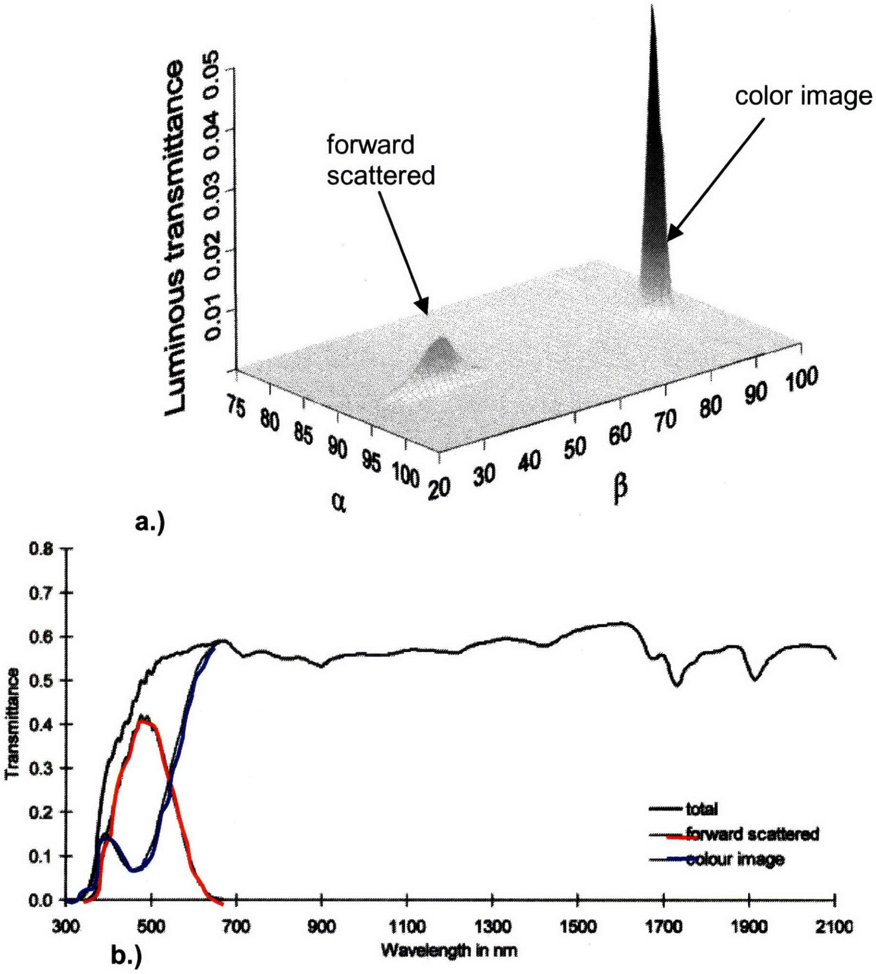

Figure 2.2 a.) Cardiff goniophotometer total luminous transmittance for emerging angle (α,β) and normal incidence b.) Cardiff goniophotometer spectral transmittance for forward scattered and color image portion of transmitted radiation distribution. (source: Breitenbach and Rosenfeld 1999)

Unlike the Cardiff goniospectrometer, the *pab-opto* instrument only provides quasi-spectral BSDF information, or average transmittances and reflectances across certain wavelength bands for each emerging angle. This new goniospectrometer uses a variety of light sources and a modular detector concept that can be adapted to different applications. The choice of detectors covers radiometric, photometric, infrared, and multi-channel spectral ranges that together form the quasi-spectral BSDF measurements.

While these few existing goniospectrometers already collect spectral information, the time required to assess a total BSDF is at least four days for the Cardiff goniospectrometer and is undocumented for the pab-opto goniospectrometer (Andersen and de Boer 2006a). Currently neither use cameras to measure reflectance and transmittance spectra, limiting spectral characterization to instruments with long scanning-based BSDF acquisition.

2.2.2 Video-Projection Goniophotometers

With the advent of inexpensive digital cameras came new ideas about how to assess BSDFs more efficiently and continuously. Charge-Coupled Device (CCD) cameras, if used in lieu of traditional detectors, could visualize thousands of emerging angles simultaneously, capturing the entire distribution of radiance very quickly. Of equal importance, since images offer continuous pixel coverage, video-based methods could map the entire hemisphere of emerging directions continuously, assuring that the results would not miss any important specular peaks. Additionally, there would be no added time for the collection of finer resolution data as the finest resolution would be at the pixel level, and course resolution could be achieved by averaging over groups of pixels.

Three video-based projection goniophotometers and one video-based projection goniospectrometer exist today, all of which distinguish themselves from other goniophotometers by through their reliance on a projection principle to avoid moving the CCD camera from one acquisition point to the next. Two of these have been designed for research in daylighting and two for research in computer graphics. The original design, developed by Greg Ward at LBNL for the latter usage, is diagrammed in Figure 2.3 (Ward 1992). In Ward's goniophotometer, light is projected onto a target that is positioned near the focal point of a half-silvered hemisphere. When the target reflects the incident radiation, it is then re-reflected off the interior surface of the hemisphere into the fish-eye lens of a CCD camera located on the opposite side of the focal point. The CCD camera is calibrated to associate pixel locations with sample emerging angles, and a BRDF for the fenestration system can be reconstructed.

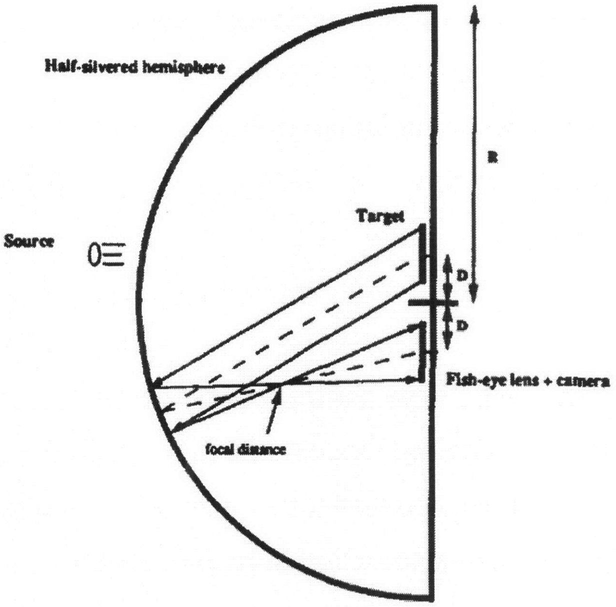

Figure 2.3 original video-goniophotometer concept designed by Ward

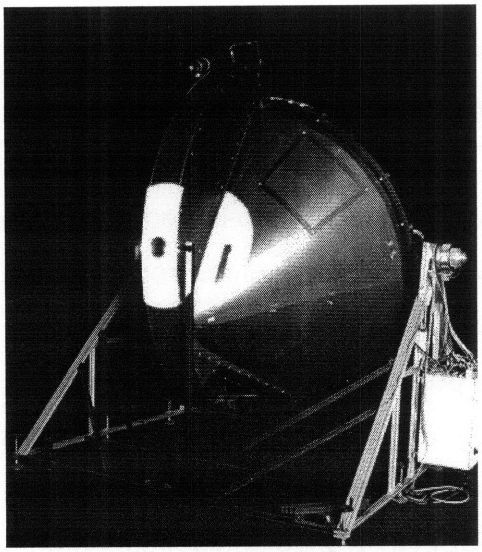

Figure 2.4 EPFL video-goniophotometer

This first device was the inspiration for two other video-projection based instruments. The first, a goniophotometer at the University of Rennes 1 in France (Deniel 2002), uses a diffusing cube as the projection surface to enhance photo-realistic rendering in computer graphics. The second, and most recent, is a goniospectrometer at the Daylighting Lab at MIT called “Heliodome”, which will be discussed further in this thesis.

The final device, developed at the Solar Energy and Building Physics Laboratory at EPFL in Switzerland (Andersen et al. 2001, 2005b) used a triangular diffusing projection screen to capture emerging radiation from the sample, located on the interior of the light-proof carbon fiber cone displayed in Figure 2.4. The screen, not being reflective, had the advantage of avoiding inter-reflections. Its diffuse properties minimized polarization effects that were problematic in the two previous computer rendering models.

A camera with a wide-angle lens facing this projection screen images the screen for each of six positions covering the full 2π steridians. Up until the development of the MIT goniospectrometer, this system was the only fully validated video-goniophotometer designed for the analysis of CFS, achieving a final relative error of 10% and empirical validations between 5-8% (Andersen 2006b). It is still the only instrument of its type for which an extensive set of BSDF data have been produced (Andersen and de Boer 2006a).

The EPFL goniophotometer measures luminances through a similar calibration process as the one described in Chapter 6. The basic idea is to modify the spectral sensitivity of the CCD camera with filters that, when used in combination, closely resemble the sensitivity of the human eye. Several images can be taken at different integration times to calibrate the camera's output with known luminance measurements, taken by a luminance meter (Andersen et. al, 2001). Since the illuminance on the sample is usually known, these luminance levels for each pixel can be used to calculate a photometric BSDF by spatially calibrating pixel location to emerging angle.

The introduction of a modified spectral sensitivity to the camera allows it to measure total luminances independently of the sample's spectral reflectance or transmittance. However, it is important to restate that the resulting photometric BSDF, because it is not a spectral BSDF, is only meaningful for applications where the incident beam has a similar spectral power distribution as the beam utilized in the measurement process. As a result, façade materials should be investigated with a light source with a spectral power distribution similar to that of sunlight or daylight.

3. Heliodome Design and Development

The mentioned goniophotometers depict the state of the art for the measurement of BSDFs of complex fenestration systems. While they all bring important innovations to the area of CFS assessment, each goniophotometer has its advantages and disadvantages and its usefulness depends on the task at hand. Certain goniospectrometers give detailed spectral BSDFs, but none can measure them time-efficiently. Other video-goniophotometers have superior speed, angular resolution, and can achieve continuous results; however they are unable to measure spectral or radiometric information. Other goniospectrometers have expanded their spectral sensitivity range, allowing them to consider NIR range radiometric distributions in addition to the visible, but they, too, have lengthy data collection processes.

The novelty of the new MIT Heliodome is its incorporation of the benefits of all of these goniophotometers into one instrument, resulting in a time-efficient, continuous measurement process that results in spectral radiometric and total photometric BSDFs across the visible and NIR spectral ranges.

The Heliodome is automated for both the visualization of sunlight distribution inside a scale model (a heliodon), and the video-based measurement of BSDFs of materials (goniospectrometer), however, this thesis will only discuss the latter function. Since its inception in 2004, much work has been completed on the Heliodome's mechanical design, lighting components, and camera calibrations, which is described in (Gayeski and Andersen 2007a) and (Andersen 2005b). Its design and major components are outlined in this chapter.

3.1 Design Concept and Functioning Principle

As previously mentioned, the Heliodome was modelled after a prototype designed for computer graphics applications (Ward 1992) using a mirrored hemisphere as a projection screen which would reflect light emerging from an object into a CCD camera detector. This design was modified to be applicable for window samples, accommodating transmission measurements in addition to reflection measurements. The hemisphere was changed to a hemi-spheroid in order to create two focal points—one where the camera is positioned and the other at the position of the fenestration sample.

A HMI collimated light source illuminates the sample which then transmits (or reflects) the emerging distribution onto the hemi-spheroid. For BRDFs, the beam must first pass through the semi-transparent surface of the hemispheroid before reflecting off of the sample, whereas for BTDFs, the beam is directly transmitted through the sample from the underside of the table. As shown in Figure 3.1, due to the geometry of the hemi-spheroid, all emerging light will travel from one focal point, where the material sample is located, to the other focal point, onto the fish-eye lens of the camera.

When the radiation reaches the camera, the resulting image is spatially calibrated so that each pixel corresponds to a small area on the hemi-spheroid. The camera is also calibrated to act as a radiometer (Chapter 5) or photometer (Chapter 6). Images are taken at different exposure levels and converted to a High Dynamic Range (HDR) image (Inanici 2006) of the interior of the hemispheroid. For photometric measurements, this HDR describes luminance estimates for each pixel location. For radiometric measurements, the HDR provides radiance estimates from the red, green, and blue channel of the camera for each pixel. Thus, the HDR image maps the entire emerging distribution of light for the chosen incident beam angle, and can be converted to a BSDF through the methods developed in subsequent chapters.

The hemi-spheroid, the material sample, and the camera are attached to a motorized table with two rotational degrees of freedom, enabling easy modifications to the chosen incident beam angle. Through the assessment of BSDFs at all incident beam angles, a complete characterization of the fenestration system's radiation distribution properties can be determined. This information can be used to describe how the window system would modify the angular and spectral properties of incident sunlight for any season, time of day, sky condition or facade orientation.

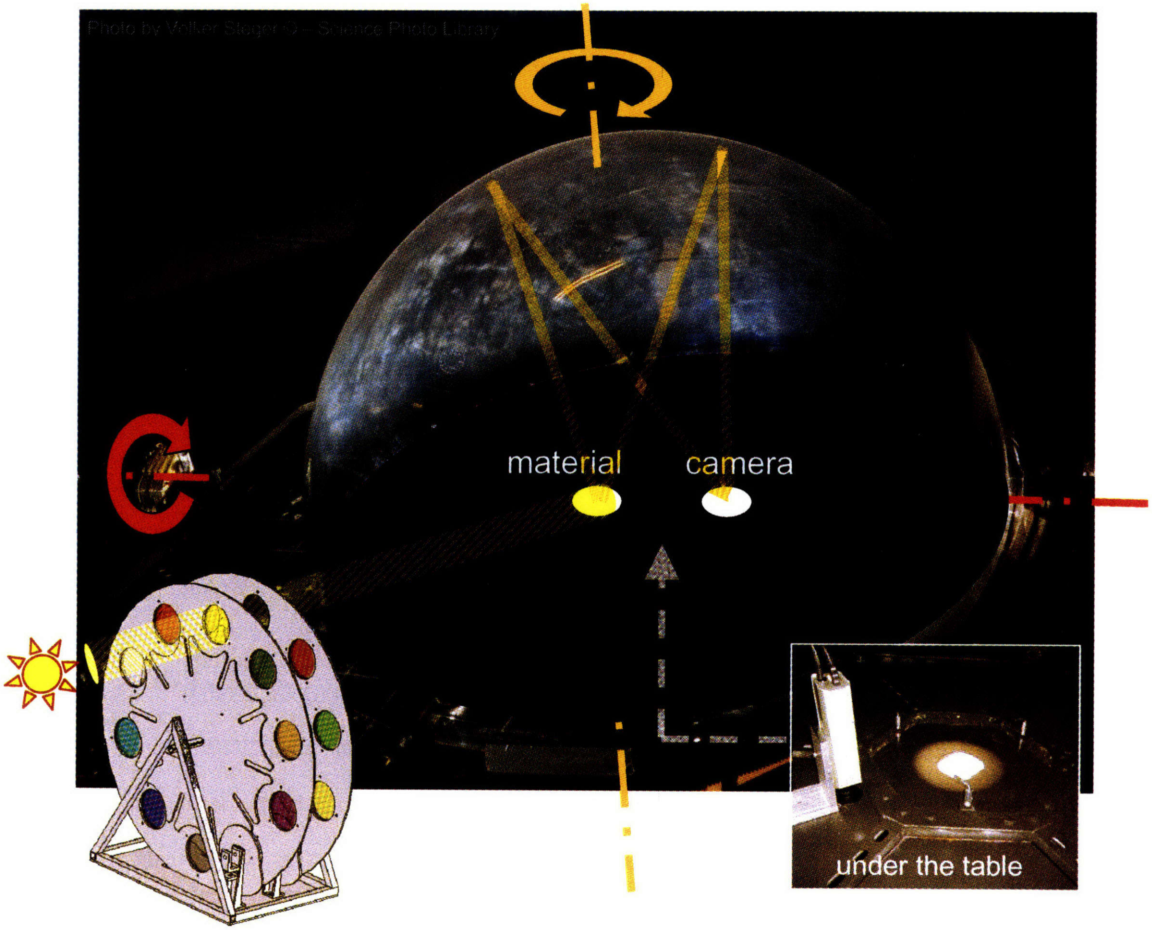

Figure 3.1: Heliodome components: The HMI beam reaches the material sample (at one focal point), from which reflected or transmitted light gets reflected once off of the hemi-spheroid to the digital camera (at the other focal point).

3.2 Components and Previous Work

The Heliodome is comprised of the components shown in Figure 3.1. A brief summary of each component is provided in this section.

3.2.1 Rotating Sample holder

As mentioned, the CFS sample is held on a table with two degrees of rotational freedom, controlled by two separate motors. The first degree of rotation, shown horizontal in Figure 3.1, defines the altitude angle between the lamp beam and the sample, θ_i. The second, shown vertical in Figure 3.1, rotates the sample 360 degrees in the specified altitudinal plane, and is denoted by ϕ_i. The sample holder situates the CFS sample such that a stationary beam, mimicking the sun, hits the sample at a chosen incidence angle pair (θ_i,ϕ_i).

The sample holder accommodates fenestration samples with a diagonal diameter between 100mm-200mm and thickness less than 20mm. A full description of the table's design is given in (Ljubicic 2005).

3.2.2 Light Source and Filter Wheel

The source used to illuminate CFS samples in the Heliodome is a 400W dedolight HMI lamp chosen because of its collimation and its relative spectral emittance, which is similar to that of sunlight (Browne 2006). Figure 3.2 shows the relative spectral irradiance of the HMI light, measured with an Ocean Optics USB2000 spectrometer, compared to the ASTM Terrestrial Reference solar spectral irradiance distribution (ASTM 2008). The light has three adjustment settings (also listed in Appendix B) that are fixed throughout the data collection process—the power supply and the lamp output mode are set to "spotlight" to induce maximal collimation in the beam. The beam diameter is also adaptable through an aperture that varies the size of the output port of the lamp. The setting of this aperture greatly affects the illuminance on the sample plane and the angular spread of the beam. The beam's half angular spread has been chosen to be 2.4°, for reasons listed in section 7.2.

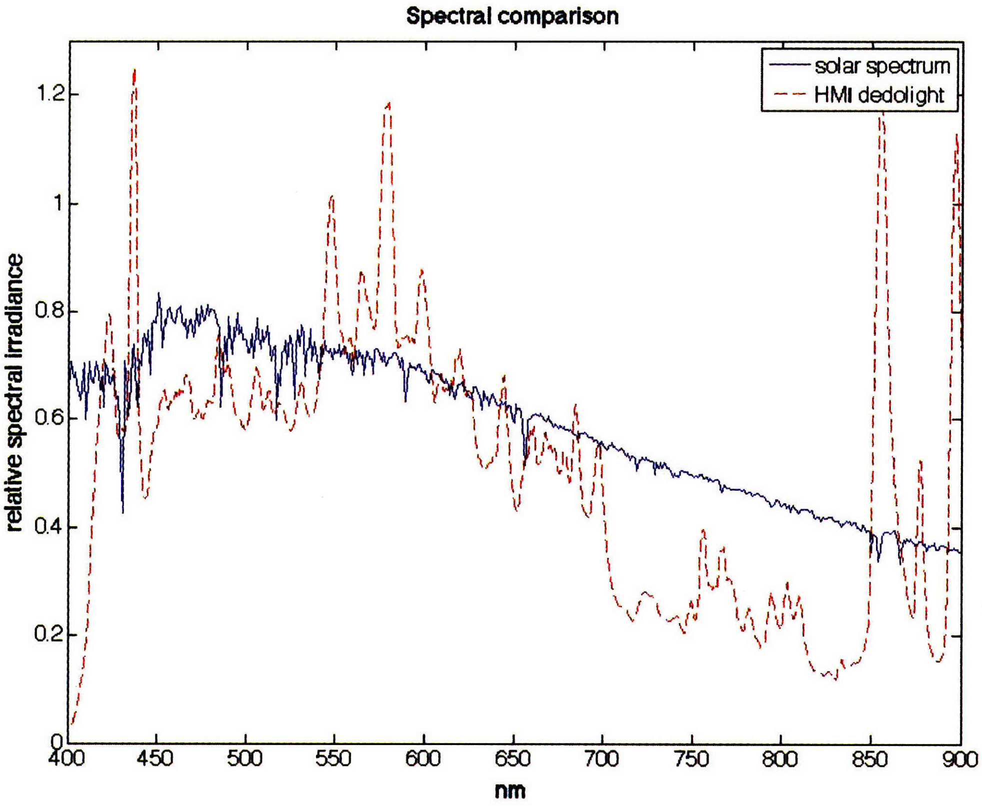

Figure 3.2 HMI spectrum as compared to sunlight

In transmission, the table is turned such that the lamp projects onto the sample from the underside of the table. Thus, the portion of the incident beam entering the spheroid is restricted to the size of the sample's diameter. The beam hits the sample directly, without any modifications for fixed spot size.

In reflection, however, the entire beam is transmitted through the spheroid's semi-transparent acrylic shell, causing the camera to view parasitic light reflections from the illuminated area outside of the sample's diameter, as shown in Figure 3.3a. First, black felt was applied to the sample holder's metal edges to minimize its specular reflectance, as shown in Figure 3.3.b. However, even with this correction, the camera still detected diffuse reflection from the beam hitting outside of the sample area. To ameliorate this problem, in reflection, the beam has been modified with a black light corset, fixing the beam diameter such that it only illuminates the sample, correcting most of the parasitic light reflection, as shown in Figure 3.3c. The remaining parasitic light captured by the camera is dealt with in section 6.3.2.

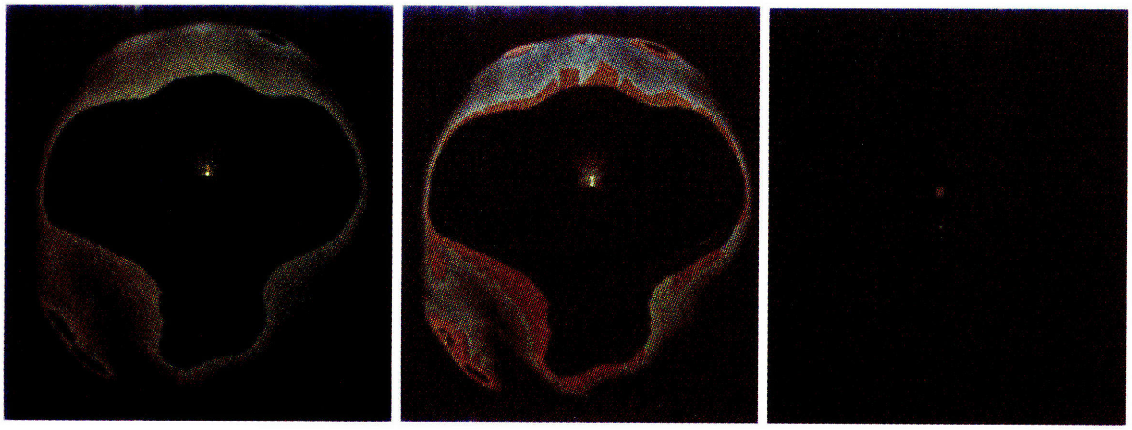

Figure 3.3 Black corset applied as a solution to parasitic light problems. 3.3a) image of a "hole" captured in reflection. b) image of a hole with felt correction applied to edges of the sample holder c) image of hole with black corset applied to limit beam width to sample diameter

The HMI lamp is also projected through one of nine Schott filter combinations, as shown in Figure 3.4, before reaching the sample or hemispheroid. Eight of these filter combinations are used for radiometric BSDF assessment and one is used for photometric BSDF assessment, however, the purpose of these filters will be explained in greater detail in the subsequent chapters. All of the filters are held in a filter wheel (Koch 2007) shown in figure 3.4, which will be programmed to cycle through the whole filterset once per incident angle while the camera captures a series of images at different integration times for each filter.

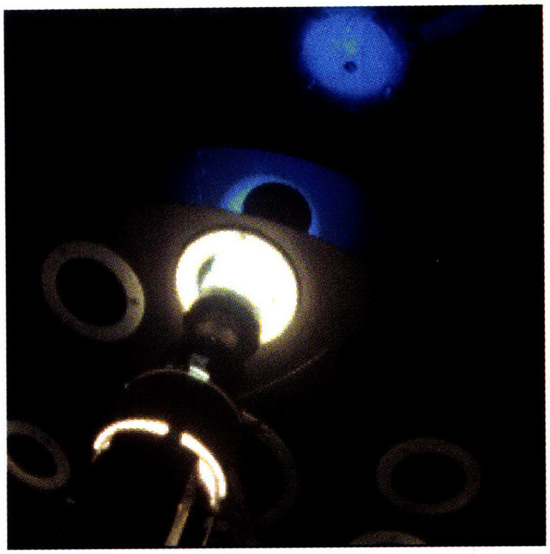

Figure 3.4 HMI dedolight, filter wheel, and sample port

3.2.3 Half Mirrored Hemi-Spheroid

The hemi-spheroid, shown in Figure 3.5, is an acrylic shell coated on the inside with a thin film of aluminum, such that it is about 40% transmissive over the whole dome. The final dimensions of the spheroid are the same as the original design, chosen so that the distance from the sample to the spheroid is always greater than five times the sample's diameter (Browne 2006). The development and characterization of the new spheroid is discussed in detail in chapter 4.

Figure 3.5 Aluminum coated acrylic hemispheroid on table

3.2.4 Digital Cameras

Two digital cameras are used in the Heliodome, a Kappa DX20 color CCD camera sensitive in the 380-950nm spectral range and a Sensors Unlimited SU320 1.7RT near-infrared camera sensitive in the 900 to 1700nm range. Both utilize an interchangeable Fujinon high resolution fisheye lens with a 185 degree opening angle. The spatial and radiometric calibration of the CCD camera is documented in (Gayeski 2007b), and the calibration of the NIR camera is discussed in appendix A. A luminance calibration was also performed on the CCD camera, using a photopic $V(\lambda)$ filter to measure photometric BSDFs, documented in section 6.2.

3.2.5 Image Acquisition

Two computer control softwares are used to capture the images used to reconstruct photometric, radiometric, and spectral radiometric BSDFs. The CCD camera uses Kappa ImageBase Control, with which integration time can be varied. All other controls for the CCD camera should remain unchanged, as the camera settings must match their respective values at the time of the radiometric calibration. The settings were chosen so as to apply the least amount of photo manipulation to the raw images, and are listed in Appendix B.

The NIR camera is controlled using a National Instruments (IMAQ) interface, though the control of both cameras will eventually be integrated in the Heliodome interface, which will also organize the presentation of the final BSDF results. All image processing will be performed using MatLab®, as described in Chapter 6 of this thesis.

4. Developing the Hemi-Spheroid

As the hemi-spheroid is the vehicle for radiation traveling from the sample to the camera, it is most important that the surface and geometry be pristine. The geometrical accuracy, surface characteristics, and spectral properties of the spheroid greatly affect the resulting imaging, and thus are critical in the accurate estimation of spectral BSDFs.

While hemispheroids were developed in previous stages of the Heliodome project (Browne 2006, Gayeski 2007b), they were unusable due to imperfections in the manufacturing process. This chapter will describe the accomplishments of the second iteration of hemi-spheroid development, as well as the spectral characterization of the final hemi-spheroid.

4.1 Modifications to the Hemi-Spheroid

Due to complications in the manufacturing process, the geometry of these domes was found to be faulty (Gayeski 2007b). . Thus, the first step in the development of the new hemispheroid was the identification of imperfections in the geometry, in order to improve the next manufacture.

In order to investigate these geometrical inaccuracies, the shape of the hemispheroid was measured, point by point over a 5cm by 5cm grid that spanned the entire base of the dome. At each grid-point, the perpendicular distance from the table to the domes interior surface was measured and recorded. These measured points were plotted and compared against the targeted geometry, a hemispheroid of major axis 1150mm and minor axis 1122.5mm, as shown in Figure 4.1a, with the dotted line outlining the profile of the theoretical spheroid. The differences between each point on the theoretical spheroid (purple) and the measured spheroid (grey) are charted in Figure 4.1b.

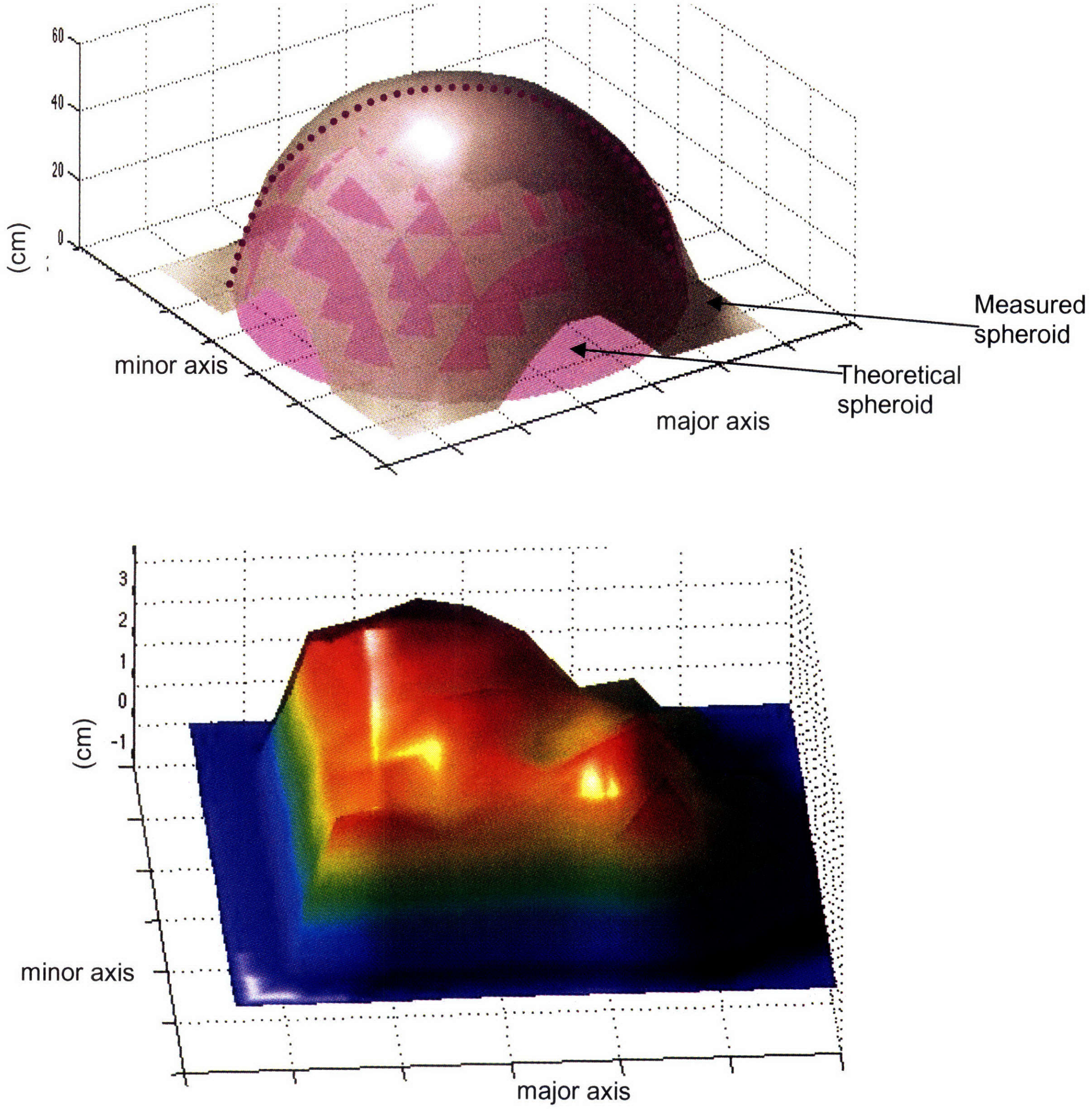

Figure 4.1 a) geometry of measured spheroid (grey) compared with theoretical spheroid (dotted line). b) Differences in height (cm) between the theoretical and measured spheroid for all grid points.

These graphs reveal a 2-3cm discrepancy between the spheroid's theoretical form and the measured spheroid at the apex, causing the spheroid to redirect light towards the center of the spheroid, "undershooting" the second focal point. This phenomenon can be observed in Figure 4.2, where the yellow arrows indicate the correct redirection of light from the sample port, reflecting off the spheroid's interior surface onto the center of the white target, positioned at the camera port. Instead, the spot can be noted to the right of the focal point, missing the camera's fisheye.

In addition to this geometrical flaw, due mostly to an inaccurate mold, the surface quality of the spheroid's acrylic induced a wavy effect on the spheroid's redirected light. Because the hemispheroids were formed on a mold, temperature differentials between the hot acrylic and the mold may have caused contraction patterns during cooling. In order to address both defects, a new hemi-spheroid was manufactured at Replex Plastics without the mold.

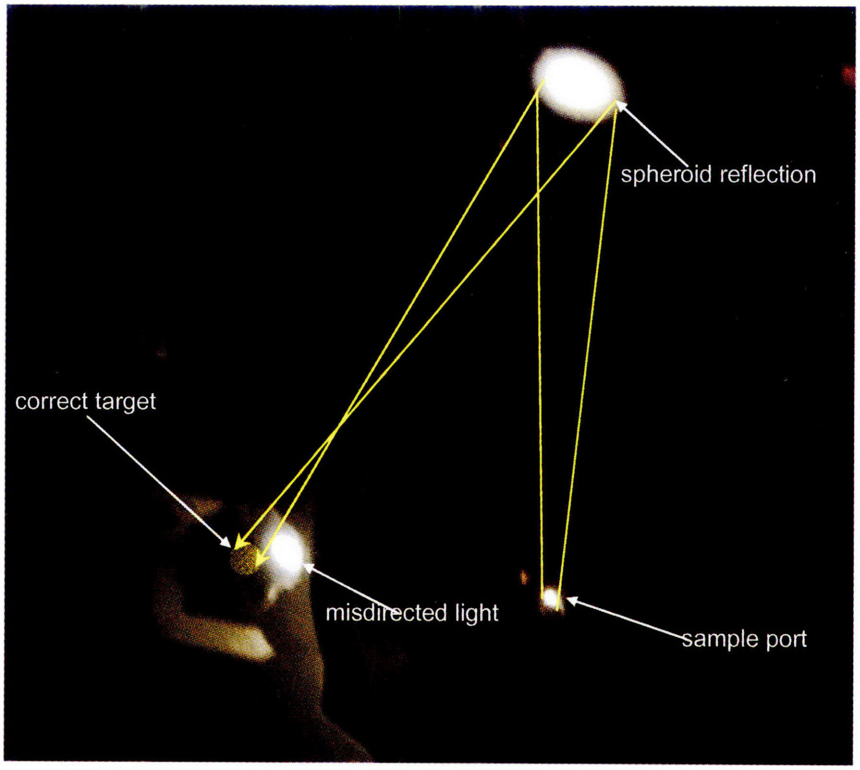

Figure 4.2 Light mis-redirection due to spheroidal curvature inaccuracy

The hemi-spheroid was made of mirror grade extruded acrylic, which was free-formed in a vacuum cavity at Replex. The acrylic was heated with differing temperature patterns that altered the dome's shape, while the geometry was controlled by the pressure differential across the bubble balanced by the tensile stress in the polymer. When the spheroid was formed, 3" holes were drilled in two places on the flange to attach the spheroid to the table and define the minor axis.

Once the forming process was completed, the spheroid was coated with a thin-film of aluminum. While this coating is needed to redirect light from the sample to the camera, it is kept very thin in order to allow the transmission of the incident beam, enabling sample reflectance measurements. The transmittance of the spheroid can be observed in Figure 4.3, a photo taken of the daylighting lab from inside the spheroid.

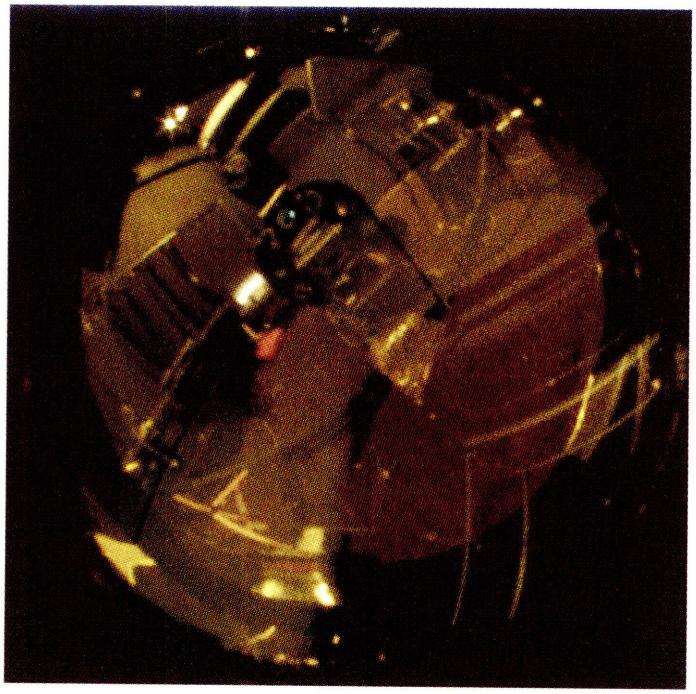

Figure 4.3 Image of daylighting lab through spheroid, demonstrating transmittance

Because acrylic is very sensitive to heat, the dome was coated through a cathodic arc evaporation physical vapor deposition (PVD) process. In this process, a target of aluminum is struck with a low voltage, high current arc in a vacuum, spraying vaporized aluminum at the acrylic shape without damaging it (Richter et al. 1998). The dome was metalized on the inside, with the target positioned such that it was approximately centered and equidistant to any point on the interior of the spheroid. As discussed in section 4.2, this set-up made it possible to achieve a more uniform coating thickness, and thus a more even spectral transmittance and reflectance across the spheroid's surface.

In order to achieve a correct geometry, several domes had to be manufactured and checked for accuracy. In order to accomplish this verification at Replex, four arcs, defining the profile of the spheroid, were cut from a 3/16" thick polycarbonate sheet wide enough to span the entire dome. The holes in the flange were used to properly align the arcs along the major axis, the minor axis, and at 45 degree increments in between. When each spheroid was formed, the acrylic geometry was compared against the arcs to see where improvement was needed. By adjusting the heat pattern in the forming machine, the dome's local geometric inaccuracies could be adjusted in the region underneath that particular heater. Thus, the heating pattern was not uniform in the end, but instead was allowed to vary in order to fine-tune the observed shape of the bubble. With each dome iteration, the geometry was improved to more closely conform to the shape defined by the arcs.

Through this free-forming process, the surface quality of the spheroid was markedly improved. As shown in Figure 4.4, the reflected light beam is much more clearly imaged in the free-formed spheroid. In fact, when the interior surface of the spheroid is illuminated with a Labsphere KI-120 tungsten halogen lamp, the lamps concentric circular flux pattern can be clearly observed. In the previous spheroid, this same beam reflectance resulted in a muddled post-reflection image.

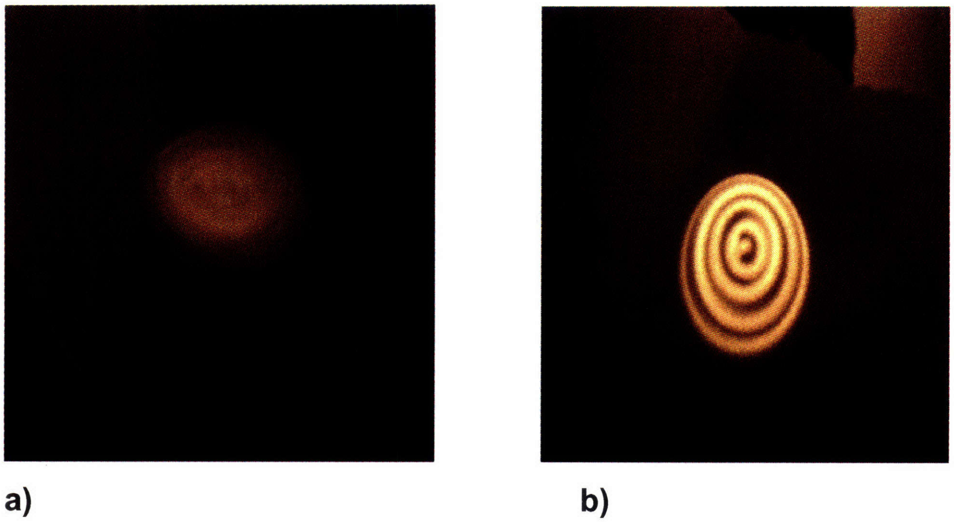

Figure 4.4 a) reflection of tungsten-halogen lamp off of mold-extruded hemispheroid. b) reflection of tungsten-halogen lamp off free-formed hemispheroid

The spheroid's geometry was also verified through the process documented in figure 4.2. In transmission, the Heliodome was tested for a hole, or empty sample port, as the incident beam altitude and azimuth was varied. For each incident direction, the beam was reflected off a different portion of the spheroid's surface and was redirected to the camera port. The spheroid's geometry was verified for all incident angles, except for altitude-azimuth pairs in the range of (60-65°, 30-45°), (60-65°, 135-150°), and for all angles with altitudes greater than 80°, as shown in Figure 4.5.

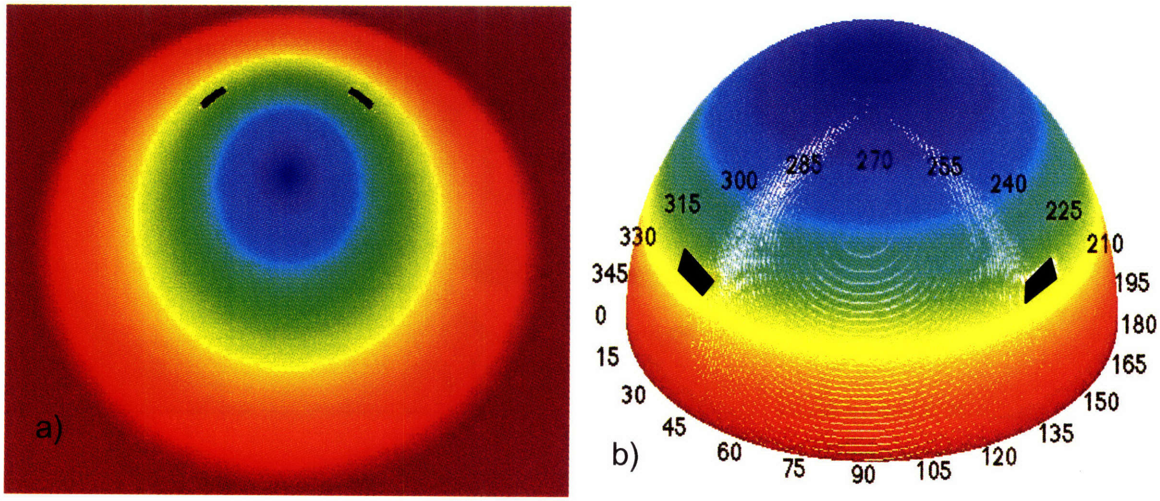

Figure 4.5 a) angles (60-65°, 30-45°) and (60-65°, 135-150°) identified on a raw image b) corresponding locations on the spheroid's surface.

The black spots in Figure 4.5a identify these angles of mis-redirection on a raw image, whereas Figure 4.5b correlates these locations to positions on the spheroid's surface. The red band in both images also highlights the higher angles (greater than 80), for which the spheroid is not reliable.

A sample diameter of 10cm was determined to be the limiting size that would still accurately redirect all incident beams such that their reflected spot completely covered camera port. This sample size was determined by testing the Heliodome in reflectance mode for a diffusing sample. The sample diameter was limited by an opaque aperture, starting at 3cm in diameter and escalating upwards. For each aperture size, an image was taken with the CCD camera of the diffuse distribution having reflected off of the hemispheroid. The resulting images revealed the angles for which the spheroid correctly and incorrectly reflected radiation to the camera. By increasing the sample size, the number of correct angles was increased, as shown in Figure 4.6. With a sample diameter equal to 10cm or greater, the radiation distribution from almost all sample emerging angles was redirected to the camera's fisheye. Thus, the free-formed hemispheroid was shown to have gained a notable improvement over the previous hemispheroid, whose limiting sample diameter was greater than 20cm.

Figure 4.6 a) 3cm diffuse sample in reflection, b) 5cm diffuse sample in reflection, c) 10 cm for diffuse sample in reflection

4.2 Characterization of Spheroidal Spectral Transmission and Reflection

Because all radiation reaching the camera reflects off of the hemispheroid, it is important to know how the spheroid modifies the spectral power distribution of the emerging sample radiation. Knowledge of the spheroid's spectral and total reflectance and transmittance in the 380-1700nm range is thus necessary for an accurate assessment of the fenestration sample's spectral and total transmittance or reflectance, the ultimate goal of the Heliodome.

When characterizing the spheroid, it is first important to establish a coordinate system to describe the position of a point of reflection or transmission on the spheroid's surface. The position of the spheroid was determined through a sample-oriented coordinate system, also used in (Gayeski 2007b). This coordinate system, displayed in Figure 4.7, is based on the movement of the rotating table, with the CFS sample (F1) positioned at the origin. As a result, a beam projected normal to the CFS sample (θ_i=0), does not reflect off of the apex of the spheroid, and the cross-sections at each θ_I are not symmetric on the spheroid's surface. For example, as shown in the figure, (θ_i,ϕ_i)=(10°,90°) locates a point lower on the hemispheroid's surface than does (θ_i,ϕ_i)=(10°,270°).

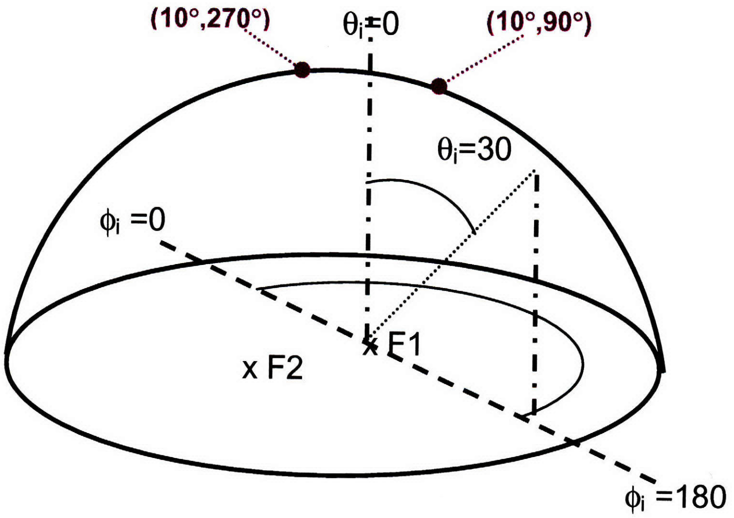

Figure 4.7 Spheroidal sample oriented coordinate system

The spectral transmission and reflection coefficients were measured with an Ocean Optics USB2000 spectrometer in the visible range and an NIR512 spectrometer in the near infrared range. Both spectrometers were calibrated to measure absolute irradiance (μW/cm^2). The spectrometers' bare fiber optic was positioned outside of the spheroid facing a tungsten halogen lamp placed inside the spheroid, as shown in figure 4.8. The beam was projected through the acrylic, while the spectrometers recorded measurements at every 30° of azimuth at θ_i=60°. The spectral transmittance at each point could be calculated by comparing the spectrum of the tungsten halogen lamp before and after passing through the spheroid.

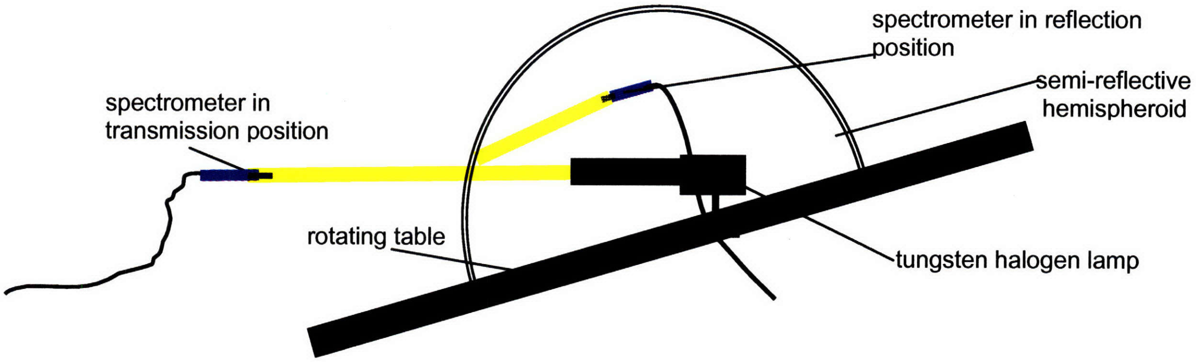

Figure 4.8 Experimental setup of spheroidal transmission and reflection measurement procedure

The results of this measurement process are shown in Figure 4.9. As was observed, the aluminum coating among azimuth angles is very even, resulting in approximately the same spectral transmittance for each azimuth measurement. This circumferential uniformity is probably due to the rapid rotation speed used during metallization. Another positive attribute is the spheroid's stable transmittance spectrum across the whole visible range. This stability allows passage to all wavelengths of the incident beam, restricting any major spectral selectivity to the fenestration sample.

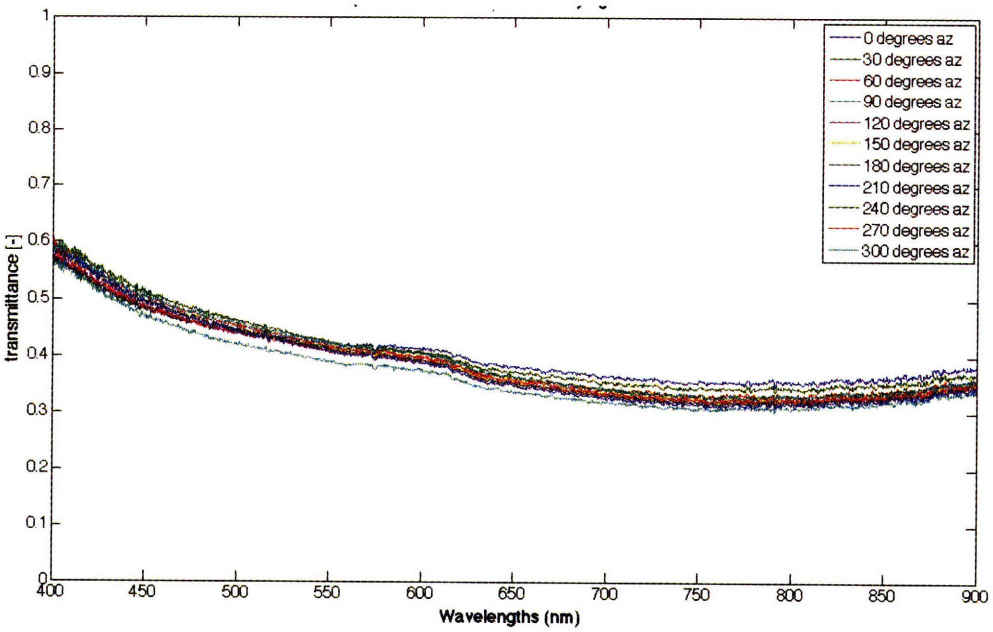

Figure 4.9 Spheroidal spectral transmittance for θ_i=60

Results for the near infrared portion of the spectrum, shown in Figure 4.9, were similarly uniform for all azimuth angles and similarly constant across the NIR range.

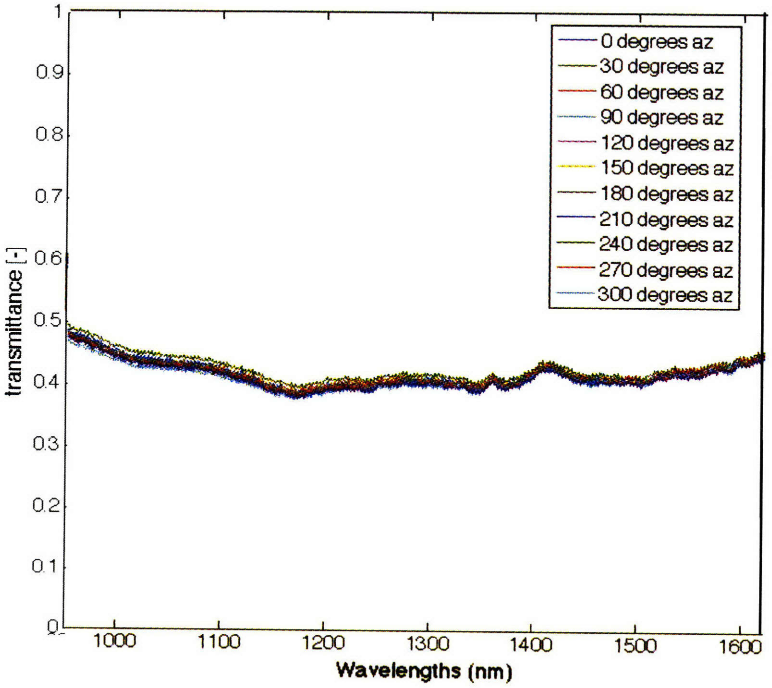

Figure 4.10 Spectral NIR transmission in the spheroid for θ_i=60

The spheroidal spectral transmittance was also measured for varying degrees of altitude between θ_i=85 and θ_i=5, as shown in Figure 4.11. Because the circumferential variation was determined to be small, the transmittance along the major axis (270° azimuth) was assumed to be representative of the variation among all azimuth axes. While the total transmittance decreases for higher altitude angles, the relative spectrum stays approximately the same. Total transmittance variation was determined to be in the range of 35% (at the flange) to 50% (at the apex) for the visible spectrum.

NIR measurements along the major axis, displayed in Figure 4.12, confirmed a similar 15% variance amongst altitude angles-- 45% (at the flange) to 60% (at the apex). The relative spectrum was also the same for the NIR, independent of total transmittance discrepancies.

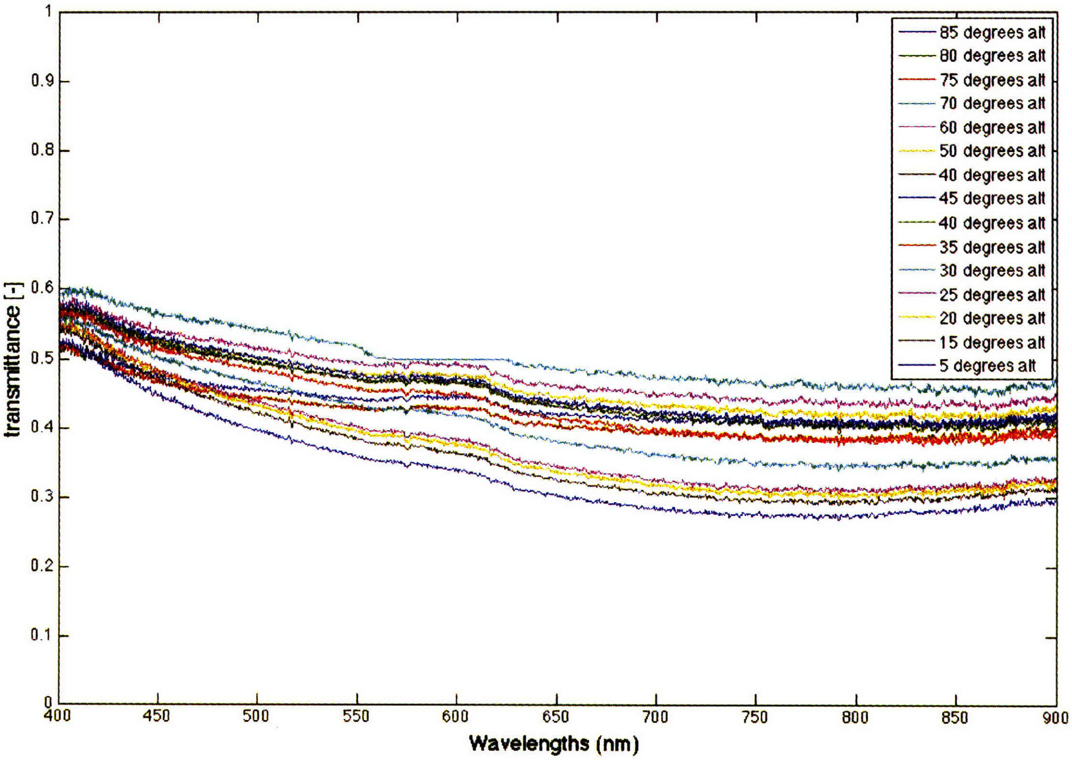

Figure 4.11 Visible spectral transmittance in the spheroid along the major axis

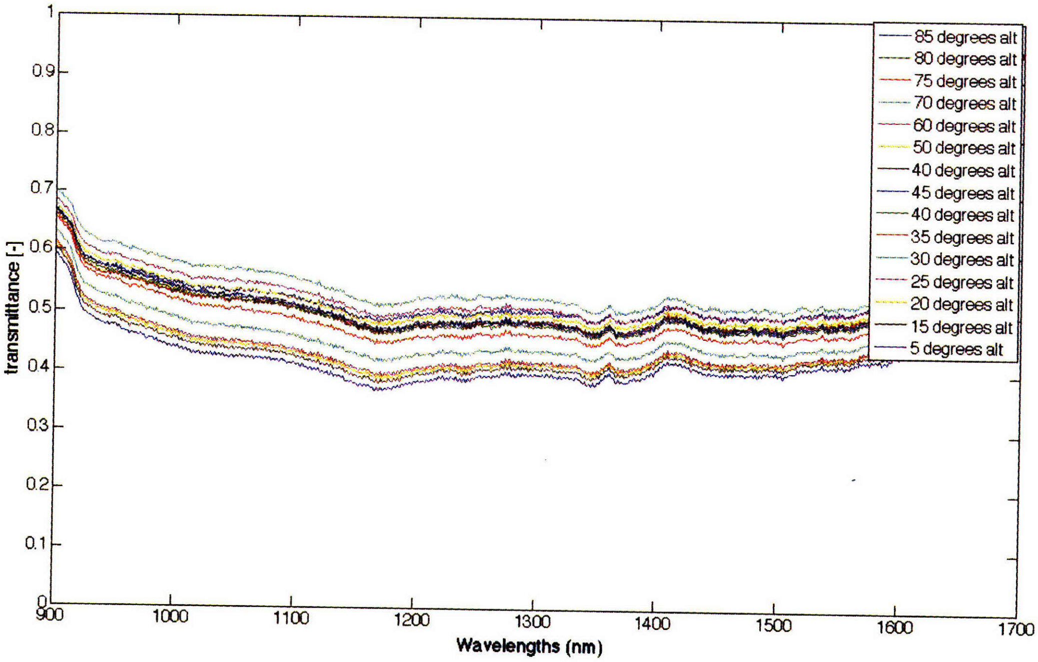

Figure 4.12 NIR spheroidal spectral transmittance along the major axis

The spectral reflectance of the spheroid was also measured for varying altitude and azimuth angles. In this case, the spectrometer's fibre optic and tungsten-halogen lamp were both positioned inside the spheroid through the sample port, facing the interior surface. The lamp's beam was reflected off of the spheroid, and the fibre optic was positioned slightly off normal, to receive the emerging radiation.

In order to measure the baseline spectral irradiance, the spectrometer had to be repositioned facing the lamp at a distance approximately equal to the total distance travelled by the reflected beam. Because the spectrometer was positioned to the side of the sample port, this total distance was subject to variation, and the average distance was used, introducing error into the absolute spectral irradiance measurements. Also because the spectrometer is so angularly sensitive, absolute irradiance measurements varied for each azimuth and altitude measurement since, unlike in transmission, the angle of acceptance could not be held constant. As a result, the visible and NIR spectral reflectance measurements, shown in Figure 4.13 and 4.14, will only be used to define the relative spectrum.

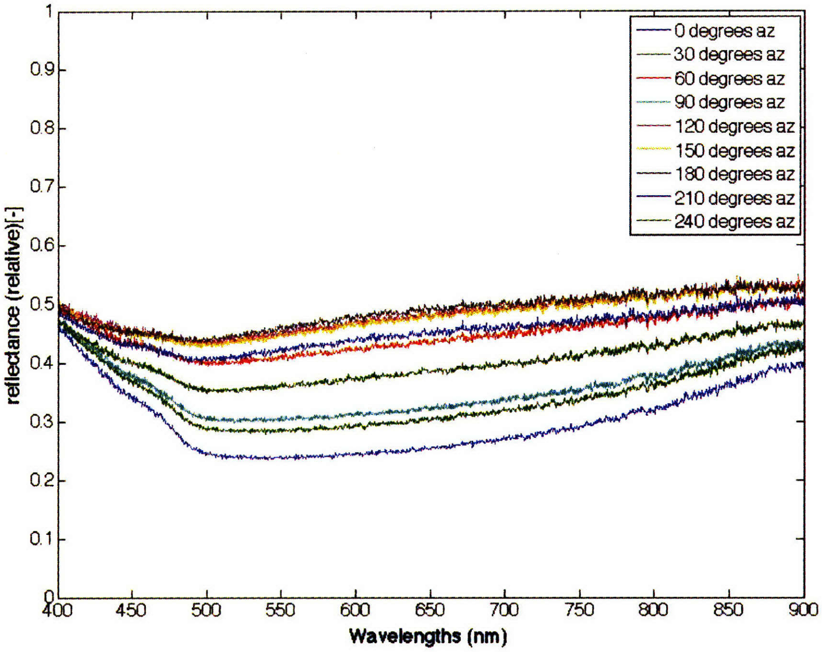

Figure 4.13 Spectral reflectance for θ_i=60 in the visible range

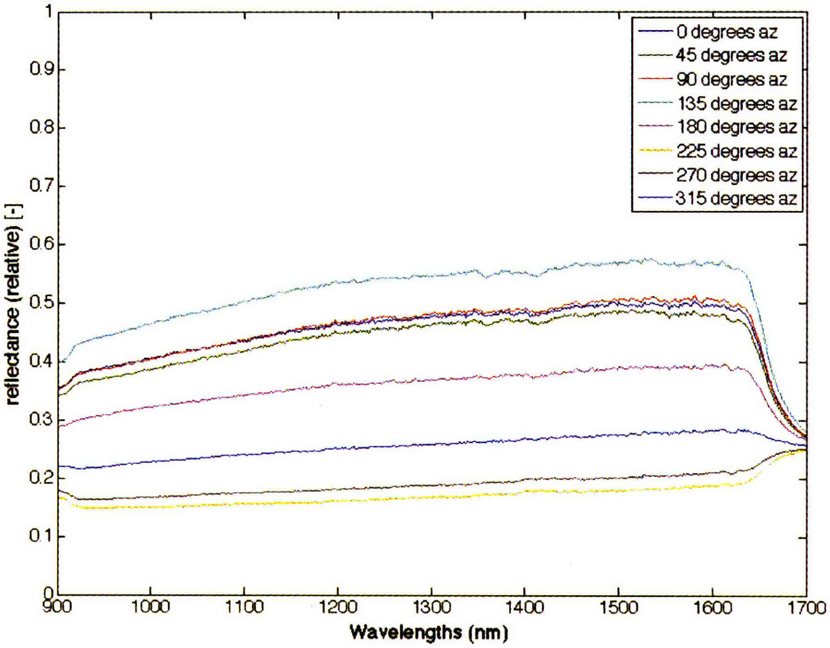

Figure 4.14 Spectral reflectance for θ_i=60 in the NIR range

Additional information was needed to revise the absolute magnitudes of these reflectance spectra, and scale them appropriately. Because the transmission measurements were known, an experiment that determined the relationship between transmittance and reflection was devised. This relationship, once determined, would use the magnitudes of the spectral transmittance spectra for each (θ_i,ϕ_i) to inform the magnitudes of the spectral reflectance spectra for the same incident angle.

A Labsphere integrating sphere, calibrated to measure total radiant flux for monochromatic beams, was used to relate transmission and reflection for various points at different azimuths and altitudes over the entire hemispheroid. First the radiant flux of a tungsten halogen lamp with a 500nm narrow passband filter was measured without the spheroid to determine the baseline. Then the tungsten halogen lamp and filter were placed inside the spheroid, such that the beam was oriented towards the spheroid's interior surface. The lamp's vent was blocked with black cloth, and the integrating sphere was zeroed so measurements were not affected by parasitic light. The beam's orientation was modified to test forty different positions on the spheroid, ranging in altitude and azimuth. Both a transmittance measurement and reflectance measurement were taken at each of these positions, by moving the integrating sphere into and out of the spheroid, as shown in Figure 4.15.

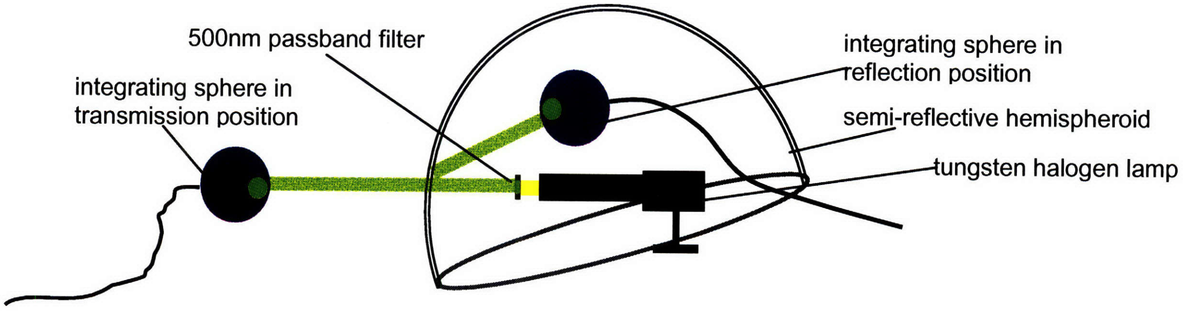

Figure 4.15 Experimental set-up relating reflectance and transmission

After dividing the transmission and reflectance measurements by the baseline measurement, reflectance and transmittance of 500nm light can be related for each measured position on the spheroid. The assumption is that as the thickness of the aluminium coating increases, transmittance will decrease while reflectance increases, following the theoretical relationship between the two quantities, well-known from literature. By collecting measurements over the whole range of aluminium thicknesses, a functional relationship can be defined between the two quantities.

Figure 4.16 shows this association, an almost linear relationship, deduced from the experimentally determined individual measurements. This function contains all of the information needed to revise the magnitudes of the spectral reflectance measurements shown in Figures 4.13 and 4.14. For each altitude and azimuth, the transmittance coefficient at 500nm can be located on the curve below, and the corresponding reflectance at 500nm can be deduced.

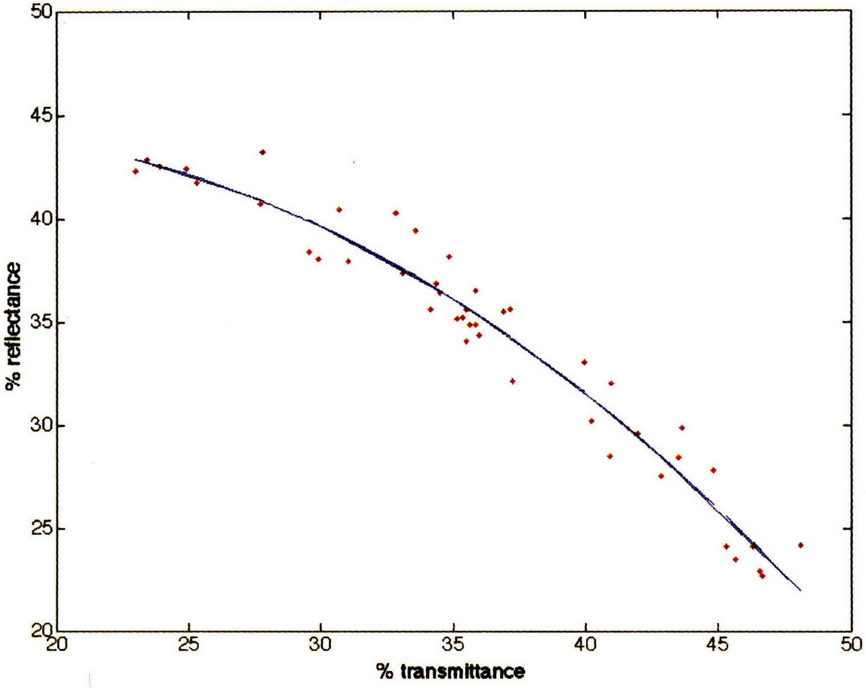

Figure 4.16 Relationship between reflectance and transmission for 500nm light

To extrapolate this relationship over the surface of the hemispheroid, the integrating sphere and 500nm filter were again used to measure the radiant flux at locations along the major and minor axis, verifying the accuracy of the spectral measurements. By knowing the radiant flux of the beam without the hemispheroid, the predefined reflectance-transmittance relationship was applied to each of the measured transmittance points to derive the reflectance and absorption at each altitude at the two azimuths (sample coordinate system). The results are shown in Figure 4.17, with most measurements still within the range of 35-50% transmittance, resulting in a reflectance range of 25-40% for 500nm.

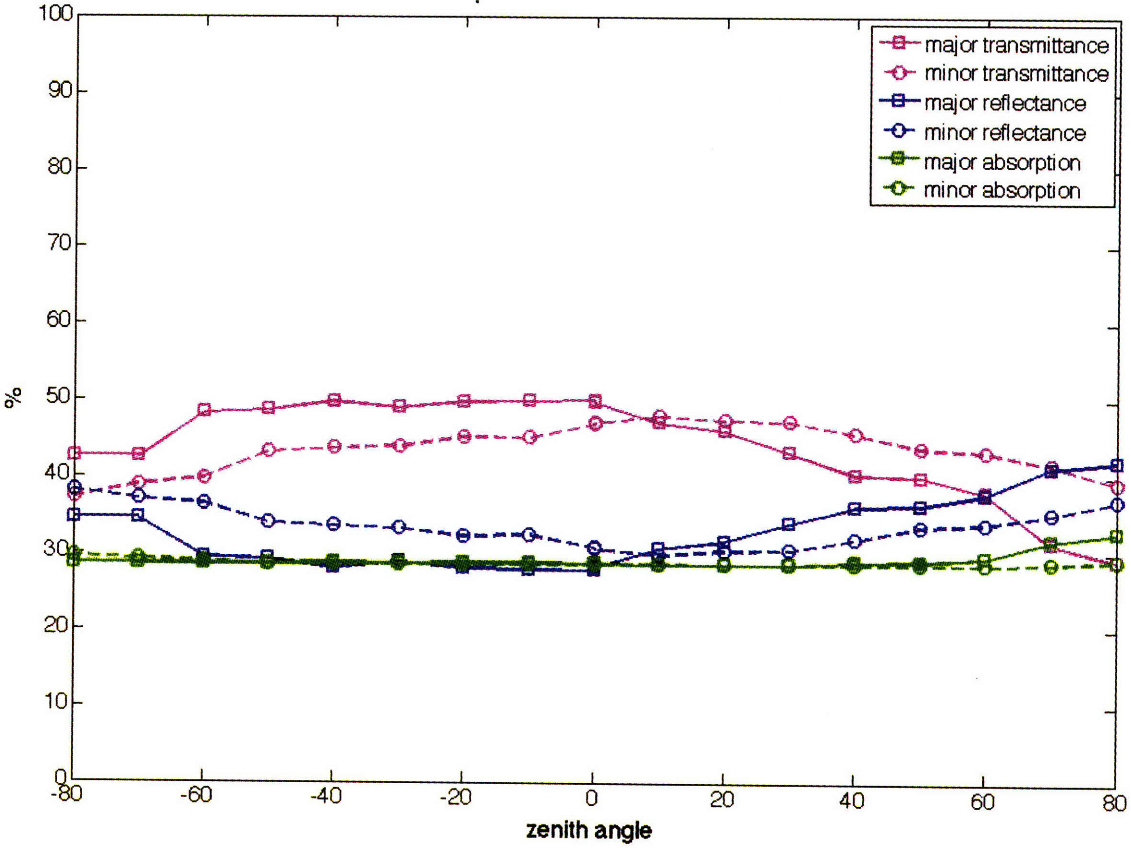

Figure 4.17 Spheroidal reflectance, transmittance, and absorbance of 500nm light across the major and minor axis.

Considering spectral transmittance was measured to be uniform along any given altitude, the transmittance (and thus reflectance) of the spheroid to 500nm radiation can be estimated over the entire surface of the spheroid for the given altitude angles by interpolating between the major and minor axis measurements. The resulting weights, graphed in Figure 4.18 and 4.19, are used to scale the relative spectrum to find the spectral transmittance or reflectance for any position on the entire spheroid. This $\rho_{spheroid,\,\lambda}(\theta_r,\phi_r)$ and $\tau_{spheroid,\,\lambda}(\theta_r,\phi_r)$, measured discretely in λ wavelength increments, will be relied on extensively in the spectral estimation method described in Chapter 5.

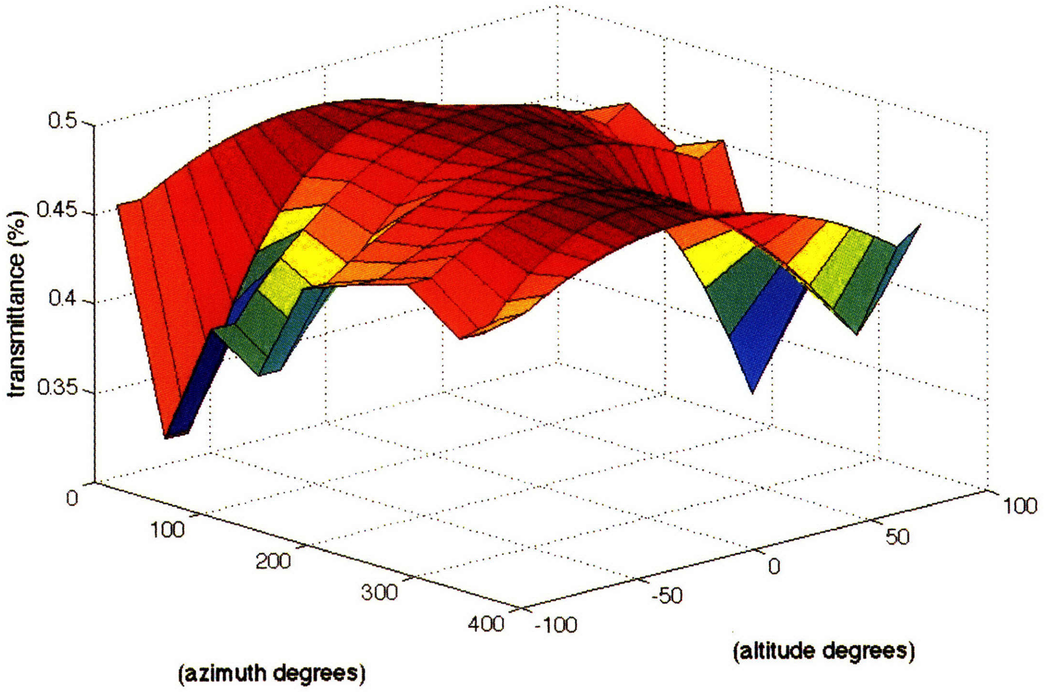

Figure 4.18 Transmittance of spheroid to 500nm radiation at all altitude and azimuth angles

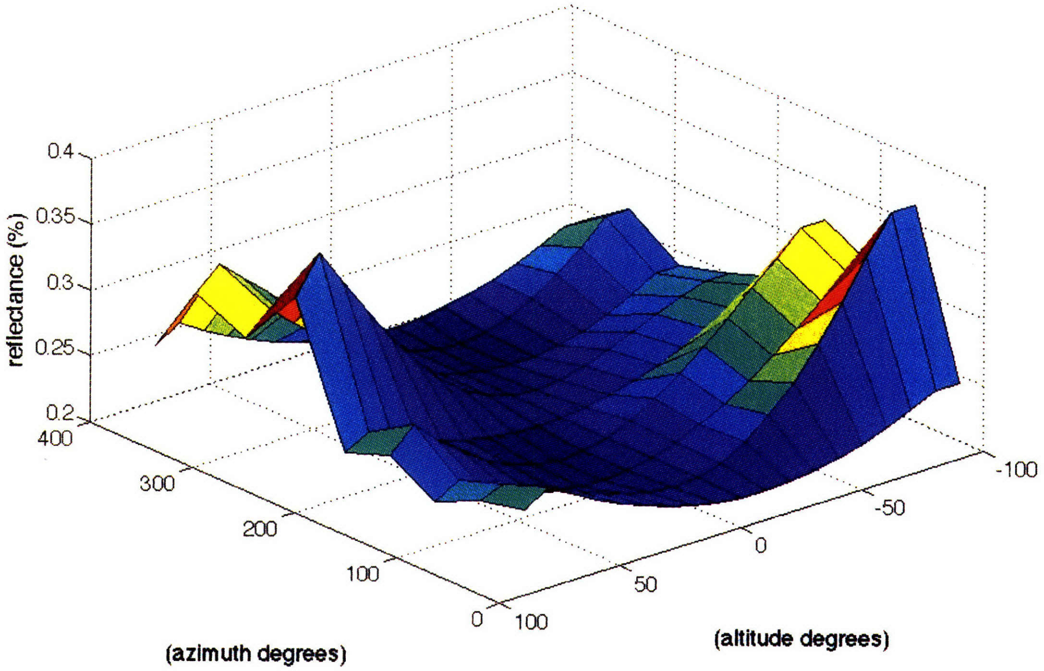

Figure 4.19 Reflectance of spheroid to 500nm radiation at all altitude and azimuth angles

5. Camera Calibrations

One of the Heliodome's major challenges is the calibration of the CCD and NIR cameras so that they act like multi-point luminance meters and spectroradiometers. This chapter describes the conversion of raw images from the CCD camera to photometric and radiometric HDR images. The calibration of the NIR camera is discussed in Appendix A.

The CCD camera was radiometrically calibrated in previous stages of the project (Gayeski 2007b), however, a short review of those results are provided in this chapter as background for the spectral estimation method explained in chapter 6. In addition, the methods, experimentation, and results of the complete photometric calibration of the CCD camera are documented here, to be used in the calculation of photometric BSDFs.

5.1 Radiometric Calibration Review

A correct radiometric calibration of the digital camera would provide the necessary link between an image's digital levels for adequately exposed pixels and a corresponding radiance for that pixel. When these radiances are combined through HDR imaging, the pixels of the HDR will form a map of the emerging light distribution from the sample, with each pixel associated to the emerging radiance in a certain direction. The first step to achieving this map is a correct radiometric calibration of the cameras.

5.1.1 Spectro-Radiometric Response

To calibrate CCD camera, images were taken of monochromatic beams of known radiances, which were then correlated with the digital output of the camera (Gayeski 2007b). The camera's response to monochromatic radiation was evaluated as a normalized digital level ($NDL_{R,G,B}$)--a red channel, blue channel, and green channel value for each pixel. Each $NDL_{R,G,B}$ was associated with a spectral exposure $h(\lambda)$, the product of the known radiance and integration time, for the tested monochromatic wavelength λ. By varying the radiance or integration time for any λ, it was possible to chart the camera's response to a range of spectral exposures.

The CCD camera's response to monochromatic radiation was found to be best expressed through a logistic dose response function:

$$NDL_{R,G,B} = \alpha + \frac{\beta}{1+\left(\frac{h(\lambda)/h^{0.3}_{R,G,B}(\lambda)}{\gamma}\right)^{\delta}} \tag{5.1}$$

where $\alpha,\beta,\gamma,\delta$ are experimentally derived constants and $h^{0.3}{}_{R,G,B}(\lambda)$ is the spectral exposure required to yield a normalized digital level of 0.3 (Gayeski 2007b). To measure the relative response of the camera across different wavelengths, it is only necessary to compare $h^{0.3}{}_{R,G,B}(\lambda)$.

5.1.2 Spectral Responsivity

The response of the camera to different wavelengths in different channels is called the absolute spectral responsivity (ASR) , $r_{R,G,B}(\lambda)$, where

$$r_{R,G,B}(\lambda) = 1/h^{0.3}_{R,G,B}(\lambda) \tag{5.2}$$

The ASR for the CCD camera has been experimentally determined in (Gayeski 2007b) by inverting the logistic response curve, and measuring radiances and resulting NDL every 25nm across the visible spectrum. As a result, it is possible to solve for $h^{0.3}{}_{R,G,B}(\lambda)$ at each of these wavelengths for each channel. The resulting absolute spectral responsivities of the red, green, and blue channels are shown in Figure 5.1.

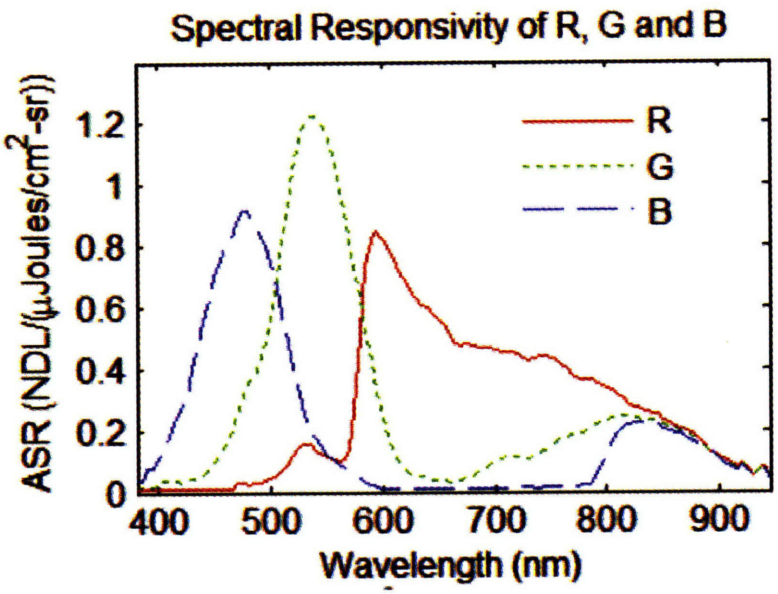

Figure 5.1 Absolute Spectral Responsivity of the CCD camera for the visible range (source: Gayeski 2007b)

For polychromatic radiation, the ASR curves must be weighted by the relative spectrum of the beam reaching the camera to give a new $h^{0.3}{}_{R,G,B,beam}$. Thus, by knowing the relative spectrum of the beam and the digital output of the camera in at least one channel, it is possible to predict the total radiance of the beam, $L_{e,beam,380\text{-}945}$, across the wavelength range where the camera is sensitive. Equation 5.3 shows this relation :

$$L_{e,beam,380-945} = \frac{h^{0.3}_{R,G,B,beam}}{t_{int}} \times \gamma\left(\frac{\beta}{NDL_{R,G,B} - \alpha} - 1\right)^{1/\delta} \qquad (5.3)$$

where t_{int} is the integration time of the camera, and $h^{0.3}{}_{R,G,B,beam}$ assumes knowledge of the relative spectrum.

However, since the Heliodome is primarily designed to characterize the distribution of radiation through *unknown* fenestration samples, it is unrealistic to require that the camera know the relative spectrum of a beam. It is most important for the camera to measure radiances from unknown spectra, and to then provide some information about what can be inferred about a sample's reflection and transmission spectra. The filtering system that leads to the estimation of these quasi-spectral properties of an unknown sample is summarized below. In chapter 6, the spectral estimation method will build upon this information to derive a closer approximation to the reflectance/transmission spectra of the sample.

5.1.3 Filtering System and Unknown Spectra

The simplest way to avoid the change in ASR due to a varying relative spectrum is to sample the beam at small *wavebands,* over which the ASR of the camera does not vary dramatically. These could be defined such that, even with the most variant spectra, monochromatic beams, the predicted radiance would differ from the true radiance by no more than a defined amount.

To define these wavebands, a filterset consisting of eight Schott colored glass short and long pass filter pairs (shown in Table 5.1 and pictured in Figure 3.4) were chosen to best isolate the flatter sections of at least one channel's ASR for each waveband (Gayeski 2007b). By designing the filters so that they only transmit in each of these wavebands, we can use the digital output from the most sensitive color channel over the waveband to approximate the radiance in band. These eight average radiances can be used to reconstruct an approximation of the spectral power distribution of the light emerging from the sample.

Waveband λ interval (nm)	Schott filter combination
380-500	GG400 (1mm), BG39 (1mm), BG25 (2mm)
450-590	GG455 (2mm), BG7 (2mm)
480-590	GG495 (2mm), BG7 (2mm)
500-650	OG530 (2mm), BG42 (2mm)
550-640	OG570 (2mm), BG39 (2mm)
570-690	OG590 (2mm), BG40(2mm)
650-850	BG665 (2mm), KG1(2mm)
800-945	RG830 (2mm)

Table 5.1: Schott filter set chosen to isolate wavebands across the visible spectrum (source: Gayeski 2007b)

In the resulting step function , each step describes the radiance of the beam in a particular waveband $\Delta\lambda_j$ (with j=1 to 8 corresponding to each of the eight filtersets), which has been reflected from the corresponding location on the hemi-spheroid. While the filters are not box-like, the waveband is a close approximation to the actual filter transmittance, achieving estimations within 10% of the true radiance in each $\Delta\lambda_j$ (Gayeski and Andersen 2007a). The radiance step curve can be changed into a quasi-spectral step curve, describing a rough spectral transmittance or reflectance estimation of the sample. Finally the spectral estimation method is applied in order to obtain finer knowledge of the spectral aspects of samples, as described in Chapter 6.

5.2 Photometric Calibration

For many samples, especially those involving neutral spectral materials or solely angular components, a photometric BSDF is all that is needed to understand the distribution of radiation in a space. This section will describe the photometric calibration of the CCD camera, enabling the Heliodome to deliver quick photometric BSDFs.

To achieve this goal, the CCD camera must act, not only act as a radiometer, but also as a multiple-points luminance meter. An appropriate luminance calibration of the camera would allow it to perceive light with the same spectral sensitivity as the human eye. While it would be easy to calculate photometric BSDFs from radiometric BSDFs, the radiometric analysis is unnecessarily lengthy, capturing images for eight filterbands and all integration times (280 images in all).

However, if it were possible to modify the camera's spectral sensitivity so that it more closely emulates the photopic function $V(\lambda)$ (Commission Internationale de l'Eclairage, 1932), the processing time for photometric measurements would be eight times faster. The first part of this section describes modifications of the raw CCD camera's spectral sensitivity that were executed in order to achieve this goal. The second describes an experimental photometric calibration that enables the instrument to associate luminances with grayscale pixel values following a method described in (Andersen et al. 2001).

5.2.1 Determination of Optimal Modified Camera Sensitivity

The CCD camera's spectral sensitivity for the red, green, and blue channel has been determined in previous stages of the Heliodome project (Gayeski 2007b). The normalized sum of all three channels is contrasted with the targeted V(λ) photopic function in Figure 5.2. It is immediately obvious that the camera is much too sensitive in the red and blue parts of the spectrum compared to the human eye. Furthermore, the equal parts addition of the three curves creates two peaks—one around 530nm from the green curve and one at 590nm from the red curve, both cradling the targeted V(λ) peak at 555nm.

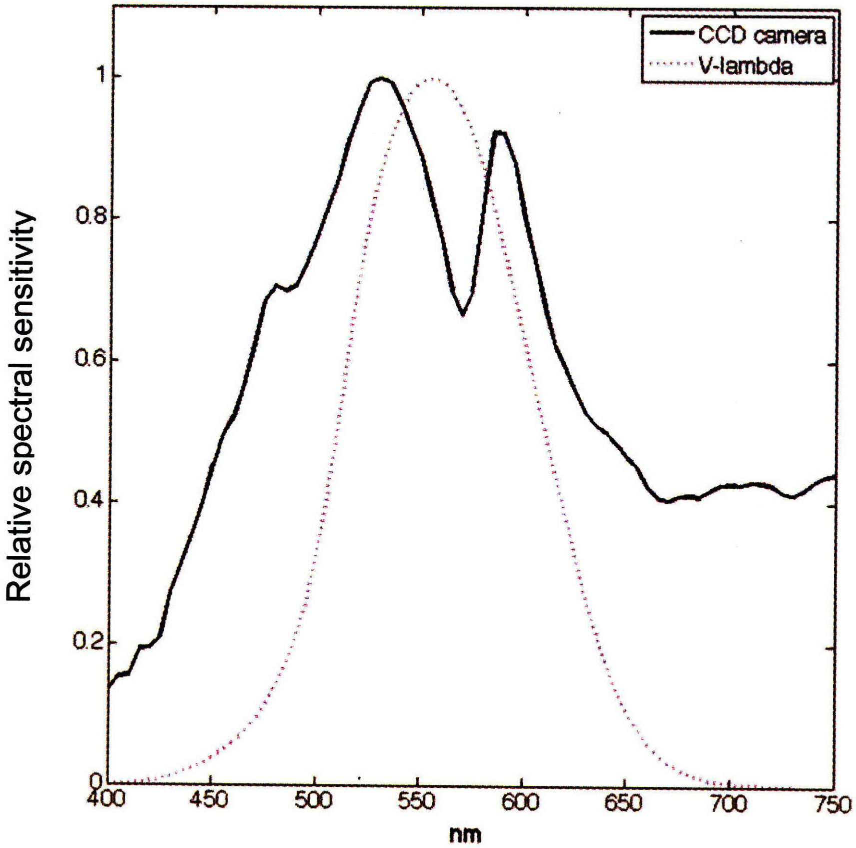

Figure 5.2: Total raw spectral sensitivity of CCD camera, as compared with V(λ), as found by adding the R,G,B channel spectral sensitivities.

In order to address these two issues, an optimization was performed, allowing autonomous scaled adjustments to the red, green, and blue sensitivity curves. To restrict the impinging signal to the photopic region, an assortment of Schott long pass and wide band pass colored glass filters were also tested in pairs. By optimizing the filter pairing, the filters' respective thicknesses, and the R,G,B scaling parameters simultaneously, it was possible to diminish the excessive sensitivity in the red and blue regions of the spectrum by eliminating those regions of radiation in the incident beam.

Two filters were chosen as a result of this optimization—GG495 at 2mm thickness, and BG40 at 2mm thickness. While other filter pairs were found that achieved a slightly improved cut-off, these two were chosen because of their availability due to time constraints. GG495, the long-pass filter, reduces the sensitivity in the low wavelength range, while BG40, a band-pass filter, gradually cut out the signal from 560 to 700 nm.

In conjunction with new scaling parameters for the red, green, and blue channel--.792, .657, and 0 respectively—the corrected response, approximating $V(\lambda)$, is shown in Figure 6.3. The function f_1' (Commission Internationale de l'Eclairage (1987)) was used to quantify synchronization between $V(\lambda)$ and the new relative spectral sensitivity $S(\lambda)$, according to Equation 6.7:

$$f_1' = 0.0093584 \cdot \sum_n \left| S(\lambda) - V(\lambda) \right| \cdot \Delta\lambda_n \qquad (6.7)$$

For the chosen filter combination f_1' was found to be 17.6%, a great improvement over the initial f_1' of Figure 5.2, 99.7%.

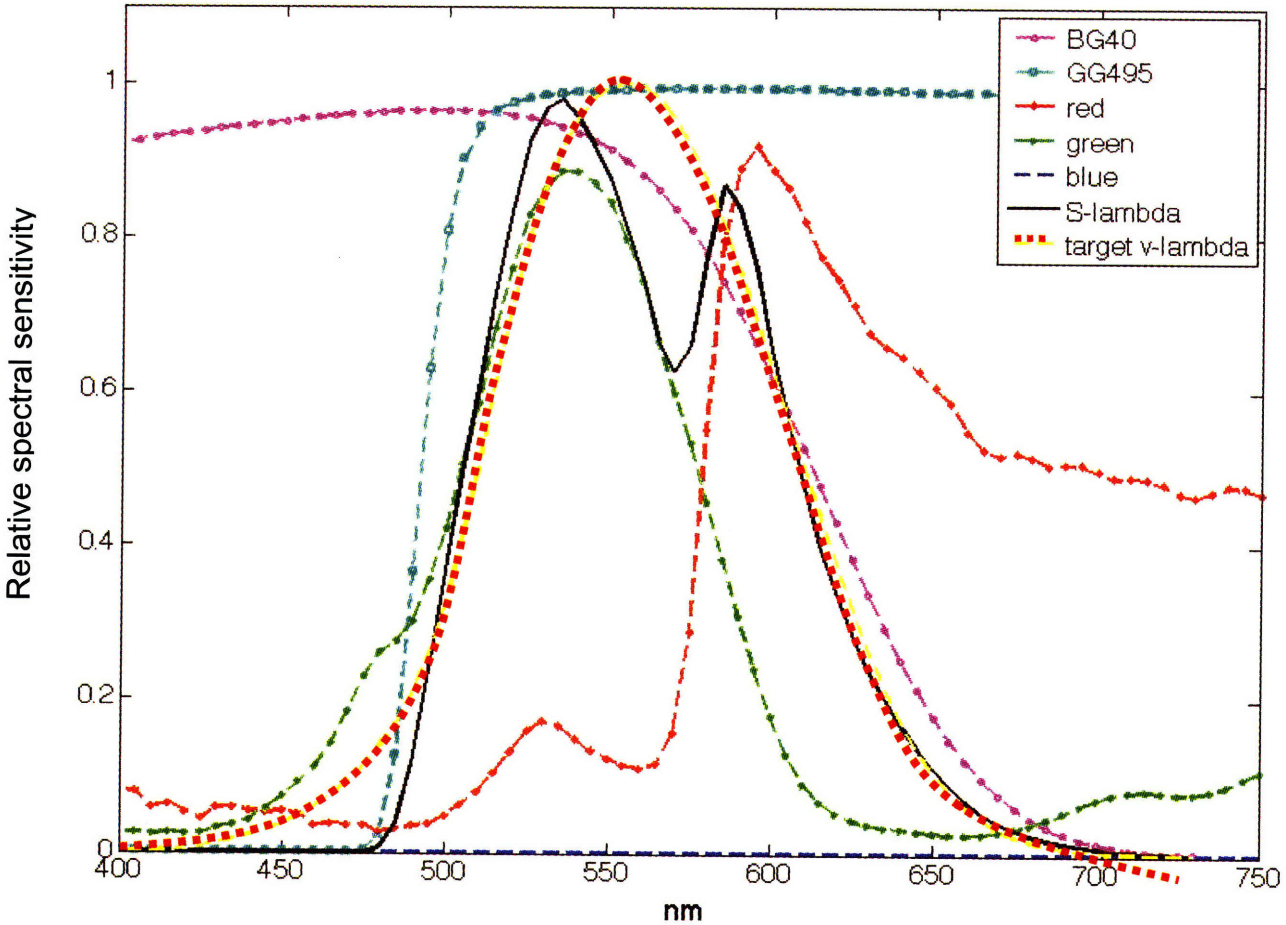

Figure 5.3: Modified spectral sensitivity of CCD camera for luminance measurements (black). Modifications due to two cut-off filters, BG40 (magenta) and GG495 (cyan), in addition to weighing the CCD camera's R,G,B spectral sensitivity curves, (shown in red, green, and blue). The modified relative spectral sensitivity more closely matches *V(λ)* (orange)

Due to the disconcerting dip in *S(λ)* around 570nm, a test was performed with hypothetical spectra to gauge the maximum error expected from this misalignment. The spectra were designed such that their total luminances were the same, though they were maximally different from each other. As shown in Figure 5.4, spec1 and spec2, peaking and dropping at the aforementioned dip, are meant to test the limits of the error expected from using *S(λ)* to predict luminance. Spec3 and spec4 more closely resemble rough spectral power distributions that would actually be tested in the Heliodome.

The result of these tests suggest an upper limit for error of around 30%, while the expected error in luminance estimation of less spiky spectral power distributions will be much lower, around 5-10%. This expected error was adequately low to still provide a meaningful photometric BSDF, and thus the chosen filters and channel scaling factors will be used in the final calculation procedure. These were also applied during the camera's photometric calibration described in the following section.

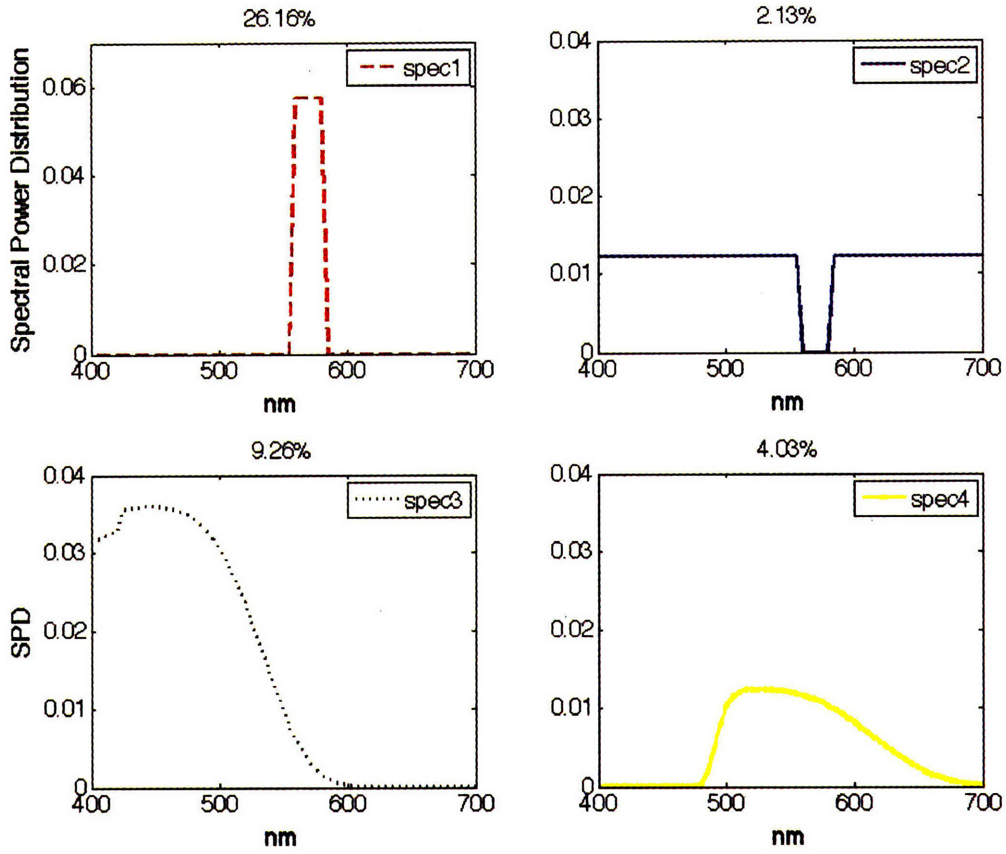

Figure 5.4: Hypothetical spectral power distributions of the same luminance and their associated errors for total luminance estimation

5.2.2 Luminance calibration

The purpose of the photometric calibration is to correlate grey scale pixel values (now from 0 to 369.5 due to the adjusted scaling parameters) with associated luminances for each integration time of the CCD camera. An experiment was set-up, as shown in Figure 5.5, with the HMI dedolight illuminating a spectralon reflectance standard, a perfectly diffusing white surface, through the designed cut-off filter pair, GG495 and BG40. The CCD camera and a luminance meter were positioned facing the reflectance standard at similar angles off the perpendicular. In order to achieve a broad range of luminance measurements from the reflectance standard, the illumination level of the beam was adjusted both through the use of spectrally selective filters and alterations of the power setting of the lamp.

For each illumination setting, yielding luminances in the range of 1.55 Cd/m^2 to 200,000 Cd/m^2, images were taken at all integration times from detection to pixel saturation. A luminance measurement was also recorded from the luminance meter and associated to the series of images.

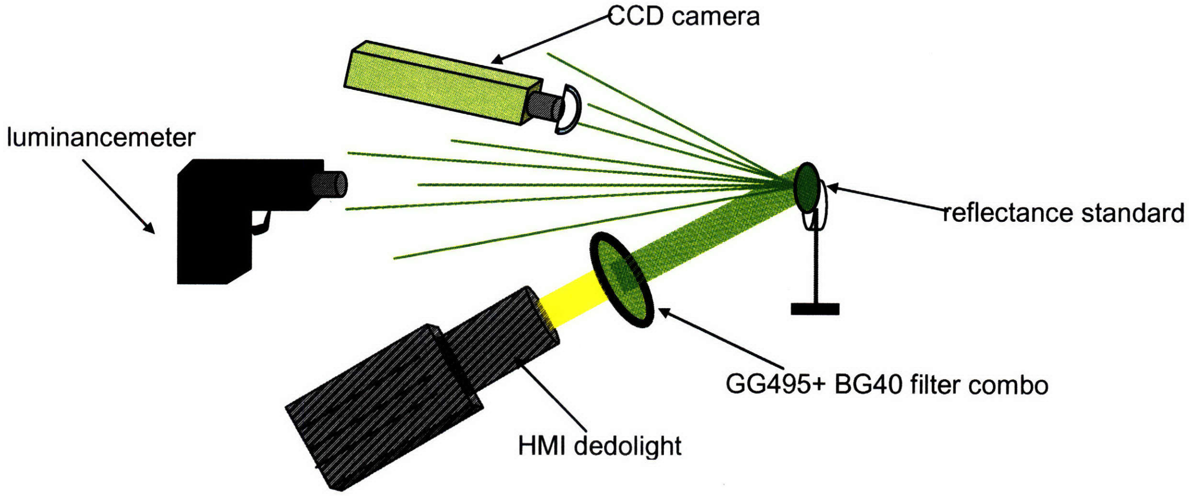

Figure 5.5: Photometric calibration experimental set-up

When the data was collected, the red, green, and blue digital levels for each pixel were each averaged over an image area of 460 pixels with consistent illumination having a standard deviation less than 3.8 digital counts (out of 255). The red and green channel's digital levels were combined using the scalar weights described in the previous section to produce grayscale values that could be normalized and associated with the measured luminance levels. Figure 5.6 and 5.7 show the normalized grayscale levels for each integration time that correspond to each measured luminance level, and their respective 10% error bars (to be described in section 5.2.3).

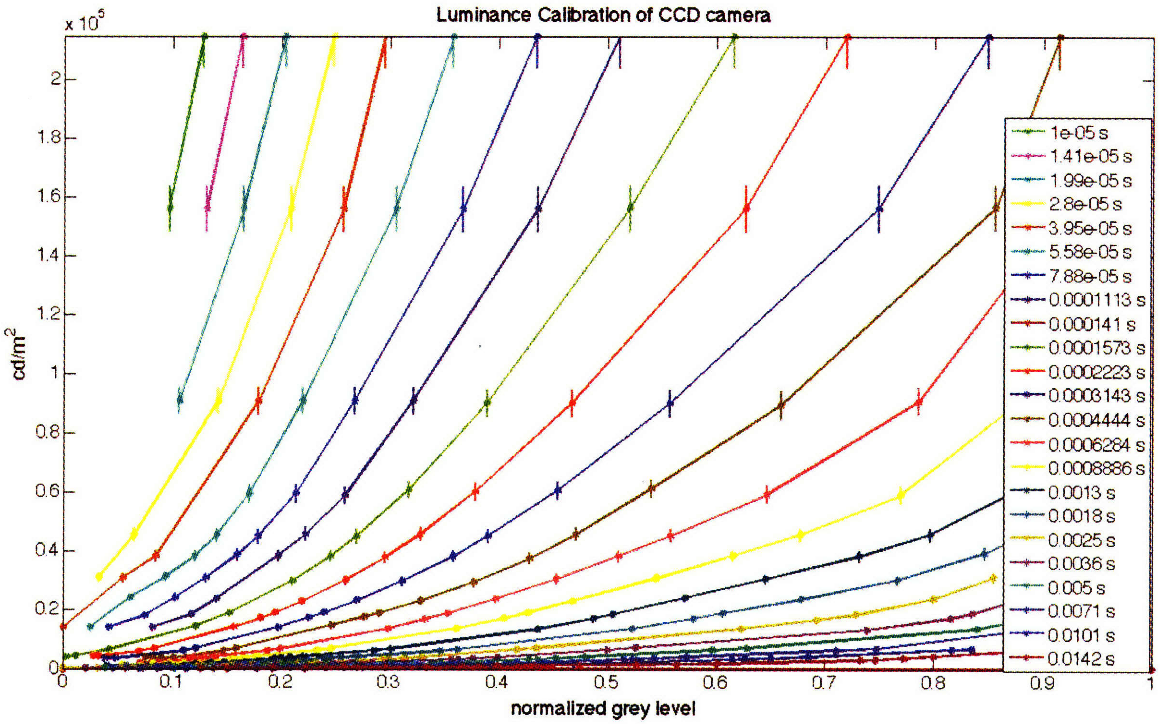

Figure 5.6 Photometric calibration of the CCD camera for low integration times + 10% error bar

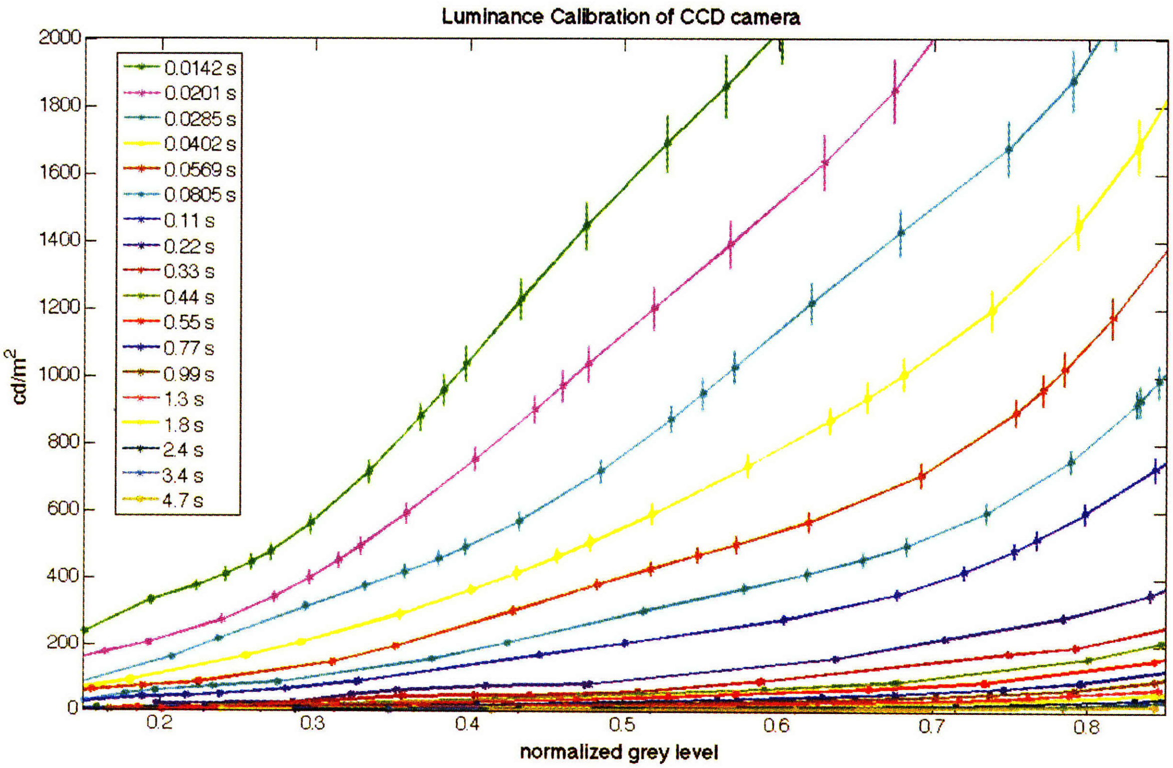

Figure 5.7 Photometric calibration of the CCD camera for higher integration times + 10% error bar

5.2.2 Photometric Validation

The luminance calibration was validated with five spectrally selective fenestration samples used to alter the HMI's spectral power distribution in different ways. These five samples consisted of two coated glazings, two applied film glazings, and one laminated sample. The HMI dedolight was transmitted through each of these spectrally unknown samples and through the cut-off filter pair to illuminate the reflectance standard. The HMI lamp settings were also altered for each sample measurement to achieve multiple luminance values for each sample, each of which was also measured by a reference Minolta luminance meter.

Overall, 100 different luminance values were captured from the illuminated standard by the CCD camera. In each of these images, the average red, green, and blue digital levels from the area of interest were translated into a grayscale value. Using the grey values and integration times from each image, the luminance calibration curves could be used to deduce the associated expected luminance. For each of the 100 images, the luminance estimate was then compared against the measured luminance from the luminance meter, as demonstrated in Figure 5.8.

All estimates fell within a 10% error range of actual luminance measurements, whereas the average error was 4.9%. It was observed that the estimated values were not predictably above or below measured luminance values, as the actual luminance values will vary depending on the spectral power distribution, and thus on the reflectance or transmittance of the unknown sample.

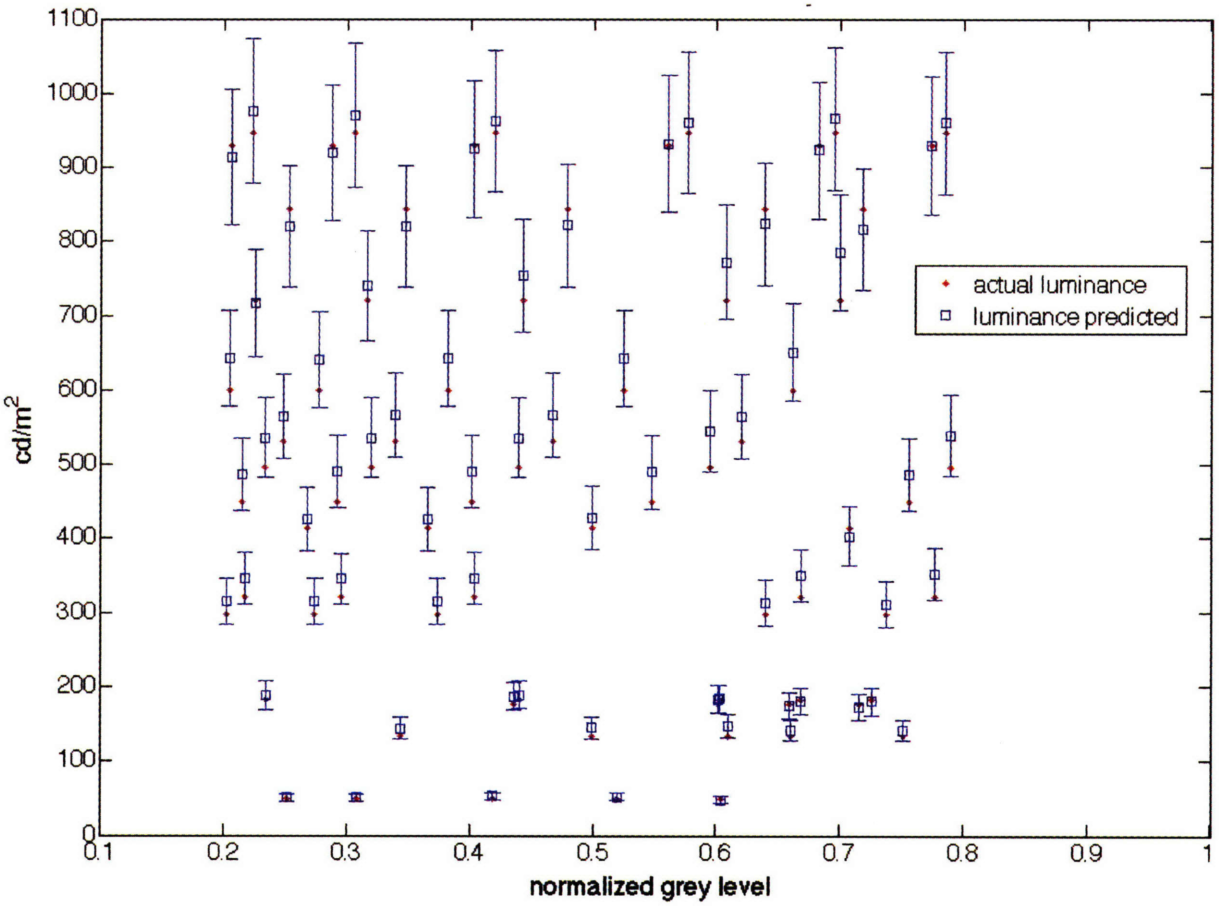

Figure 5.8 Validation of Luminance Calibration for CCD camera. Error bar=10%, Average Error=4.9%

This calibration enables each pixel in an HDR image to be associated with a luminance value, the average of the luminances predicted for each integration time in an image series documenting light detection to pixel saturation. Each phase necessary to achieve a photometric BSDF from these luminance estimations will be described in chapter 7.

6. Spectral Estimation Method

This chapter concentrates on the development of a method to estimate the reflection and transmission spectra of fenestration system materials based on the color coordinates from the tri-chromatic CCD camera when viewing the filtered light impinging on the camera's fisheye lens. This digital output is used to reconstruct a sample's spectral bidirectional transmittance or reflectance. This method will improve upon the quasi-spectral reflectance/transmittance step function developed in (Gayeski 2007b) and described in section 5.1.

6.1 Opportunities for Spectral Estimation

Previously, many glazing technologies and shading systems have been evaluated solely on their thermal properties, neglecting their effect on the Correlated Color Temperature (CCT) and color-rendering index (CRI) of incoming light. Often this neglect leads to lowered visual performance, negative impact on the environment, and little control over the color appearance of the space (Chain et. al 2001). Understanding the spectral power distribution (SPD) of emerging light is integral for control over the color surfaces and visual satisfaction of the occupants.

Spectral information is also used to control solar gains in spectrally selective glazings. These glazings are usually designed to allow maximal visible light transmission, while seasonally controlling NIR transmission to lessen HVAC loads. Through the application of a minimally emissive coating, spectrally selective glazings reduce solar heat gains in summer and heat loss in the winter. The benefits of these selective coatings include increased transparency over tinted glass, downsizing mechanical heating and cooling systems, and cost paybacks in 3-10 years (PNNL 1998). However, by combining fenestration light distribution techniques with spectral modification techniques, systems could be designed that handle the heat of light differently from the visible component. This combination has profound implications on thermal comfort and the efficient use of thermal masses.

Furthermore, though quasi-spectral radiometric measurements provide a general idea about radiation distribution in a space, a gross approximation to spectral information is inadequate for multi-layered systems. When fenestration materials are layered, their reflectance or transmittance spectra cannot be averaged over large bands, but instead must be multiplied wavelength by wavelength. Thus, an optimal result requires detailed knowledge of the spectral information of each layer in an assembly.

6.2 Spectral Estimation Methods

Of the two scanning goniospectrometers described in chapter 2, one only has the capability of creating quasi-spectral BSDFs, and the other uses spectrometers, which are expensive in both cost and image-processing time (Nieves et. al 2007).

As an alternative to traditional spectroradiometers, recently, mathematical methods have been used for the recovery or spectral information from digital images. These methods aim to estimate the spectral information of a scene from the red, green, and blue channel pixel levels of a digital image. As a result, they are especially interesting for video-based goniophotometry, though they have not been used for this application previously. Many of these methods aim to modify the standard assumption of low dimensional linear models in order to appropriately use spectral estimation in a variety of applications, such as colorimetric image archiving (Imai and Berns 1999) and computer rendering under changing lighting conditions (Maloney 1986, Connah et. al 2001).

The technique used for most spectral reflectance estimation methods is based on the principal component analysis of low dimensional linear models. Studies have shown that this technique is adequate for reconstructions of natural illuminants and situations with known camera properties (Nieves et. al 2007, Hernandez-Andres et. al 2004, Romero 1997, Maloney 1986). Spectral estimation in the Heliodome combines this a priori method with other regularization techniques to design an appropriate routine for the spectral reflection and transmission reconstruction of CFS in a goniophotometer.

6.3 Spectral Estimation of Unknown Spectra

To derive the reflection or transmission coefficients of a fenestration sample, the Heliodome's measurement process must be described mathematically. The two modes differ only in that, for reflectance measurements, the incident beam must be initially transmitted through the spheroid before reaching the sample. The spectral estimation of transmittance spectra can be seen as a specific sub-case ($\tau_{spheroid}=1$ for allλ) of the general spectral reflectance estimation method. Therefore, this section will describe the methodology in reflection mode, starting with the deliverable -- the series of filtered images taken by the camera.

6.3.1 Deriving camera digital response vector *d*

As explained in section 5.1, the digital output of the color CCD camera for each filter, $NDL_{RGB,j}$, is related to the radiance seen by the camera $L_{j,\lambda,cam}$ by a logistic dose response function, f, described in (Gayeski 2007b):

$$NDL_{R,G,B,j} = f\left(t_{int}\sum_{\lambda} L_{e,j,\lambda,cam} r_{R,G,B,\lambda}\right) \qquad (6.1)$$

where j= [1,8], λ=[380,945] in 5 nm increments, $r_{R,G,B,\lambda}$ is the CCD camera's ASR, and t_{int} is the integration time of the image. To isolate the reflection coefficients of the sample, the expression linking NDL to $L_{j,\lambda}$ must be further dissected:

$$\frac{f^{-1}(NDL_{R,G,B,j})}{t_{int}} = r_{R,G,B,\lambda} \bullet L_{e,j,\lambda,cam} \qquad (6.2)$$

The dot product, $f^{-1}(NDL_{R,G,B,j})/ t_{int}$,, can be compiled into a vector of length 24, called d for each pixel in an image:

$$d = \begin{bmatrix} f^{-1}(NDL_{R,1}) / t_{int} \\ f^{-1}(NDL_{G,1}) / t_{int} \\ f^{-1}(NDL_{B,1}) / t_{int} \\ \vdots \\ f^{-1}(NDL_{B,8}) / t_{int} \end{bmatrix} \qquad (6.3)$$

Everything in d is known from the camera's image and camera settings.

6.3.2 Deriving the spectral modifier matrix

The other side of the expression contains the unknown spectral radiance of the beam reaching the fisheye, $L_{j,\lambda,cam.}$ To isolate the reflection coefficients of the unknown sample, $L_{j,\lambda,cam}$ is represented as a product of its contributing parts. Each spectrum can be seen in Figure 6.1, and affect the relative spectrum of the initial beam in different ways depending on their flatness.

The reflectance and transmittance spectra of the spheroid, accounted for in chapter 4, vary slightly for each pixel depending on variations in the reflective coating. The spectral estimation method will therefore be described for a single pixel corresponding to an arbitrary angle $(\theta_i,\phi_i,\theta_r,\phi_r)$.

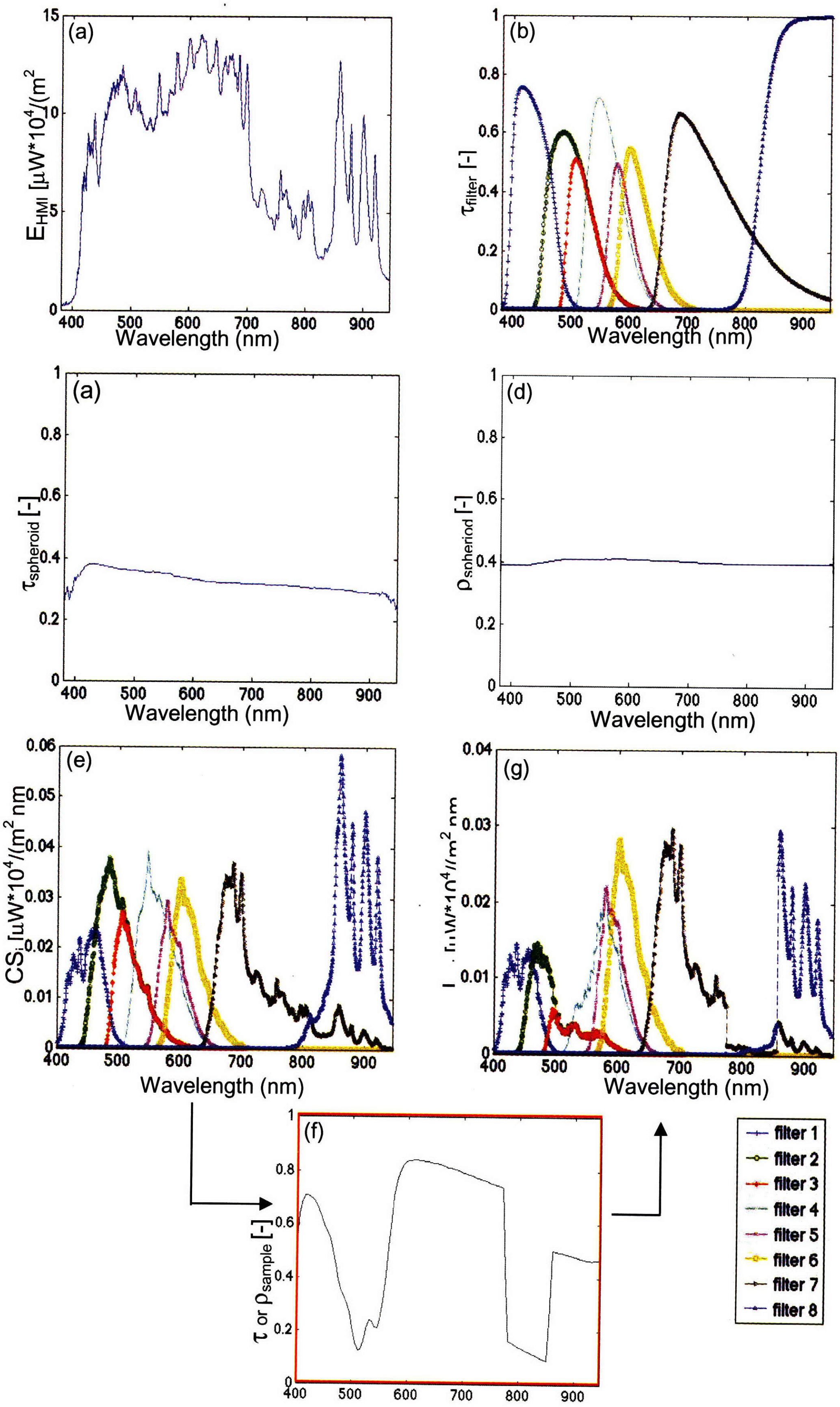

(a)
E_HMI [µW*10^4/(m^2
Wavelength (nm)
(b)
τ_filter [-]
Wavelength (nm)
(a)
τ_spheroid [-]
Wavelength (nm)
(d)
ρ_spheriod [-]
Wavelength (nm)
(e)
CS_i [µW*10^4/(m^2 nm
Wavelength (nm)
(g)
µW*10^4/(m^2 nm
Wavelength (nm)
(f)
τ or ρ_sample [-]
filter 1
filter 2
filter 3
filter 4
filter 5
filter 6
filter 7
filter 8

Figure 6.1: System spectra as a function of wavelength [nm]: (a) initial HMI spectrum (M_{HMI}), (b) filter transmittance (τ_{filter}), (c) spheroid transmittance ($\tau_{spheroid}(\theta_i,\phi_i)$, (d) spheroid reflectance ($\rho_{spheroid}$,(θ_r,ϕ_r)), (e) conglomerate spectrum ($CS_j(\theta_i,\phi_i,\theta_r,\phi_r)$), (f) hypothetical unknown sample transmittance or reflectance (τ or ρ_{sample}), (g) hypothetical final spectral power distribution reaching the camera ($L_{j,\lambda,cam}$ $(\theta_i,\phi_i,\theta_r,\phi_r)$)

The initial spectral exitance of the beam, $M_{HMI,\lambda}$ is modified as expressed by equation 6.4:

$$L_{e,j,\lambda,cam}(\theta_i,\phi_i,\theta_r,\phi_r) = M_{HMI,\lambda}.*\tau_{filter,j,\lambda}.*\tau_{spheroid,\lambda}(\theta_i,\phi_i).*\rho_{sample,\lambda}(\theta_i,\phi_i,\theta_r,\phi_r)$$
$$.*\rho_{spheroid,\lambda}(\theta_r,\phi_r)*cos(\theta_i) \qquad (6.4)$$

where

$\tau_{filter,j,\lambda}$ is the transmission spectrum of filter j

$\tau_{spheroid,\lambda}(\theta_i,\phi_i)$ is the transmission spectrum of the spheroid for an incident altitude and azimuth angle (θ_i,ϕ_i)

$\rho_{sample,\lambda}(\theta_i,\phi_i,\theta_r,\phi_r)$ is the reflection spectrum of the unknown sample along emerging direction (θ_r,ϕ_r) from a beam of incident angle (θ_i,ϕ_i)

$\rho_{spheroid,\lambda}(\theta_r,\phi_r)$ is the reflection spectrum of the spheroid corresponding to the angle (θ_r,ϕ_r)

all recorded in 5 nm wavelength increments. The symbol .* is the scalar multiplication of the elements in corresponding vector row indices, and cos(θ_i) accounts for the effect of off normal radiation.

Combining the known components of the spectrum yields:

$$CS_{j,\lambda}(\theta_i,\phi_i,\theta_r,\phi_r) = M_{HMI,\lambda}.*\tau_{filter,j,\lambda}.*\tau_{spheroid,\lambda}(\theta_i,\phi_i).*\rho_{spheroid,\lambda}(\theta_r,\phi_r)*cos(\theta_i) \qquad (6.5)$$

where $CS_{j,\lambda}(\theta_i,\phi_i,\theta_r,\phi_r)$ is the conglomerate spectrum for filterset j, or discrete spectral radiance as viewed by the camera as if there were no sample. Transforming the dot product, Eqn. 6.2 becomes:

$$\frac{f^{-1}(NDL_{R,G,B,j})}{t_{int}} = r_{R,G,B,\lambda}\left[CS_{j,\lambda}(\theta_i,\phi_i,\theta_r,\phi_r)\right]^T\left[\rho_{sample,\lambda}(\theta_i,\phi_i,\theta_r,\phi_r)\right] \quad (6.6)$$

The row vectors, $r_{R,G,B,\lambda}\left[CS_{j,\lambda}(\theta_i,\phi_i,\theta_r,\phi_r)\right]^T$, are combined in a matrix *N* corresponding with vector *d*:

$$N(\theta_i,\phi_i,\theta_r,\phi_r) = \begin{bmatrix} r_{R,\lambda}CS_{1,\lambda}(\theta_i,\phi_i,\theta_r,\phi_r)^T \\ r_{G,\lambda}CS_{1,\lambda}(\theta_i,\phi_i,\theta_r,\phi_r)^T \\ r_{B,\lambda}CS_{1,\lambda}(\theta_i,\phi_i,\theta_r,\phi_r)^T \\ \vdots \\ r_{B,\lambda}CS_{8,\lambda}(\theta_i,\phi_i,\theta_r,\phi_r)^T \end{bmatrix} \quad (6.7)$$

If ρ_{sample} is measured at 5nm intervals, the final expression:

$$N\rho_{sample} = d \quad (6.8)$$

is a linear system with 24 equations (8 filters x 3 color channels) and 114 unknown reflection coefficients that can be calculated for each pixel.

The intuitive solution to this matrix expression would be to use the pseudoinverse of N to solve for ρ_{sample}:

$$N^+ = (N^T N)^{-1} N^T \quad (6.9)$$

$$\rho_{sample} = N^+ d \quad (6.10)$$

If N were a full rank matrix measured in 5nm wavelength increments, requiring thirty-eight filters, and d were a perfectly calibrated sampling of digital responses from the camera, the pseudoinverse solution would be a perfect match. However as the pseudoinverse is highly sensitive to noise and error (Neumaier 1998, Hardeberg 1999) and a large number of filters would be both cost and time expensive, alone it is not a practical solution for our application.

Since the system is ill-posed, there are many metamers that satisfy Eqn. 6.8, i.e. many different spectral power distributions that would still correspond to the same combination of R, G and B values. Additional information is needed to weed out these metamers and find the vector that most reasonably estimates a probable ρ_{sample}.

6.3.3 Smoothness Constraint

To further constrain the problem, the solution, ρ_{reg}, approximating ρ_{sample}, can be assumed to be a smooth reflectance curve, a condition similarly used in (Li and Luo 2001, van Trigt 1990). Severe monochromatic-like peaks are very unlikely to occur in the reflectance or transmittance spectra of fenestration, so the assumption of smoothness is not overly restrictive for our purposes. As a result of this assumption, each consecutive element of the vector ρ_{reg} cannot differ dramatically from the next. Thus, we use a second difference matrix S, curtailed to address the boundary conditions:

$$S = \begin{bmatrix} 1 & -2 & 1 & 0 & 0 & 0 & \cdots \\ 0 & 1 & -2 & 1 & 0 & 0 & \\ 0 & 0 & 1 & -2 & 1 & 0 & \\ & & & & \ddots & & \\ 0 & 0 & 0 & 0 & 1 & -2 & 1 \end{bmatrix} \qquad (6.11)$$

A smooth choice for ρ_{reg} requires the minimization of the second norm $||S\rho_{reg}||_2$.

6.3.4 Regulation Methods

The problem to be solved is one of balancing these two criteria correctly. Though there will be expected errors in the radiance estimates, ρ_{reg} must still closely satisfy the linear system, minimizing $||N\rho_{reg} - d||_2$. Additionally, solutions with dramatic perturbations over small wavebands must also be eliminated by minimizing the side constraint, $||S\rho_{reg}||_2$. A ρ_{reg} is chosen that balances these two concerns such that ρ_{reg} is reasonably close to the unknown solution ρ_{sample}.

6.3.4.1 Full Rank Method

This regularized solution, ρ_{reg}, could be found using a variety of regularization methods. The first possibility is to side-step the ill-conditioning of matrix N. The condition number of N is 7436, which means that any small error in d could cause very large errors in ρ_{reg}. Thus, to achieve any sort of accuracy in ρ_{reg}, one must turn N into a well-conditioned matrix. This could be accomplished by utilizing the side constraint to construct a full-rank matrix, as in Tikhonov regularization (Tikhonov 1977):

$$min\left\|\begin{pmatrix} N\rho_{reg} - d \\ \xi S - \xi S\rho^* \end{pmatrix}\right\| \qquad (6.12)$$

Here, p^* is an initial guess of the reflectance spectra and the minimization of the norm is achieved for the best ρ_{reg}. ξ is a scale used to vary the balance between smoothness and regulation (Tikhonov and Arsenin 1977).

6.3.4.2 Truncated Singular Value Decomposition

The other option is to construct a well-conditioned *rank-deficient* matrix N_k that would reasonably approximate N (Hansen, 1987). With this method, the solution ρ_{reg} would be the one that best solves the problem:

$$min\|(\xi S)\| \text{ subject to } min\|(N_k \rho_{reg} - d)\| \qquad (6.13)$$

In rank-deficient matrices, the closest rank k approximation to N would be:

$$N_k = U\Sigma V^T = \sum_{i=1}^{k} u_i \varphi v_i^T \quad (6.14)$$

where U=(u_1, u_2... u_k) and V=(v_1, v_2... v_k) are the orthonormal singular vectors of N and ∑= diag($ø_1$... $ø_k$) are the singular values of N in non-increasing order. Because the singular values get very small as *i* approaches *k*, taking into account the first *i* singular values is the closest approximation for N achieved by a matrix of rank i. As the singular values decrease, u_i and v_i become more and more oscillatory (Hansen 1998). Since the condition number of N is the ratio of the largest to the smallest singular value, truncating N in this manner would ameliorate the ill-conditioning problem.

Using this truncated generalized singular value decomposition (TGSVD) (Hansen 1987, Hansen 1988, Hansen 1992a), the method chosen for the Heliodome's application, the solution is:

$$\rho_k = \sum_{n=112-k+1}^{112} \frac{u_n^T d\ x_n}{ø_n} + \sum_{n=113}^{114} u_n^T d\ x_n \qquad (6.15)$$

where ρ_k is the reflectance spectra estimated using the first k singular values of N, x_n is the n^th^ vector of matrix X, and $ø_n$ is the nth singular value from the generalized singular value decomposition.

While ρ_{reg} is not constrained such that all its coefficients are less than one, satisfying the linear system requires that energy be conserved, so the system would only violate this restriction if radiance values implied an almost completely transmissive or reflective sample.

6.4 Spectral Estimation Results

In order to visually understand the accuracy of ρ_k in predicting ρ_{sample} (or τ_{sample}), referenced spectra of applied film, coated, monolithic, and laminated fenestration materials were used and compared against the TGSVD solution. These referenced spectra represent the range of transmission and reflection spectra that the Heliodome might encounter, and were treated as if they were unknown samples in the instrument's set-up.

6.4.1 Finding d for Referenced Samples

Matrix N was determined, as always, independently from the sample. The vector d was derived by multiplying the conglomerate spectrum by the hypothetical sample's reflectance or transmittance spectrum. The resulting spectrum reaching the camera could be integrated to give a total radiance in each designated waveband, as described in (Gayeski 2007b). This radiance could then be converted into an exposure, $h(\lambda)$, by multiplying by an integration time that would achieve an acceptable NDL from the camera.

The exposure of the camera's detector should be weighed by the camera's spectral sensitivity, $h^{0.3}{}_{R,G,B}(\lambda)$, for each channel. The result is a response that is related to the digital output of the camera through a logistic curve, as shown in equation 5.1. Thus, the assumed reference sample yields a digital level that would be produced if the sample were actually being tested.

These normalized digital levels for each channel and each waveband and their associated integration times, are all that is needed to find the vector d. The vector d is the main clue to figuring out the unknown reflectance (or transmittance) spectrum of the sample, and is the only assumption in all of the spectral estimation method that changes between each sample. Therefore, it is of utmost importance that the camera calibration be as accurate as possible, since the response from the camera is the only link between the estimation method and the true reflectance spectrum.

6.4.2 Comparing ρ_{sample}, ρ_k, and ρ_{box}

Figure 6.2 shows a comparison between the ρ_k for large k from the spectral estimation method and ρ_{box}, the reflectance information that can be derived about a sample using only the radiance step curve. The radiance step curve refers to the CCD camera's radiance estimate from the most sensitive channel in each filterband, according to figure 5.1.

The first example shown is a filter transmittance curve, a highly spectrally variant case to test the limitations of the method. The latter is a transmittance spectrum of a window coating from the Optics 5 database (Versluis et. al 2007). In both cases, ρ_k is a marked improvement over ρ_{box} in the accuracy of the estimation to ρ_{sample}, which will be quantified in the next section.

It is important to note, especially in the first case, that these results are different than what would be achieved by solely applying a smooth polynomial fit to the quasi-spectral step curve. Solving for ρ_{sample} as a system of equations, with unknown variables at each 5nm increment measurement point allows the method to take into account finer spectral modifications within filterbands. The method also allows for multiple inflection points within large filterbands, whereas a polyfit would not. While it is difficult to asses the degree of accuracy necessary in estimating ρ_{sample} for the application of fenestration design, in the case of layered or laminated systems, it is likely that these a grossly approximate method would not be adequate.

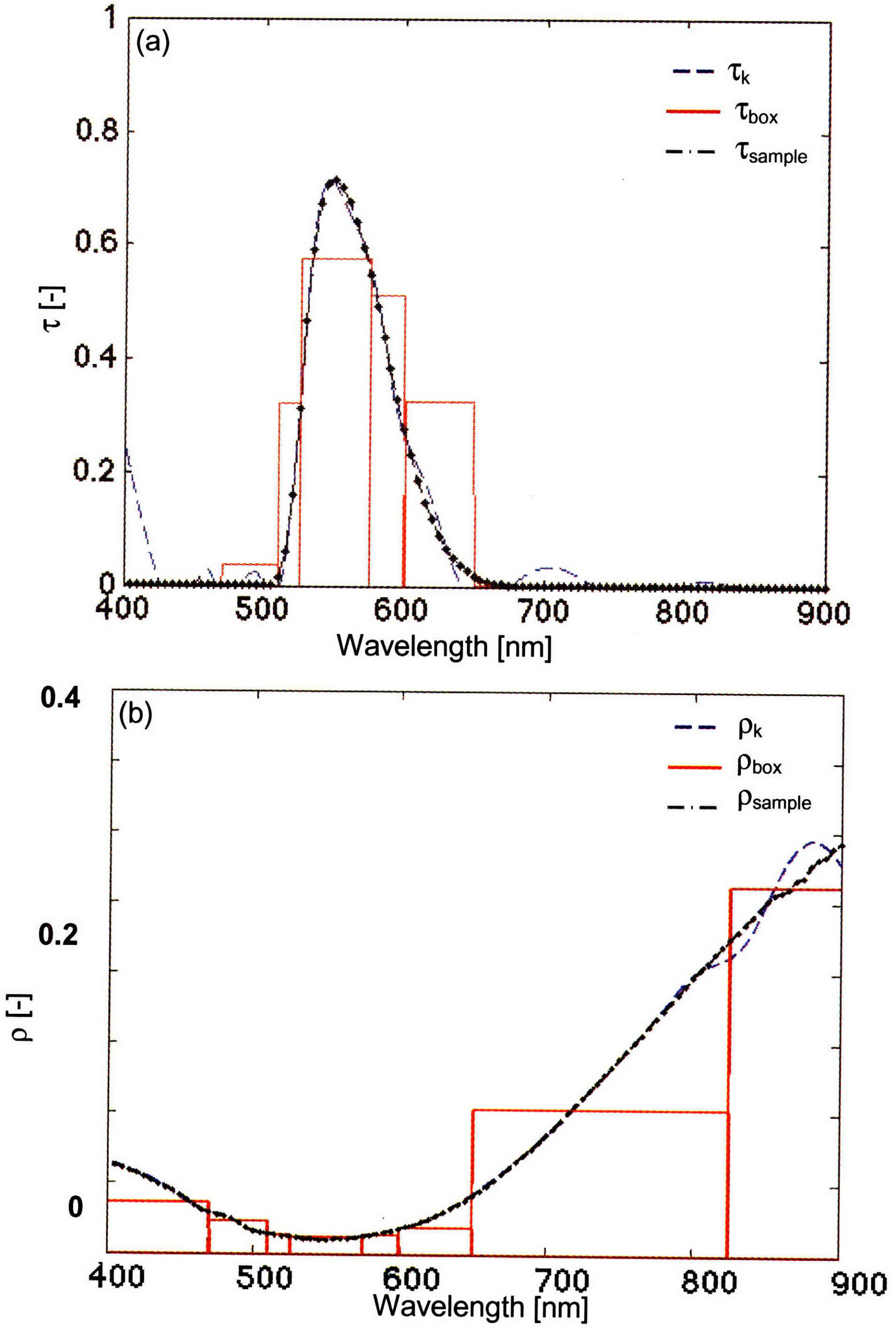

Figure 6.2: Improvement from τ_{box}, resp. ρ_{box}(—), to τ_k, resp. ρ_k(- -), in approximating τ_k, resp. ρ_{sample}(- ˙ -), using spectral estimation: (a) combination of Schott filters (transmission): GG495 (2 mm) and BG7 (2 mm) (b) V-kool applied film (reflection)

In all of the test runs, the edges of the approximation spectrum (around 400nm and 900nm) are consistently the most "off". This is due to the low sensitivity of the camera in those areas for all color channels, and the exclusion of the boundary conditions in the S matrix. Because the estimation is only as good as the NDLs predicted by each channel, a low sensitivity may yield higher errors in radiance prediction, and thus, higher errors in spectral estimation as well.

The main limitation of the method occurs when there are rapid oscillations that occur over less than 5nm wavelength intervals. Because the elements in each row of M, and the elements in ρ_k are measured at 5nm wavelengths, and because of the added smoothness criteria, rapid oscillations are often not estimated as well using the spectral estimation method. However, severe monochromatic-like peaks are very unlikely to occur in the reflectance or transmittance spectra of fenestration. For the purposes of the Heliodome, these fits are adequate.

6.5 Theoretical Validation of Spectral Estimation

It is vital that the camera calibration be as accurate as possible, since the response from the camera in all three channels is the link between ρ_k and ρ_{sample}. However, due to the limits on radiometric accuracy that non-theoretical filters impose on the NDL measurements, the spectral estimation method must plan for error contributions to the vector d.

These errors create a perturbed $\bar{d}$, from which reflectance spectra estimated using the first k singular values of N, $\bar{\rho}_k$, must be inferred. Figure 6.3 shows a comparison of ρ_k from d, with the best manually chosen $\bar{\rho}_k$ from $\bar{d}$, the same vector with added randomly distributed noise. In these hypothetical examples, when $\bar{\rho}_k$ is optimally truncated, it converges towards ρ_k. The question is, then, how to choose k optimally.

It is useful to identify the types of error introduced into the approximated solution. The first of these errors is associated with the camera's calibration, and can be written as the difference:

$$\bar{d} - d = \varepsilon \qquad (6.16)$$

Where d is the unperturbed vector and where ε is a random error vector. The second is comprised of the errors inherent in the regularization approximation.

A graphical tool called an L-curve (Hansen 1992b, Hansen and O'Leary 1993) plots the semi-norm of both contributions. With an L-curve, one can find the minimization point, where $\bar{\rho}_k$ should be least affected. When plotted on a log-log scale, these graphs have a characteristic L-shape, where the corner marks the minimization point. Here, the vertical component (contributions from $\|S\bar{\rho}_k\|$) meets the horizontal component (contributions from $\|N\bar{\rho}_k - d\|$).

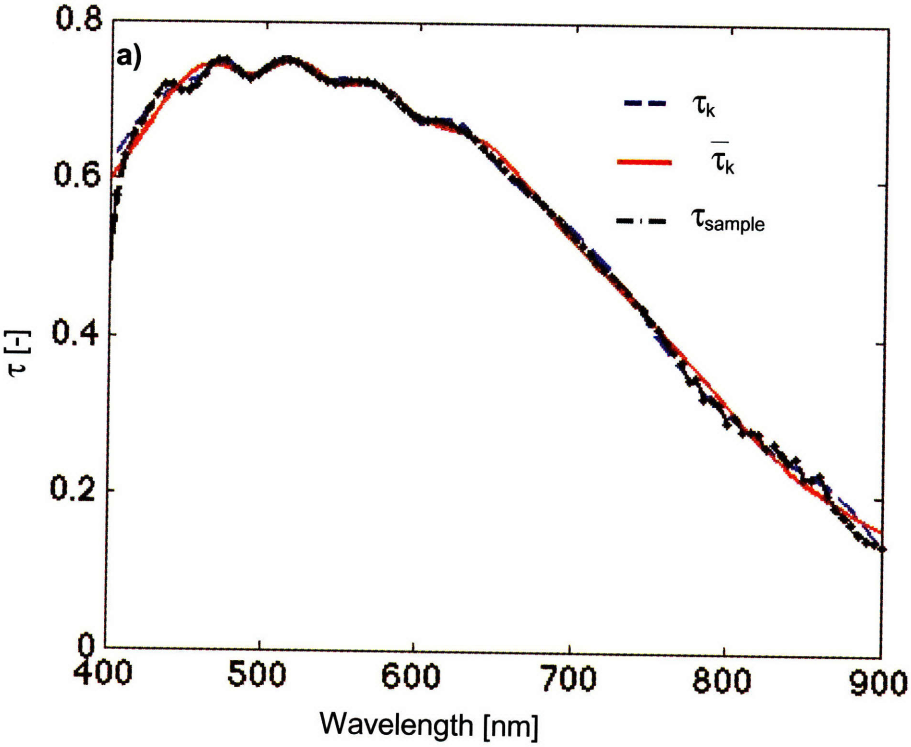

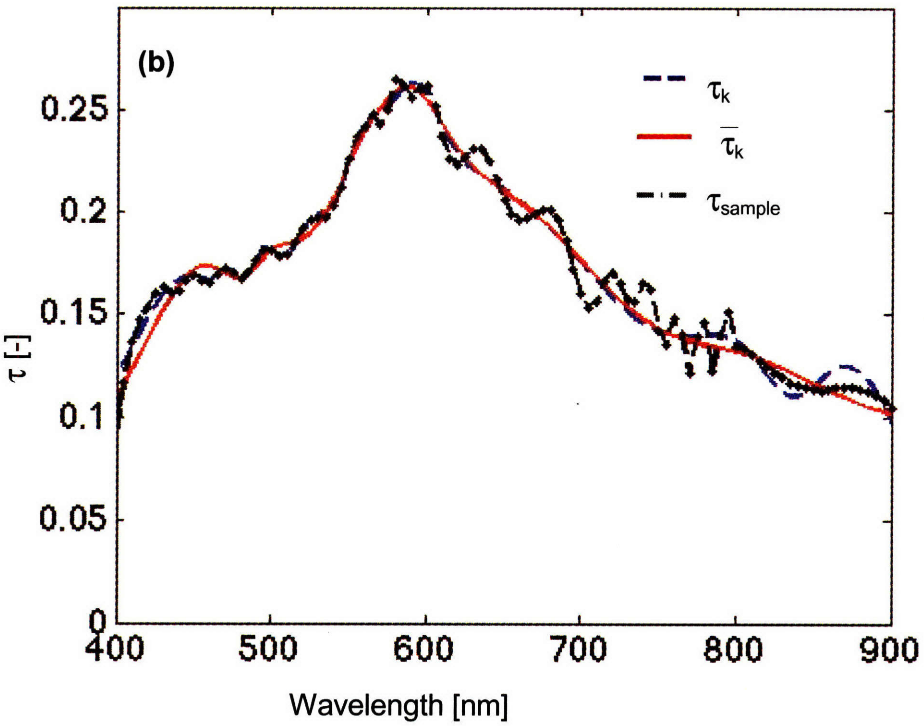

Figure 6.3: Comparison of an optimally chosen $\bar{\tau}_k$ (—) , with τ_k (- -) and τ_{sample} (- ˙ -) for: (a) a sample of V-kool applied film and (b) a solar guard bronze applied film

As demonstrated in the series of truncations for the coated sample, shown in Figure 6.4, as k increases and $ø_n$ decreases, the estimation ρ_k begins to fluctuate noticeably. This is due to the contribution of the perturbation error ε for small singular values. However, when k is too low, the regulation error is high and $||N \bar{\rho}_k - d||$ does not adequately approximate ρ_k. Thus, the L-curve for this sample, shown in Figure 6.5, is used to determine the appropriate value for k, in this case k=11, so as to get an optimal $\bar{\rho}_k$ for the given sample.

When compared with ρ_{box} the truncations achieve significantly closer approximations to ρ_{sample}. By averaging the distances, one can calculate the error reduction of $\bar{\rho}_k$ over ρ_{box}:

$$\frac{\left\|\rho_{box} - \rho_{sample}\right\|_2 - \left\|\bar{\rho}_k - \rho_{sample}\right\|_2}{\left\|\rho_{box} - \rho_{sample}\right\|_2} \qquad (6.17)$$

For the coating sample shown in Figure 6.6, this error was reduced by 94%, for the chosen $\bar{\rho}_k$ approximation. Such high error reductions can commonly be achieved for samples that rapidly vary within a given waveband, as in the 650-850nm waveband for the given example.

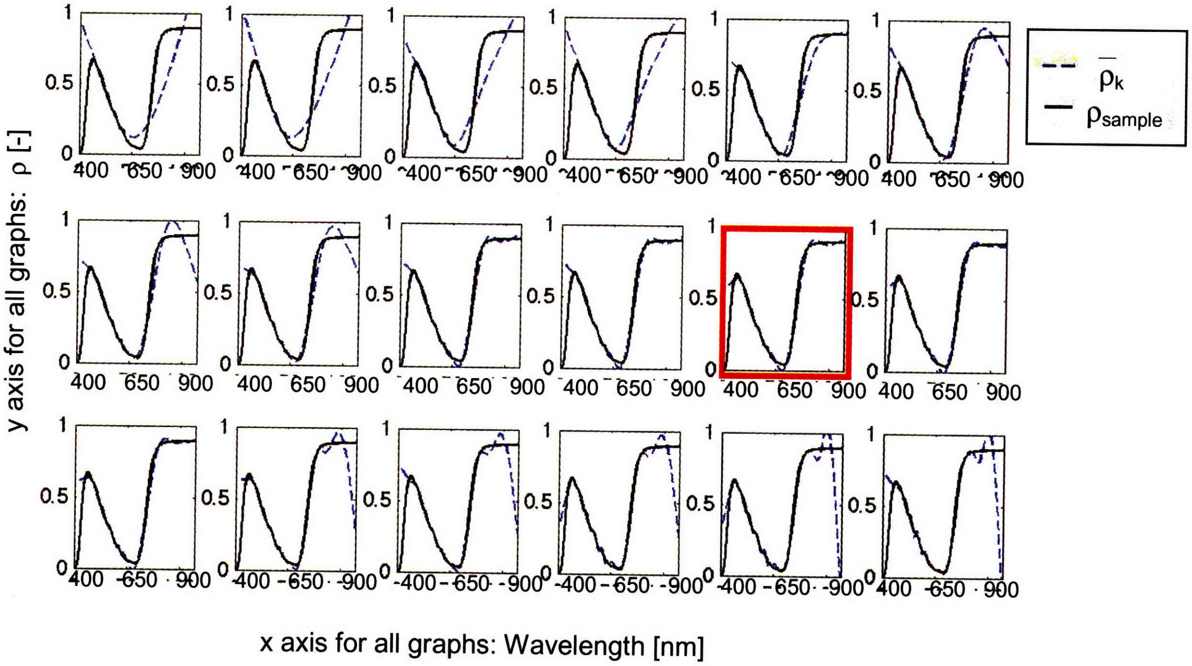

Figure 6.4 Iterations of $\bar{\rho}_k$ for k=1 to 18 for a coated sample, in transmission (solar guard royal blue applied film, 3 mm thick) with k=11 highlighted

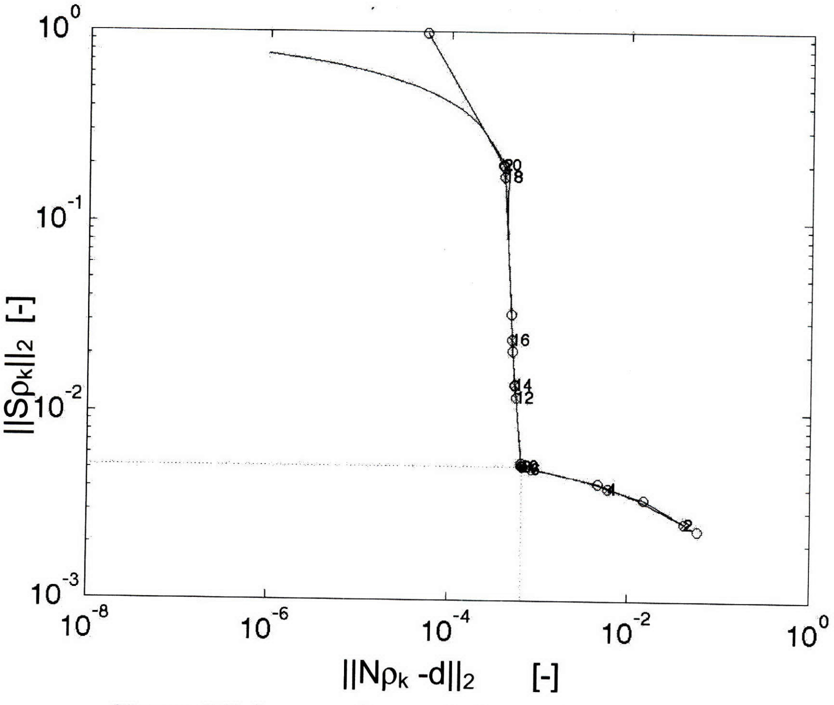

Figure 6.5: L curve for coated sample, minimizing at k=11

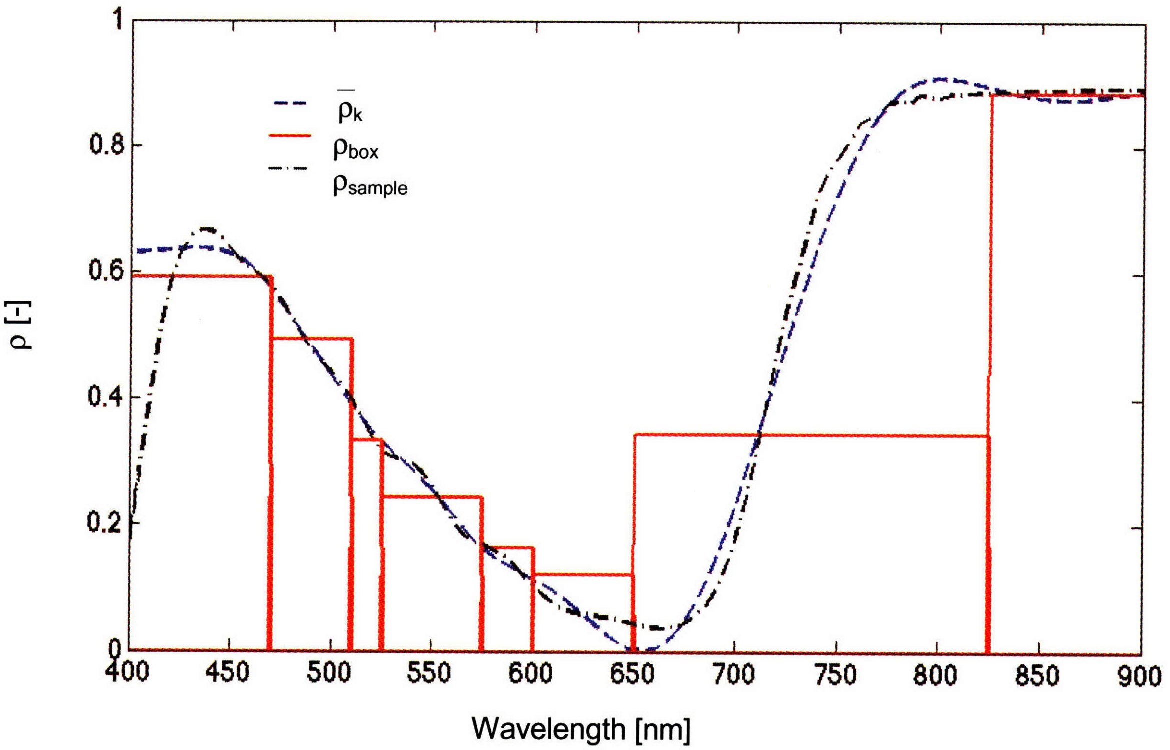

Figure 6.6 85% improvement of $\bar{\rho}_k$(- -) over ρ_{box} (—) compared to ρ_{sample} (- ˙ -) for a coated sample

It is important to note that a metamer of the spectrum resulting from the ρ_{sample} in figure 6.6 would not be a satisfactory solution. One could imagine a metamer (or spectral distribution of the same color) whose R, G, and B digital levels in each filterband were the same as the spectrum in Figure 6.6. However, because the filterbands are so small, this metamer would almost always be less smooth than the chosen $\bar{\rho}_k$. It would also not maintain a minimum $||N\ \bar{\rho}_k - d||$, since $\bar{\rho}_k$ is measured at 5nm increments. Thus, it is unlikely that a metamer would ever be estimated over the correct $\bar{\rho}_k$ in the spectral estimation method.

An error analysis was performed for 48 reflectance and transmittance spectra chosen from four fenestration categories documented in the Optics 5 database. In each case, the improvement of $\bar{\rho}_k$ over ρ_{box} was calculated according to equation 6.17, along with a smoothness quotient:

$$Q_s = \sum_{n=2}^{112} \left| \left(\rho_{sample,\lambda,n+1} + \rho_{sample,\lambda,n-1} \right) - 2\rho_{sample,\lambda,n} \right| \quad \text{with } \rho_{sample,\lambda,n} \in \rho_{sample,\lambda} \qquad (6.18)$$

and a flatness quotient:

$$Q_f = \left| min(\rho_{sample,\lambda}) - max(\rho_{sample,\lambda}) \right| \qquad (6.19)$$

Smooth spectra were defined as having Q_s<0.1 and flat quotients were defined as having Q_f less than 0.1.

By categorizing the samples as described above, it was possible to identify the types of samples that would benefit most from being analyzed under the spectral estimation method, or the % improvement over ρ_{box}. While the % improvement is a good measure of the spectral estimation method's achievements in gaining information over the previous quasi-spectral method, it is not a measure of spectral agreement. To quantify the actual fit between $\bar{\rho}_k$ with ρ_{sample}, (independent of the improvement over ρ_{box}), the function f_1' (CIE (1987)) was also calculated for each spectral estimation.

The average improvement of $\bar{\rho}_k$ over ρ_{box} for all 48 spectra was 58%; 51% for reflectance spectra and 73% improvement for transmittance spectra. For the same samples, the average f_1' was 9.4%. Broken up by glazing type, the average improvements were 69% for the applied films, 75% for coatings, 50% for monolithic samples, and 37% for laminates. This equated to a f_1' of 9.8% for applied films, 8.7% for coatings, 9.1% for monolithic samples, and 16.7% for laminates.

Greater improvements are mostly due to differences in smoothness and variance. The tested applied films in particular, such as Solis and Solarguard colored films, had less smooth reflectance and transmission spectra, with an average Q_s of 0.6 compared to Q_s's around 0.3 for the other three categories. In fact, when categorizing the samples according to these spectral properties, fluctuating spectra achieved an average improvement of 68%, compared to only 35% for samples with smooth spectra. Also variant spectra achieved an average improvement of 70% compared to 32% for samples with flat spectra.

It should be reemphasized that smaller reductions in error are not indications of poor spectral fits, but instead may indicate that ρ_{box} was initially a closer estimate to ρ_{sample}. The f_1' for smooth samples (6.8%), for example, was actually lower than for fluctuating samples (15.9%) , though the relative improvement was greater for fluctuating samples. For example, for the reflectance spectrum shown in Figure 6.7, the sample yielding the lowest percent error reduction, a dark grey laminate, was essentially constant.

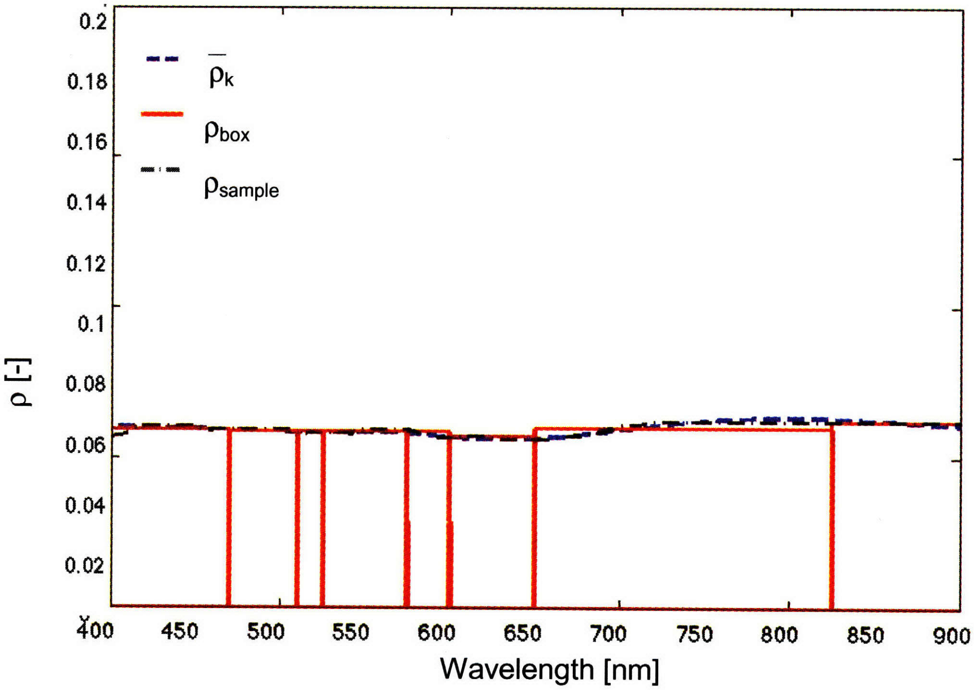

Figure 6.7 23% error reduction on the spectral reflectance of an essentially neutral sample (Versalux blue monolithic)

6.6 Experimental Validation Using Spectrally Selective Samples

The spectral estimation method was also validated by the use of eight spectrally selective samples gathered from a variety of fenestration material manufacturers. The materials were a mixture of applied film samples, coated glasses, and laminate configurations and were assumed to be generally representative of the larger body of glazing materials used in complex fenestration systems. Their transmittance spectra are shown in Figure 6.8.

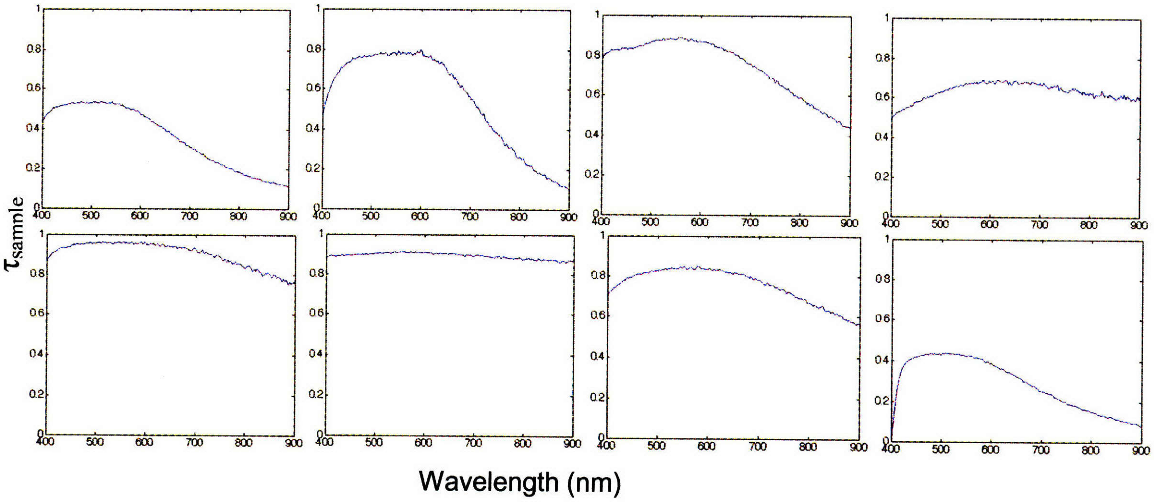

Figure 6.8 Transmitted spectra of tested samples (from top left to bottom right): 4C4 (applied film), 5E4 (applied film), 6NCOK (applied film), H8.5 (coated), H8.1(coated), H8.2 (coated) , H8.3 (coated) , Vanceva (laminate)

By performing the validation with real samples, actual images from the Kappa color CCD camera calibrated for the Heliodome could be used. To isolate the spectral estimation method and examine its soundness apart from the other components of the Heliodome, this experimental validation was realized without the spheroid, whose geometry and coating characteristics were still being improved at that time. Also, since transmitted light can be measured more easily and accurately than reflected light, these samples were analyzed in transmission mode only for this validation exercise, but the results are equally applicable to both modes.

As shown in Figure 6.9a, a USB2000 spectrometer was used to measure each sample's spectral transmission coefficients across the 380 to 900nm range. The emittance spectrum of a tungsten lamp was compared before and after transmission through the sample. The spectrometer was also used in conjunction with the filters to find the absolute spectral power distribution (SPD) of the beam after it has been transmitted through each filter and the unknown sample. The integral of these SPDs is the true radiance in each waveband.

The sample's now known (measured) transmission spectrum could then be compared with the spectrum predicted when the camera's digital levels were used as inputs into the spectral estimation method for a series of images taken at different exposures in each filterband.

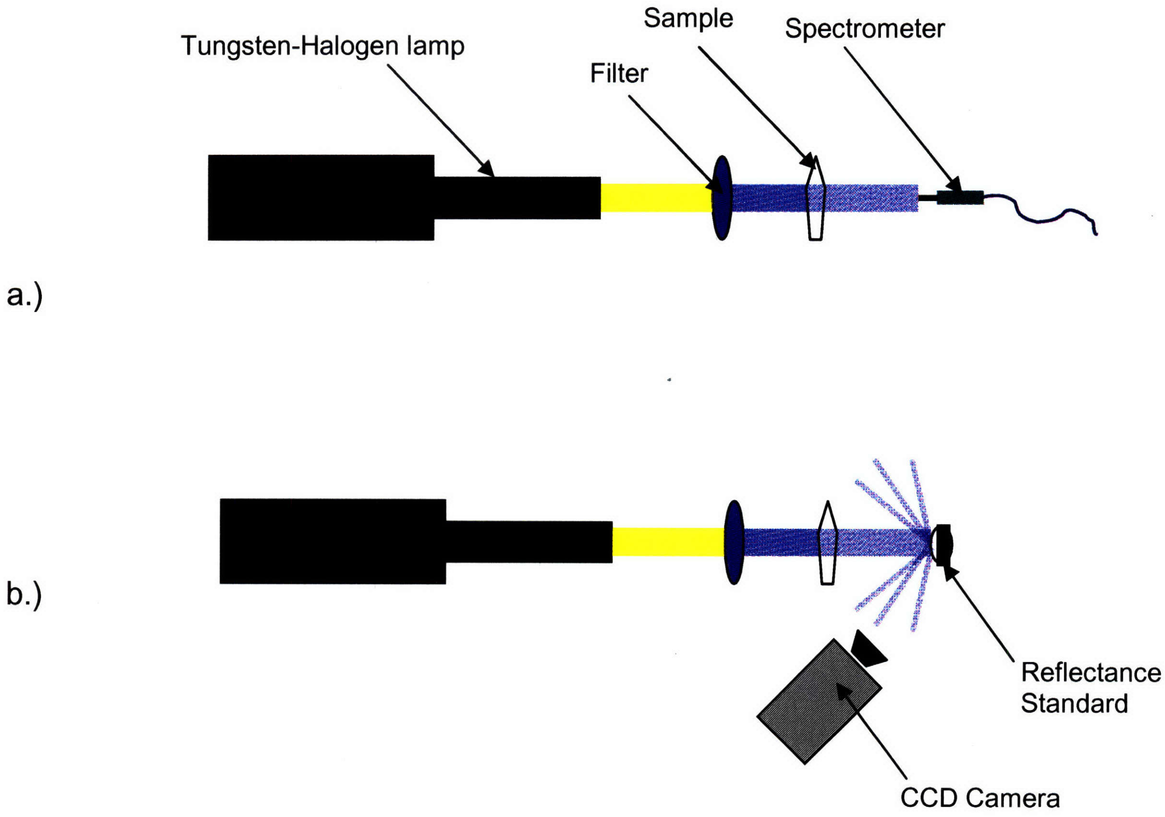

Figure 6.9: (a) Experimental set-up to measure the sample's spectral transmission coefficients, using a spectrometer; (b) Estimation of filterband radiance with digital camera

The camera was set-up facing a spectralon coated diffusing reflectance standard positioned behind the unknown sample, as shown in Figure 6.9b. For each filter, images were taken of the standard at exposure times ranging from first detection to pixel saturation. The digital levels registered by the most sensitive "best" channel were then linked to a total radiance estimate for each filter interval. When compared with the spectrometer measurements, these estimates were within 10% of the true spectral radiance. The total radiance estimates for each filter interval were also directly related to the rough step function, ρ_{box}.

One advantage of the spectral estimation method over this rough step function is its use of all the registering channels in each filter interval, instead of only the prescribed "best" channel. This allows the spectral reflectance or transmittance curve to be further refined by secondary channels yielding reasonably close radiance estimates in each filterband.

Among the nine tested samples, the spectral estimation method achieved an average improvement of 54% over the quasi-spectral estimation, ρ_{box}. Similarly to what was observed with hypothetical samples, flat transmission spectra had the lowest relative improvement at 35.3%, such as for sample H-8.3, a monolithic clear fenestration material. Also, as shown in Figure 6.10, the smooth, yet variant, coated sample C4 gains a 71% improvement over ρ_{box} with an f_1' of 3%.

Considering the large error component from the camera, the method should achieve the lowest f_1' values between $\bar{\rho}_k$ and ρ_{sample} for smooth samples. This error component forces the method to truncate the estimation early, at k=2. With fewer singular values, the method more easily estimates smooth transmission and reflection spectra. As most fenestration materials do not have sharp spectral shifts, this tendency is generally benign.

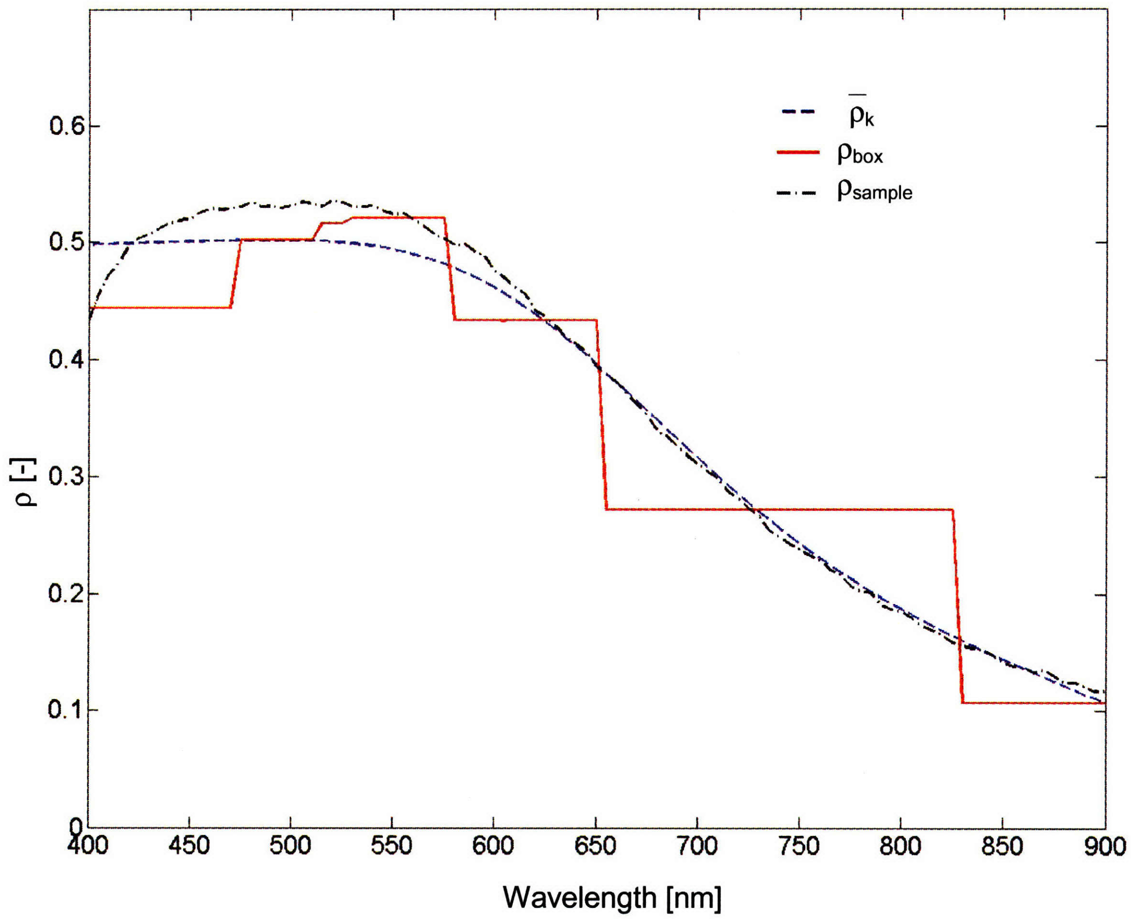

Figure 6.10: 71% error reduction in sample with coating C4

General trends in relative improvement, however, are harder to predict for real samples, since *both* ρ_k and ρ_{box} now contain an error component, unlike the ρ_{box} estimations discussed in section 6.5. As shown in Figure 6.11, even nearly flat samples can achieve 70% improvements. In this case the improvement is high because of the inaccuracy of ρ_{box}. The f_1' estimate for this sample is also still very good, at 4%. For flat samples, a smooth ρ_k easily results in grand improvements if the 10% error contribution from the camera manifests itself in alternating over and under-predictions for each waveband of ρ_{box}.

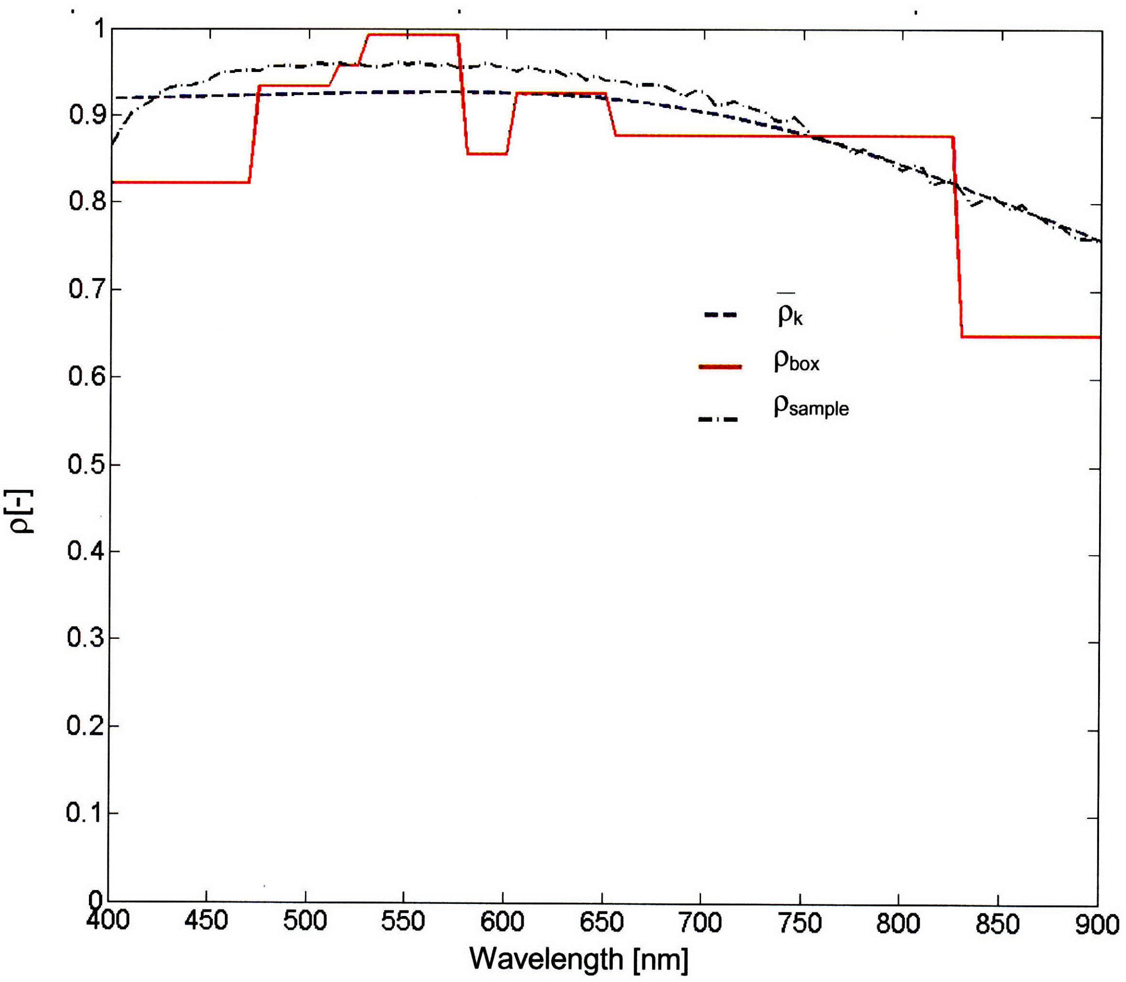

Figure 6.11: 70% error reduction in monolithic sample H-8.2

6.7 Spectral Estimation in Context

The spectral estimation method fits into the larger context of the Heliodome, by providing the spectral information needed to turn quasi-spectral BSDFs into full spectral radiometric BSDFs. The spectral estimation result, ρ_{sample}, is calculated for each pixel. When each pixel is spatially calibrated to correlate to a sample emerging angle, it can be mathematically shown that $\rho_{sample,\lambda}(\theta_i,\phi_I,\theta_r,\phi_r)$

$$BSDF_{e,\lambda}(\theta_i,\phi_i,\theta_r,\phi_r) = \frac{L_{e,\lambda}(\theta_i,\phi_i,\theta_r,\phi_r)}{E_{e,\lambda}(\theta_i,\phi_i)} \qquad (6.20)$$

where $L_\lambda(\theta_i,\phi_i,\theta_r,\phi_r)$ is the sample's emerging spectral radiance discretized at 5nm increments, and $E_\lambda(\theta_i,\phi_i)$ is the irradiance on the sample for each incident angle (θ_i,ϕ_i). $E_\lambda(\theta_i,\phi_i)$ and $L_\lambda(\theta_i,\phi_i,\theta_r,\phi_r)$ can be calculated from aforementioned known quantities:

$$E_{e,\lambda}(\theta_i,\phi_i) = M_{HMI,\lambda}.*\tau_{spheroid,\lambda}(\theta_i,\phi_i)*cos(\theta_i) \qquad (6.21)$$

$$L_{e,\lambda}(\theta_i,\phi_i,\theta_r,\phi_r) = M_{HMI,\lambda}.*\tau_{spheroid,\lambda}(\theta_i,\phi_i).*\rho_{sample,\lambda}(\theta_i,\phi_i,\theta_r,\phi_r)*cos(\theta_i) \qquad (6.19)$$

When these two quantities are divided, all that remains is $\rho_{sample,\lambda}(\theta_i,\phi_i,\theta_r,\phi_r)$, which is not actually a reflectance or transmittance at this stage, but a bidirectional spectral distribution function, measured in units sr^{-1}.

Thus, this method completes the spectral radiometric BSDF calculation. Useful especially for multi-layered CFS design, the spectral characterization of each component in a fenestration system could clarify the overall spectral reflectance and transmittance of the system. Since component spectra are multiplied on a wavelength by wavelength basis, average or non-spectral reflectance and transmission coefficients would be ill-suited to describe the effectiveness of the system as a whole.

Additionally, spectral information as it is related to a directional distribution of solar radiation and visible light is especially relevant in the design of passive heating and lighting strategies. The combination of directional and spectral information opens up new options for optimal design tactics, and deserves to become more readily accessible as complex fenestration systems become integrated into new simulation software. In hopes of addressing these informational voids, the spectral estimation method will be integrated into the Heliodome in its final form, as described in the next chapter.

7. Estimating BSDFs for Spectrally and Angularly Selective CFS

In order to frame this process from image acquisition to deliverables, the flowchart shown in Figure 7.1 maps both the spectral radiometric and photometric BSDF acquisition and processing methods. Section 7.1 will outline the spectral radiometric BSDF calculation (boxes in dark grey); while section 7.2 outlines the photometric BSDF calculation (boxes in white). Any automation steps used in both processes are highlighted in light grey.

Each process assumes an uncropped image size of 1380 x 1027 pixels. Images will be taken in a range of integration times between 3.95e-5 seconds and 3.7 seconds (a total of 35 integration times). Each phase necessary to achieve BSDF results was automated in Matlab® to achieve a full automation of the photometric and spectral radiometric BSDF assessment. While the image acquisition and final format of the data and interface must still be manipulated for user-friendliness and ease of integration into existing fenestration databases, the backbone of the assessment calculation process has been developed and is described in this chapter.

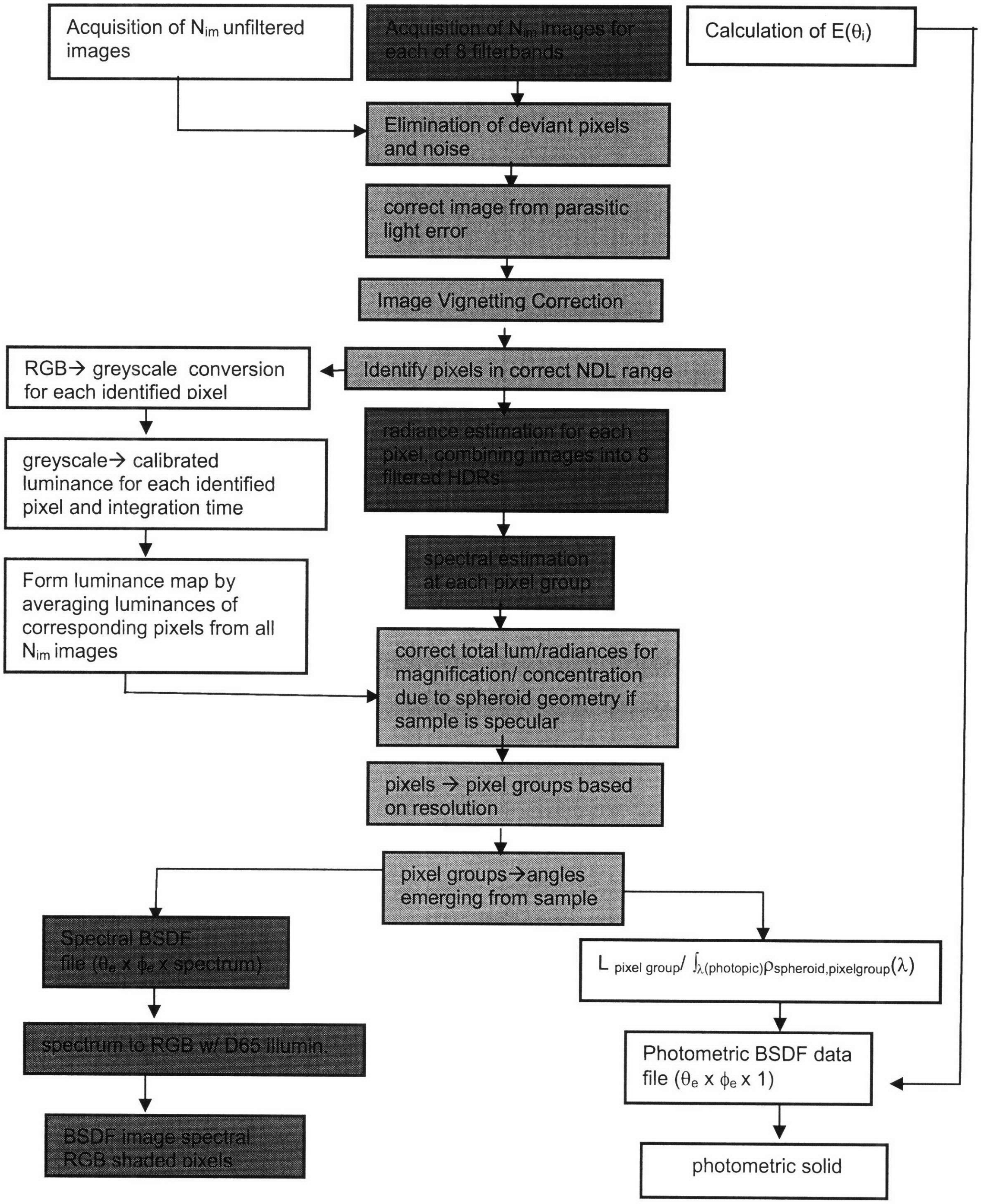

Figure 7.1 Automation flowchart for calculating photometric and spectral radiometric BSDFs

7.1 Spectral Radiometric BSDFs

Two deliverables are expected from the spectral radiometric BSDF (sBSDF) calculation. The first is numerical--a matrix of dimension m x n x 114, describing the spectral transmittance or reflectance of the sample at each of m x n emerging direction pairs (θ_r,ϕ_r) for an incident beam at (θ_i,ϕ_i). The second is graphical for efficient visualization of the results--a 3D spectral radiometric solid, demonstrating the angular and spectral reflectance or transmittance properties of the sample. Together, these two deliverables will provide both detailed numerical information and an intuitive illustration of the sample's distribution properties.

In the automation of a sBSDF calculation, first the input parameters are selected. The user defines the incident angle (θ_i,ϕ_i), investigation mode (reflection or transmission), result type (photometric or spectral radiometric), sample diameter D, and data resolution in emergence ($\Delta\theta_r,\Delta\phi_r$). The table's motors are arranged to accommodate image acquisition at these inputs. For spectral radiometric BSDFs, the CCD camera is used to capture images at all thirty-five integration times for each of eight filtersets, as shown in Figure 8.1.

The procedures used to extract spectral BSDF data from these images are executed as follows, as is defined according to the dark grey path in Figure 7.1:

•In all 280 images, predefined consistently deviant pixels are eliminated, or set to zero. For details describing the identification of these pixels, see section 7.3.1.

•In all images, pixels with a digital level equal to seven or below are set to zero. A digital level of seven was determined to be the noise to signal threshold, as also described in section 7.3.1.

•If reflection mode is selected, known parasitic light locations from the beam's spheroidal reflection are identified (section 7.3.2).

•For all images, a vignetting correction matrix is then applied for the full image to correct for light drop off toward the edges of the image. The vignetting correction matrix was developed in (Gayeski 2007b), and is briefly reviewed in section 7.3.4

•At this point all of the images' raw data for each filter set has been corrected, and can be combined into 8 HDR images via the spectroradiometric calibration described in (Gayeski 2007b). Each HDR image is associated with three estimations of radiance, one in each of the red, green, and blue channels. Thus the output at this stage is 24 radiance estimations for each pixel.

•For each of the 1380 x 1028 pixels, the spectrum estimation method will be applied (Chapter 6). Vector d is arranged from the aforementioned 24 radiance estimations and matrix N is created from the known spectral properties of the spheroid, the dedolight, the filtersets, and the ASR of the camera. The application of this method results in a reflectance or transmittance spectrum for the sample, ρ_k, at each pixel.

• Each pixel can be correlated to an incident and emerging direction pair, via the spatial calibration derived in (Gayeski 2007b).

• Depending on the angular resolution of the spatial calibration, the discrete spectral reflectance or transmittance, $\rho_{sample,\lambda}(\theta_i,\phi_i,\theta_r,\phi_r)$ or $\tau_{sample,\lambda}(\theta_i,\phi_i,\theta_r,\phi_r)$, can be averaged, element by element, over chosen solid units of angle.

• For each pixel group, the magnitude of the discrete spectral reflectance or transmittance, $\rho_{sample,\lambda}(\theta_i,\phi_i,\theta_r,\phi_r)$ or $\tau_{sample,\lambda}(\theta_i,\phi_i,\theta_r,\phi_r)$, will be corrected to account for concentration and magnification effects of the spheroidal mirror at the position of reflection (θ_i,ϕ_i). These corrections are described in detail in section 7.3.3.

- The resulting $\rho_{sample,\lambda}$ $(\theta_i,\phi_i,\theta_r,\phi_r)$ or $\tau_{sample,\lambda}(\theta_i,\phi_i,\theta_r,\phi_r)$ data is accumulated into a m x n x 114 matrix, with m x n pixel groups, each correlated to a vector $\rho_{sample,\lambda}$ $(\theta_i,\phi_i,\theta_r,\phi_r)$ or $\tau_{sample,\lambda}(\theta_i,\phi_i,\theta_r,\phi_r)$ of length 114, covering the visible spectrum at 5nm increments. This is the first deliverable of the spectral radiometric BSDF calculation.

- For each pixel group, the spectral reflectance or transmittance can then be changed into an RGB triplet. Because a sample's color is influenced by the illumination it receives, the reflectance or transmission alone can not be changed to an RGB triplet. Instead, the sample is assumed to be illuminated by daylight, a standard D65 reference illuminant, replicating noon light. The resulting spectral power distribution is converted to XYZ coordinates (Billmeyer and Saltzman 1981) as shown:

$$X = \frac{1}{P}\int_{\lambda} \bar{x}(\lambda)\ell(\lambda)\rho_{sample}(\theta_i,\phi_i,\theta_r,\phi_r,\lambda)d\lambda \qquad (7.1)$$

$$Y = \frac{1}{P}\int_{\lambda} \bar{y}(\lambda)\ell(\lambda)\rho_{sample}(\theta_i,\phi_i,\theta_r,\phi_r,\lambda)d\lambda \qquad (7.2)$$

$$Z = \frac{1}{P}\int_{\lambda} \bar{z}(\lambda)\ell(\lambda)\rho_{sample}(\theta_i,\phi_i,\theta_r,\phi_r,\lambda)d\lambda \qquad (7.3)$$

$$P = \frac{1}{P}\int_{\lambda} \bar{y}(\lambda)\ell(\lambda)d\lambda \qquad (7.4)$$

where $\bar{x}$, $\bar{y}$, $\bar{z}$ and are the 2° CIE standard observer functions (Smith and Guild 1931), and $\ell(\lambda)$ is

the D65 reference illuminant (CIE 1991).

These *X, Y, Z* tristimulus values are then converted to R, G, B color space based on CIE chromaticities of the reference primaries. The standard RGB color space (sRGB) is used here since it is defined relative to the D65 white point. For sRGB, the matrix C (CIE 1971) changes XYZ values to RGB values and is defined as:

$$C = \begin{bmatrix} 3.24071 & -1.5372 & -0.4986 \\ -0.9689 & 1.87599 & 0.0415 \\ 0.0557 & -0.2040 & 1.05707 \end{bmatrix} \qquad (7.5)$$

Where

$$\begin{bmatrix} R & G & B \end{bmatrix} = \begin{bmatrix} C \end{bmatrix} * \begin{bmatrix} X & Y & Z \end{bmatrix} \qquad (7.6)$$

The resulting RGB values describe the color of reflected or transmitted daylight through the fenestration sample. Each pixel group is associated to a color based on this conversion

- The final spectral radiometric solid, and example of which is depicted in figure 7.2 for a holographic film element, shows the color of reflected or transmitted light for each angle, as well as the angular distribution of radiance. This graphic depicts how a sample spectrally modifies and distributes incident light throughout a space.

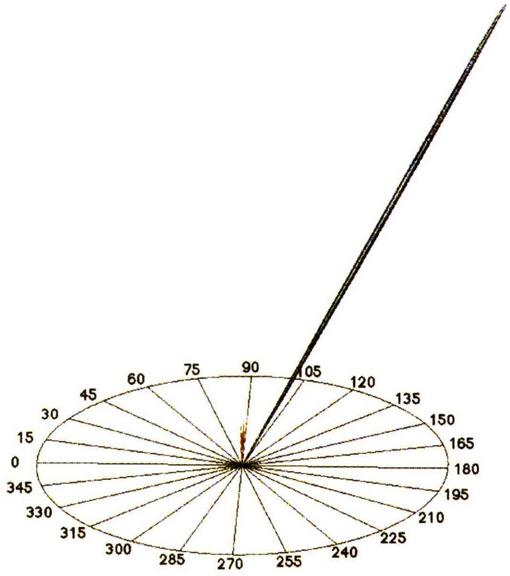

Figure 7.2 radiometric solid for a holographic film element at incident angle (45°, 80°)

7.2 Photometric BSDFs

As mentioned in chapter 5, though the spectral radiometric assessment is much quicker than existing scanning methods, it still requires the CCD camera to capture 280 images. As such it is an involved assessment procedure, as is necessary to achieve valuable detailed spectral information. The Photometric BSDF assessment provides a faster alternative to quickly characterize the angular distribution of radiation in a space.

One deliverable is expected from the photometric BSDF calculation—a 3D photometric solid, graphically demonstrating the luminance distribution of the sample for intuitive, efficient visualization of the results.

As with the spectral radiometric calculation, first the input parameters are selected. The user defines the incident angle (θ_i,ϕ_i), the investigation mode (reflection or transmission), sample diameter D, and data resolution ($\Delta\theta_r,\Delta\phi_r$). Again, the table's motors are arranged to accommodate image acquisition at these inputs. For photometric BSDFs, the CCD camera is used to capture images of the CFS sample at all 35 integration times for only one filterset, that of the $V(\lambda)$ correction filter.

The automation proceeds as follows:

- In each of the 35 images, predefined consistently deviant pixels are eliminated, or set to zero.

- In all images, pixels with a digital level equal to seven or below are set to zero.

- If reflection mode is selected, known parasitic light locations from the beam's spheroidal reflection are identified.

- For all images, a vignetting correction matrix is then applied for the full image to correct for light drop off toward the edges of the image.

These first four steps occur in both radiometric and photometric modes.

- Next, for each pixel in all 35 images, the scaled R,G,B values are added to give a normalized grey value (as described in 5.2.1). For each integration time, a predefined detection and saturation normalized grey level (.06 and .75 respectively) determines which of the pixels in each of the 35 images will be evaluated.

Images with integration times and corresponding normalized grey levels in this range are kept for analysis, while all other images are discarded. Each pixel in the retained images is associated to a luminance by the luminance calibration described in section 7.2.2. The luminance values for each pixel are averaged to achieve an HDR luminance map. The output at this stage is one average luminance value for each pixel.

- Each pixel can then be correlated to an incident and emerging direction pair, via the CCD camera's spatial calibration.

- Depending on the angular resolution of the spatial calibration, the luminance estimations can be averaged over chosen solid units of angle.

- For each pixel group, the magnitude of the luminance will be corrected to account for concentration and magnification effects of the spheroidal mirror at the position of reflection (θ_i,ϕ_i) (section 7.3.3).

- luminance data is accumulated into a m x n matrix, with m x n pixel groups, each correlated to an average luminance estimation $L_{cam}(\theta_i,\phi_i,\theta_r,\phi_r)$.

- $L_{camera}(\theta_i,\phi_i,\Delta\theta_r,\Delta\phi_r)$ is divided by the integral $\int_{\lambda_{photopic}} \rho_{spheroid}(\theta_i,\phi_i,\Delta\theta_r,\Delta\phi_r)d\lambda$ to find $L_{sample}(\theta_i,\phi_i,\Delta\theta_r,\Delta\phi_r)$

- $L_{sample}(\theta_i,\phi_i,\Delta\theta_r,\Delta\phi_r)$ is divided by $E(\theta_i,\phi_i)$

- The final photometric solid shows the angular distribution of luminance throughout a space for a given incident illumination angle. An example of a photometric solid resulting from the BRDF assessment of white paper is shown in figure 7.3.

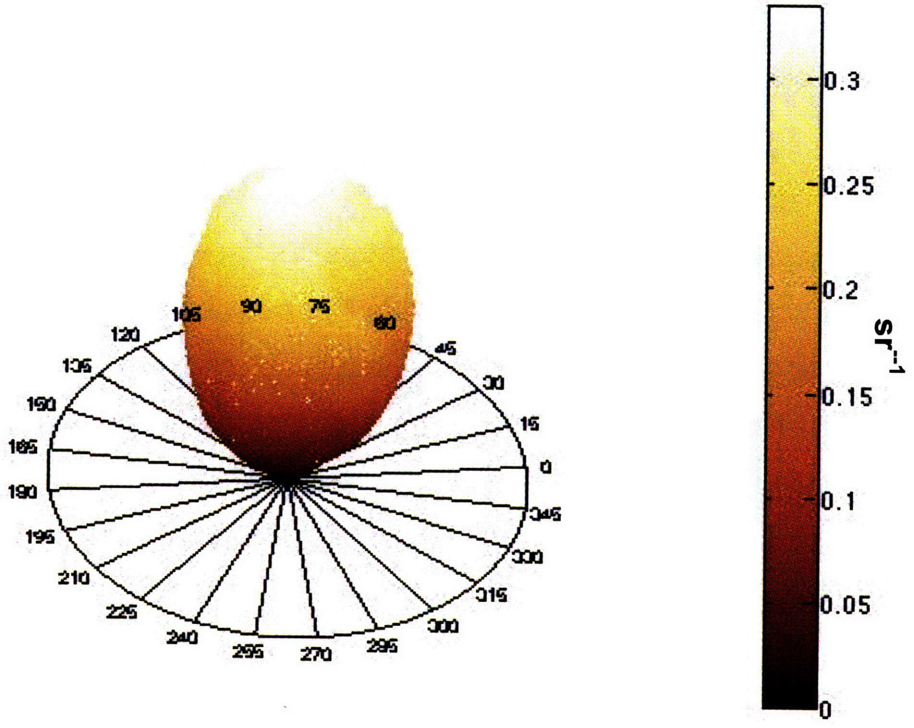

Figure 7.3 Photometric solid of BRDF of white paper at incident angle (0°,90°)

7.3 Corrections

Listed in the automation flow chart, Figure 7.1, several light grey boxes describe corrections made to the raw digital images or the HDR radiance and luminance estimations. These corrections help to minimize the final global error, by identifying and rectifying imperfections in the system that predictably influence the final BSDF assessment.

7.3.1 Noise to Signal Ratio and Deviant Pixels

To determine the noise to signal ratio of the system, an opaque sample was measured and its digital level associated to "blackness" for each incident angle and each integration time. Images were taken with the CCD camera at integration times from 3.95e-5 seconds to 3.7 seconds. Images were taken for incident angles at 60 degree azimuth intervals and 15 degree altitude intervals in transmission mode to determine the camera's noise level.

First, these "black" images were used to identify consistently bad pixels. For all initial beam angles, certain pixels escalated with integration time while most pixels stayed steady, as shown in Figure 7.4. These 159 bad pixels rising above the digital level of 9 were set to zero. Considering that the pixels were reasonably scattered in the image, and that this amount represents around .01%, the loss of these deviant pixels should not affect the Heliodome's performance. However, flat fielding tests could be pursued in the future to allow the instrument to handle slightly off-signaled pixels in a more sophisticated manner.

The maximum digital level observed in the leftover pixels was 9, and the mean value was 6.85. According to the luminance calibration, this maximum black value corresponds to a luminance of 0.2 Cdm^{-2}, a reasonable lower threshold.

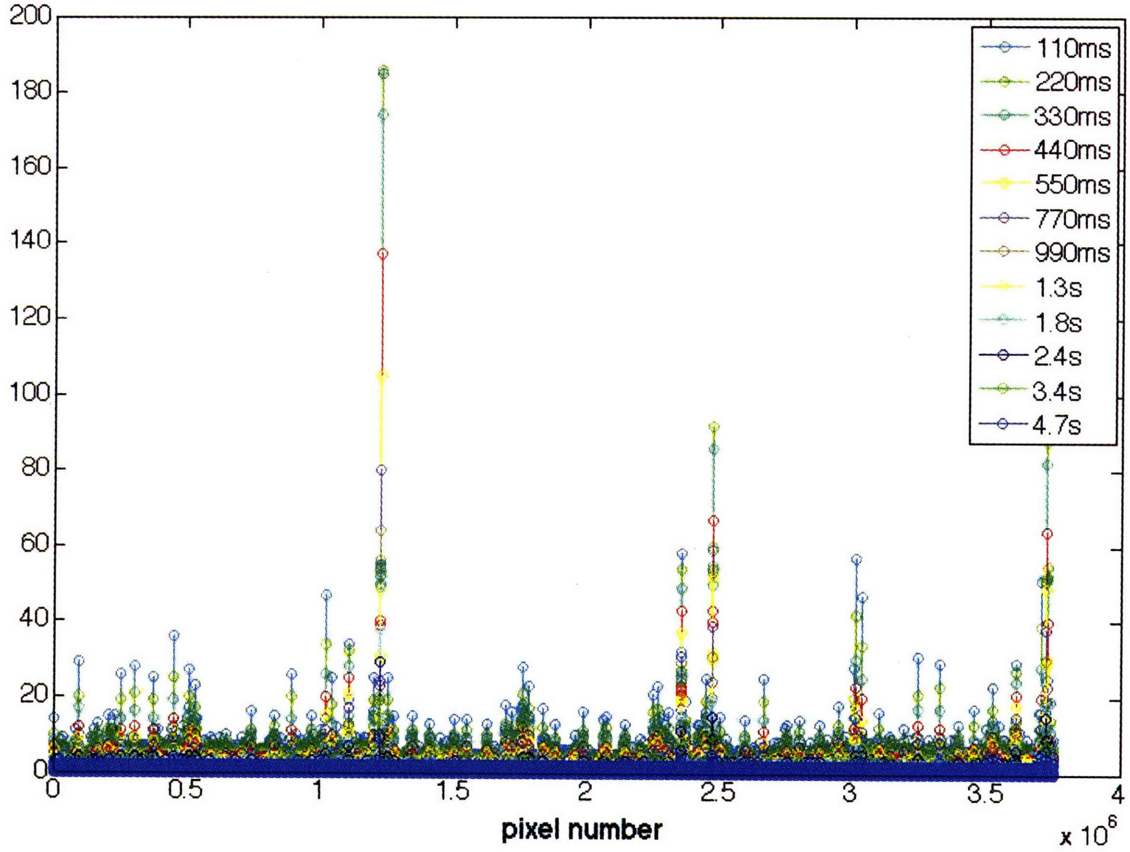

Figure 7.4 Identification of deviant pixels in the CCD camera

The effect of internal reflections in the spheroid was then analyzed in order to ascertain whether it would affect BSDF assessment in the case of highly transmissive or reflective samples. New images of a 5cm diameter hole in transmission were taken at all integration times prior to saturation, and the resulting digital levels were processed. When the actual illuminated area was removed from the image, the mean digital level of the leftover pixels when not corrected for noise was 6.86. This background value corresponds to a luminance of less than 0.2 Cdm^{-2}, found for the level of "blackness." Thus, the effect of inter-reflections could be considered negligible.

Hence, for the radiometric and photometric modes, black digital levels below 9 were set to zero in order to avoid any contribution from noise and internal reflections. The effect is that the Heliodome can not detect luminance values less than 0.2 Cdm^{-2}, however, considering the scale of measurable luminances extends to almost $2e10^5$ Cdm^{-2}, this small undetectable range is not noteworthy. Also, since in reflection a diffusing sample is not even detected until the digital level is around 21 (NDL=0.06), this maximum black value has no effect on BSDF measurements.

7.3.2 Parasitic Light

Parasitic light was observed only in reflection mode. For tests with a hole, two spots appeared in the image, whereas all pixels should not have elevated above black levels. These two spots were caused by the camera's position directly facing the dedolight—the larger spot relating to the beam's profile as it hits the spheroid, and the smaller spot from a reflection of the dedolight source on the curved mirror. In both cases, as the beam is transmitted through the spheroid's surface, a small amount of diffuse scattering occurs, some of which reaches the camera's fisheye lens. Thus, for very high integration times these two spots are visible in the image.

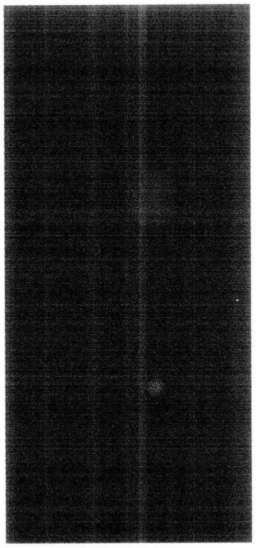

This effect on the image is very regular and easy to identify, as shown in Figure 7.5. However, since these two spots affect different pixels depending on the incident beam and their position can vary with even slight repositioning of the lamp, their effects are very difficult to exclude with accuracy. Because these spots would only have a significant relative effect on the BSDFs of very dark samples, and because the correction at this time would be clumsy, their effect has been disregarded, and will be manually removed where observed.

Figure 7.5 An enlarged image of two parasitic light spots captured by the CCD camera in reflection mode for an integration time of 900ms

7.3.3 Magnification/ Concentration of Spheroid

Due to the spheroid's geometry, reflected radiation can be focused or magnified depending on the incident direction of the beam. Since the beam has a finite radius and is not actually a point, adjacent collimated rays will be reflected such that they intersect and then diverge. The degree to which the spheroid alters the reflected spot "size" depends on the eccentricity, which controls the distance the beam travels from sample to spheroidal reflectance point, and thus also from the intersection point to the camera lens (Snail 1987). The spheroid concentrates the beam's cross section when radiation is reflected into the quadrant of the camera, and magnifies the beam's cross section when radiation is reflected into the same quadrant of the sample.

This magnification (concentration) effect greatly impacts the irradiance levels reaching the camera's fisheye lens for specular beams. Figure 7.6a demonstrates this effect for an incident beam at –60, 0, and 60 degrees zenith angles, along the major axis. As can be easily observed, radiation reflected to the same quadrant as the sample (away from the camera port highlighted with a lighter circle in the figure) results in a magnified spot covering the port, whereas radiation reflected into the camera's quadrant results in a concentrated spot. The resulting irradiance levels reaching the camera's fisheye lens in shown in Figure 7.6b.

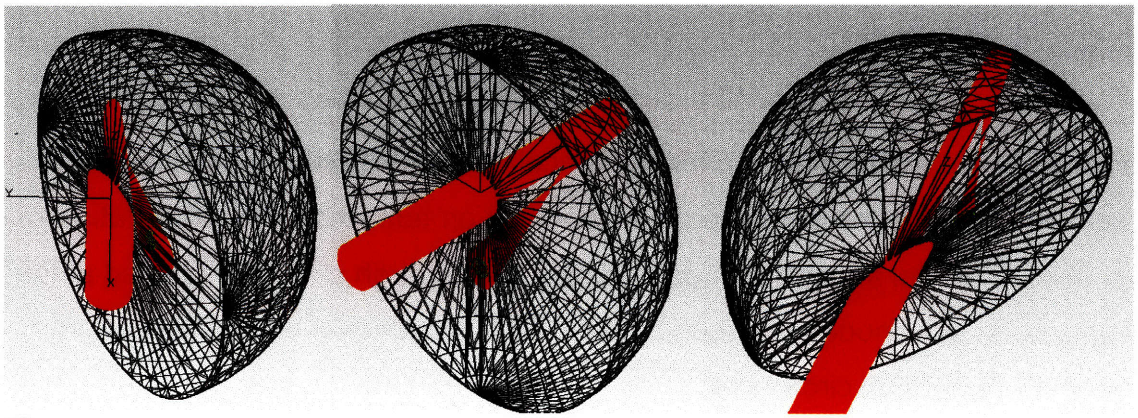

a)

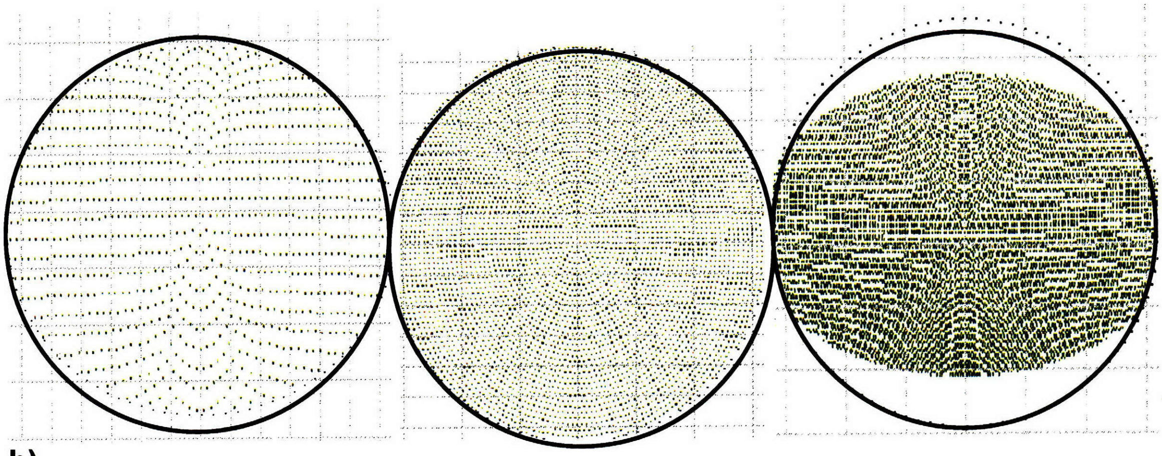

b)

Figure 7.6 a) incident beam at: 60 degrees, 0 degree, -60 degrees respectively—transmitted through 10cm sample hole to be reflected onto the camera port, shown in green
b) Effect of magnification or concentration of beam on camera port irradiance for and incident beam at 60 degrees, 0 degree, and –60 degrees altitude.

The longitudinal (major axis) magnification of a beam is predictable and can be calculated by the following formula (Snail 1987):

$$B_{major} = \left[2\left(\frac{57.5}{s}\right) - 1\right]^2 \qquad (6.7)$$

where 57.5cm is the length of the spheroid's semi-major axis and s is the distance between the sample center and the point of reflection on the spheroid. Because this magnification is only dependent on the distance s, intuitively B_{major} would vary much more dramatically than B_{minor}, since along the minor axis s remains constant.

To simulate the magnification effect of specular beams in the Heliodome, TracePro, a ray-tracing software developed by Lambda Research Corporation, was used to model an incident beam transmitted through a hole positioned at the sample port. The model assumed a hole with 5cm radius at one focal point and a perfectly absorbing circular plane, the size of the camera's fisheye, at the other focal point. The spheroid was modeled with the same dimensions as the actual instrument and with 100% interior reflectance. Since this model was only used to derive a relative effect of the geometry on camera plane irradiance for different incident angles, the actual reflectance of the spheroid was not needed. The incident beam was held stationary in the model, as the spheroid was rotated at 15 degree azimuth increments (from 0 to 360 degrees) and 15 degree altitude increments (from 0 to 75 degrees) and the resulting average irradiance on the camera plane was calculated.

Since each angle simulation assumed the same initial beam, the change in irradiance on the camera plane is solely due to magnification and concentration of the spot size after reflection off of the spheroid. The results of the simulation are shown in Figure 7.7, contained by the minor axis at 180 degrees and the major axis at 0 and 360 degrees.

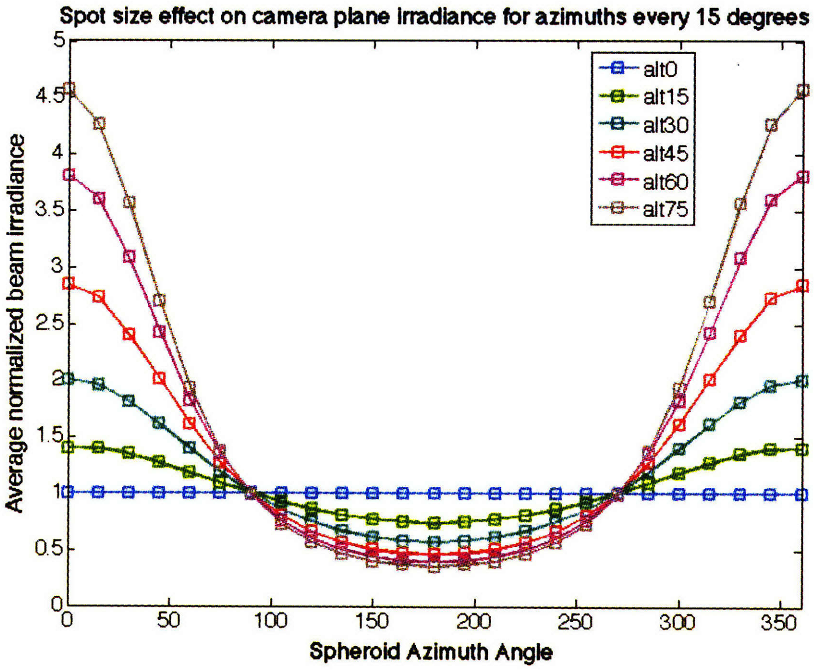

Figure 7.7 The effect of spheroidal optical properties on the average normalized irradiance reaching the camera port for different angles of incidence.

Because this spheroidal effect is consistent, it is correctable. The angles between the measured pairs have been interpolated, and a correction mask, shown in Figure 7.8, has been developed using a reverse spatial calibration. Thus, each correction factor aligns to a pixel associated to the sample emerging angle for which the factor was calculated. This mask will be applied to the high dynamic range images for specular beams to correct for magnification and concentration effects on radiance and luminance estimations before the spatial calibration is applied.

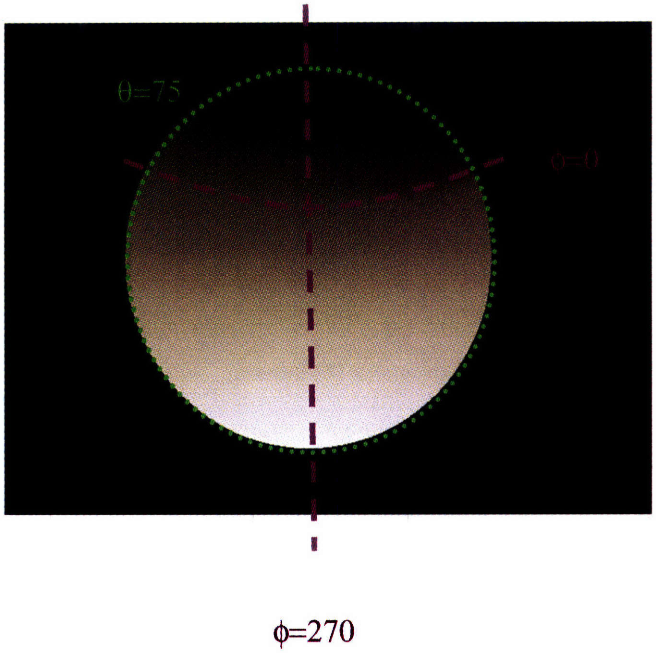

Figure 7.8 Spheroidal magnification and concentration correction mask to correct for incident specular rays that have been focused or dispersed after spheroidal reflection.

However, further work must be completed to determine the actual affect of magnified and concentrated beams on final BSDFs in the Heliodome. Because the camera reads radiance pixel by pixel, the concentration or magnification effects could have a less dramatic impact on estimated radiance levels, depending on the pixel averaging gradient and the number of pixels associated to the emerging angle.

The magnification and concentration effects have been shown to be null for diffuse samples, where the rays are not concentrated or magnified into a larger or smaller spot on the camera port since the sample's emerging radiation is scattered in all directions. This case was tested in TracePro, where a perfectly diffuse sample was placed at one focal point and examined in reflection mode at 0 degrees zenith. The resulting irradiance impinging on the camera port was compared for the same beam transmitting through a hole at 0 degrees zenith, as shown in figure 7.9a.

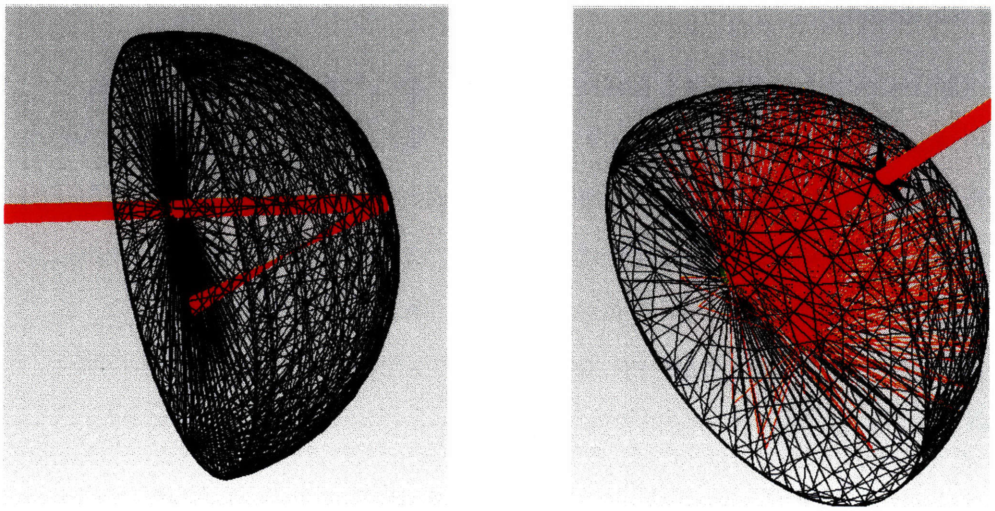

a)

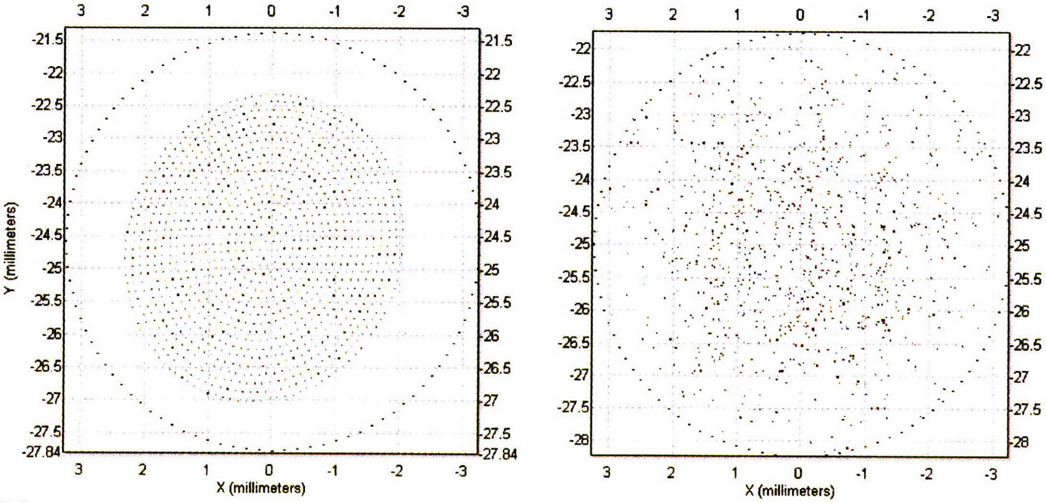

b)

Figure 7.9a) TracePro models of a specular sample and diffuse sample tested in transmission and reflection.

b) The resulting irradiances on the camera port from the two cases.

Figure 7.9b shows the resulting irradiance on the camera port. In the transmitted example, all of these rays would be associated to a few pixels and thus, a small emerging angle. In the reflected case, the rays would be associated to many angles, yielding much lower radiance values over a large area of pixels. However, in both cases, the irradiance on the camera port is the same, and thus no correction matrix is required for diffuse samples.

7.3.4 Image Vignetting

Due to obstructions in the camera's optical system, light fall off occurs at the edges of an image (Inanici 2006), known as image vignetting. Experiments were performed with the CCD camera to characterize this light fall off (Gayeski 2007b). From this characterization, a correction matrix was formed to combat this effect. This correction matrix enables pixel values in each image to be divided by correction coefficients corresponding to each zenith angle of emergence. The result is a corrected raw image, such that radiance and luminance values can be assessed accurately, without vignetting effects.

8. Validation

The Heliodome combines several new elements to bring together an innovative BSDF measurement technique. As such, its validation is vital to the success of the instrument. While several techniques have been used previously in the validation of goniophotometric data, the Heliodome will be validated through the assessment of error at every calibration and processing step, as in (Andersen 2006b, Andersen 2004c). This chapter assesses the errors and uncertainties at each stage in the measurement of spectral radiometric and photometric BSDFs and deduces a final error expected for the instrument. Unlike the imperfections discussed in the previous chapter, the errors accounted for in this chapter can not be corrected.

8.1 Camera Errors

Using the CCD camera as a multi-point radiometer and luminance meter requires several calibrations, each of which implies an error component on the final BSDF data. In the following section, the inaccuracies introduced by the CCD camera calibrations will be calculated, and later used to deduce the final global error.

8.1.1 Error due to spatial calibration

The correlation between pixel locations and incoming zenith camera angles has been determined to within 1.25 percent for the CCD with Fujinon fisheye lens, and 0.5 percent for the NIR camera with Fujinon fisheye lens (Gayeski 2007b). Though the spatial calibration defining the relationship between a sample's emergence angles and the camera's incoming angles has been theoretically calculated to a high degree of accuracy based on ellipsoidal geometry, the spatial calibration errors due to imperfections in the geometry must still be measured.

Now that the final spheroid has been manufactured, this test could be performed by emitting a collimated laser through a hole in the sample plane, at a known incident angle. If the spatial calibration is correct, the beam should be detected on the camera's output image at pre-calculated pixels associated with a certain incoming angle. The extent to which these pixels align with the actual pixels detecting the radiation determines the spatial calibration error. If this calibration were performed for all incident angles, the theoretical spatial calibration could be tweaked so the error was minimized, though never smaller than 1.25%.

As this correction will be performed in the future, the current assumption will be that spatial calibration relating sample emerging angles to camera angles can be modified to not contribute significant additional error to what was already calculated for the theoretical spheroid. Since, by limiting the sample size to 10cm in diameter or larger, the Heliodome ensures that the transmitted or reflected radiation will reach the fisheye camera for almost all incident angles, the spheroid's geometry is close enough to the theoretical geometry to provide a spatial estimation that is reasonably close to the results expected from the corrected spatial calibration for angular samples.

8.1.2 Error due to CCD spectral radiometric calibration

Several factors contribute to the error in CCD spectral radiometric estimation, including:

- Error introduced by inaccuracies in the absolute spectral responsivity calibration (ASR) of the camera,
- Errors introduced in the radiance estimation for each filterband because of the use of filters that cover large 50 to100nm filterbands,
- Errors introduced from inaccurate transformations between quasi-spectral and full spectral estimations.

The first two errors have been assessed in (Gayeski 2007b). In validating the ASR curves, the average error for estimating total radiance of a visible beam with radiation between 380nm and 945nm was found to be 8.9% for the red channel, 4.3% for the green channel, and 5.2% for the blue channel. For the estimation of radiance in each filterband, a wide variety of fenestration materials and unknown spectra were tested, most of which sustained errors below 5% in theoretical tests (Gayeski 2007b). When tested experimentally, most sustained errors below 10%, however this estimation included both the error from the ASR curves and from the method of radiance estimation for each filterband.

But, since these quasi-spectral radiance estimations feed into the spectral estimation method, they are only secondary, and do not directly affect the accuracy of spectral radiometric BSDF assessment. Instead, it is more informative to compare the final spectral estimation results compared to the known reflectance or transmission spectra of a range of fenestration materials. In chapter 6, the error between the estimated spectra and measured spectra for 48 fenestration materials, averaged to 9.4%. Because the ASR calibration curves and filtered quasi-spectral radiance estimates were used to derive the estimated spectra, their respective error contributions should be included in this final average. As a result, 9.4% will be considered the relative expected error from the camera's full spectral estimation method and calibration procedure.

8.1.3 Error due to CCD photometric calibration

In section 5.2.1, $f_1'_{,\text{photopic}}$, the relative error between $V(\lambda)$, the spectral sensitivity of the human eye, and $S(\lambda)$, the modified spectral sensitivity of the camera, was found to be 17.6%. However, this relative error feeds into the photometric calibration, and thus only contributes to the total error of photometric BSDF measurement as a secondary source.

In fact, as was shown in figure 5.4, the relative error between these two sensitivities depends heavily on the spectral modifications of the sample to the incident beam. If the relative spectrum of the modified beam peaked at a point of stark incongruency between $V(\lambda)$ and $S(\lambda)$, the errors between actual luminance and predicted luminance of the beam would be high. Otherwise, the errors would be much lower.

The photometric error, ε, is used to quantify the influence of f_1' on the BSDF assessment (CIE 1987).

$$\varepsilon_{photometric}(\%)=\frac{\left(\sum_{n=1}^{N_\lambda} S(\lambda_n)\cdot\Gamma_{meas}(\lambda_n)\cdot\Delta\lambda_n\right)\cdot\left(\sum_{n=1}^{N_\lambda} V(\lambda_n)\cdot\Gamma_{calib}(\lambda_n)\cdot\Delta\lambda_n\right)}{\left(\sum_{n=1}^{N_\lambda} V(\lambda_n)\cdot\Gamma_{meas}(\lambda_n)\cdot\Delta\lambda_n\right)\cdot\left(\sum_{n=1}^{N_\lambda} S(\lambda_n)\cdot\Gamma_{calib}(\lambda_n)\cdot\Delta\lambda_n\right)} \qquad (8.1)$$

where Γ_{meas} is the spectral radiance of the light source used for BSDF measurement and Γ_{calib} is the spectral radiance of the light source used for photometric calibration. While the HMI dedolight was used for both, for spectral samples Γ_{meas} would have to be weighted by the reflectance or transmittance coefficients of the sample.

Since each spectral sample would be different, making Γ_{meas} different for each test, the contribution of f_1' to photometric BSDFs can only be conclusively quantified for the measurement of neutral samples. In this case, the Γ_{meas} and Γ_{calib} would only maximally differ as much as the HMI fluctuates spectrally within itself. An assessment of the beam's initial qualities (Section 8.2) determined this fluctuation was less than 1%.

For spectral samples, the photometric calibration was shown to accurately predict luminances within 10% for all tested samples. This error band includes any contribution of spectral + photometric error. The average combined error was found to be closer to 4.9% assessed experimentally for spectral samples. Thus, the global error analysis will use this average relative error when calculating the global error for the Heliodome.

8.1.4 Point Spread Function

In order for a CCD camera to be used as a radiometer, radiance must be able to be evaluated on a per pixel basis. It has been shown in the application of land cover characterization that this type of per-pixel analysis can be prone to inaccuracies when substantial portions of the signal for one pixel come from adjacent areas (Huang et al. 2002, Townshend et al. 2000). This means that the real radiance of a pixel would be also be a function of surrounding pixels, which could be characterized experimentally. In other systems, the point spread function (PSF) has been shown to produce as much as a 3.7% difference between two pixel groups with the same illumination (Hong and Voss 2004). Because this effect most often occurs in high contrast scenes, it is necessary to evaluate the PSF for the application of the Heliodome.

Effects of the point-spread function on the radiometric accuracy of a CCD camera can be measured by taking images of a point source (Hong and Voss 2004). The tungsten halogen lamp was used to transmit a collimated beam through a small hole (less than 1mm in diameter) onto the inner surface of the spheroid and reflected onto the camera's fish-eye lens. The resulting spot illuminated only a small pixel area on the image, a cluster of three or four pixels. Images of this spot were taken at various integration times with digital levels averaging between 40 and 220 digital counts in the green channel.

Assuming the PSF was radially symmetric across the sensor, the spot averages were then charted against the averages of surrounding pixels at radii from 1 pixel to 100 pixels away from the center of the spot. The results from the green channel are shown in Figure 8.1 for exposure times between 400ms and 4.7 seconds. The red and blue channels had a similar reaction as the green channel, with digital levels dropping below the noise level for radii>2 pixels.

Because the PSF is so steep, with digital levels dropping dramatically outside of the spot area, the effect on the radiometric accuracy of the system was deemed negligible. Neglecting the PSF might cause errors in the estimation of incident beams filling only the solid angle corresponding to one pixel. However, for the application of the Heliodome, pixels will be averaged for larger solid units of angle. Thus, all the photons, even the ones spread to adjacent pixels, would be included in that average, minimizing the effect on the resulting BSDFs.

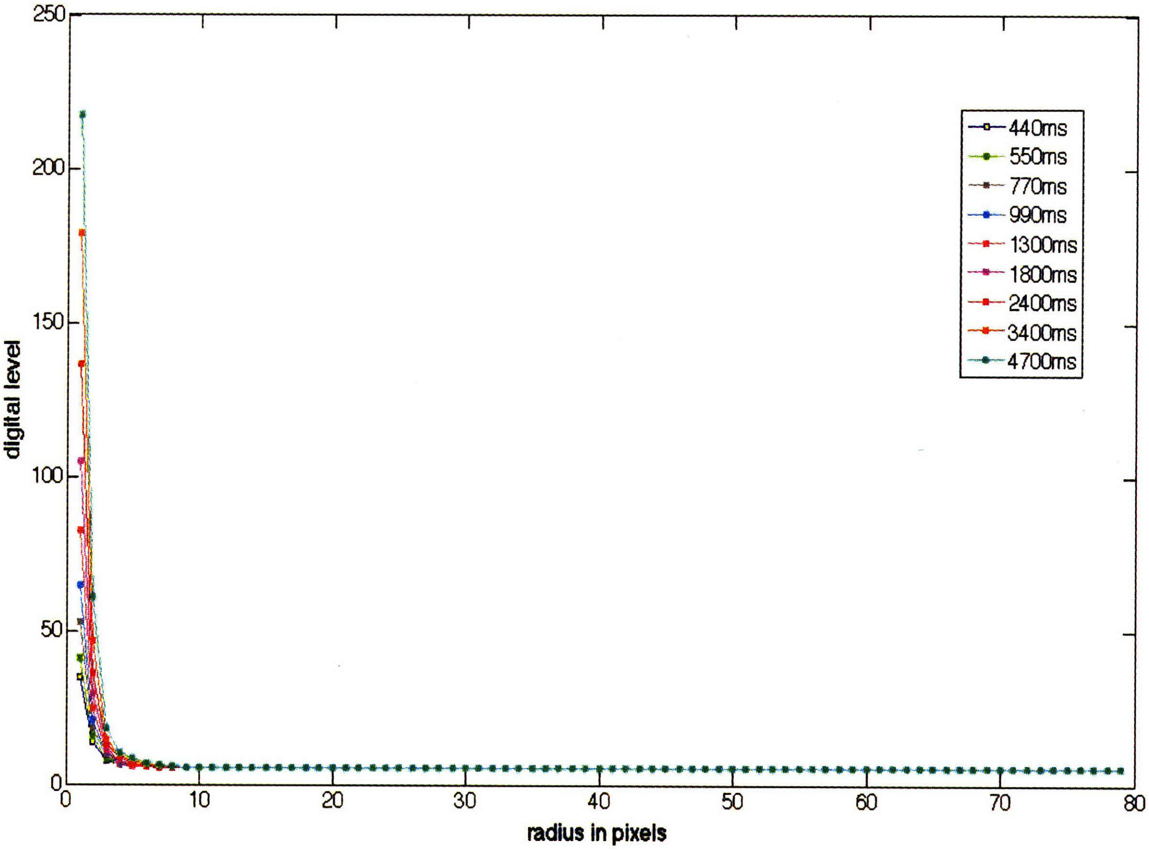

Figure 8.1: CCD camera's green channel response to the point spread function using the tungsten halogen lamp as a point source

8.2 Errors from HMI lamp

For both spectral radiometric and photometric BSDF assessment, an accurate measurement of the incident illuminance on the sample plane is necessary. Because the Heliodome set-up treats the HMI beam as a fixed entity, the illuminance on the sample plane is assumed to be uniform and constant over time. There is also a supposition that the dedolight is a perfectly collimated beam to mimic direct sunlight, while in reality, there is some quantifiable beam spread. All of these imperfections in the beam have been examined so their effect on BSDF can be quantified, as a result of the experimental analysis described in this section.

8.2.1 Sample Illumination Uniformity and Incident Beam Collimation

The collimation of the incident beam strongly affects the resulting BSDFs. An uncollimated source would result in light reflecting off the sample (or transmitting through) at more open angles. When the radiation is reflected back to the second focal point, a larger spot size results. Compared to the expected radiance from a collimated beam with the same initial flux, the camera would read a lower radiance for associated pixels. Obviously, lower radiance estimations will influence the BSDF data, as would the altered light angles hitting the camera's fish-eye.

In order to assess the beam's collimation, experiments were performed with the HMI dedolight to determine the angular beam spread. The first objective was to choose a lamp setting that would be locked in as the default for all fenestration data collection.

The dedolight can be adjusted in three ways—through a variable knob that spans a range between flood lamp and spotlight mode, through adjusting the power level on the power box itself, and by changing the size of the beam with an adjustable light-blocking aperture.

To determine the appropriate lamp settings, the dedolight was set in spotlight mode on the highest power setting in order to achieve a base level of collimation. Then, with the lamp facing the 10cm sample port and centered on the hole, the distance between the lamp and the sample port, *h*, was measured and recorded.

To find the appropriate aperture setting, the aperture size was modified from its smallest setting, resulting in a 10cm diameter beam at the sample plane ($D_{\text{sampleplane}}$), to its largest setting, resulting in a 34cm diameter beam at the sample plane.

For seven intermittent settings in that range, a luxmeter was used at the sample plane to measure the variability in illuminance across the sample port. This illuminance variability was then associated with a beam spread angle, calculated in Equation (8.2):

$$\theta_{beamspread} = tan^{-1}\left(\frac{D_{sampleplane} - D_{lamp}}{2h}\right) \qquad (8.2)$$

The results are shown in Figure 8.2. To choose an appropriate lamp setting, the beam spread angle and illuminance variation over the sample port needed to be minimized. As shown, the most collimated lamp settings also induced variations across the sample port of more than 2000 lux. To achieve an illuminance differential of less than 400 lux across the sample plane for the largest sample diameter, a beam spread angle of 2. 4 degrees was chosen.

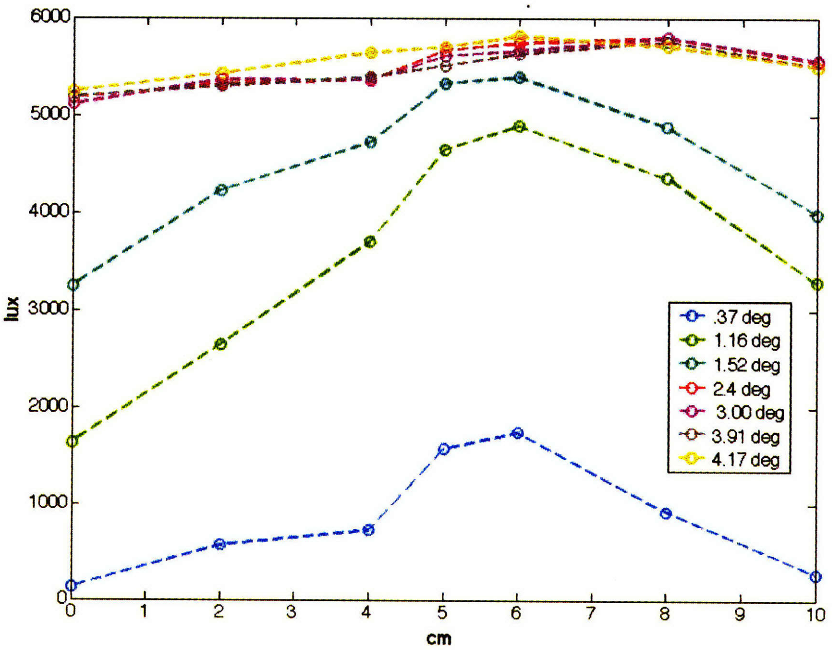

Figure 8.2: HMI beam variation across sample diameter for different beam spread angles

The effect of the beam spread on the resulting illuminance on the camera's fisheye was analyzed using TracePro. The spheroid, lamp, and camera port were modeled, and a uniform angular beam spread of 2.4 degrees with uniform circular spatial distribution of rays was assumed. The rays were traced for azimuths of 0 and 90 degrees with and without the beam spread for a beam with the same total flux, as shown in Figure 8.3. At 15 degree zenith angle increments, the illuminance on the camera port was compared for the two beam conditions.

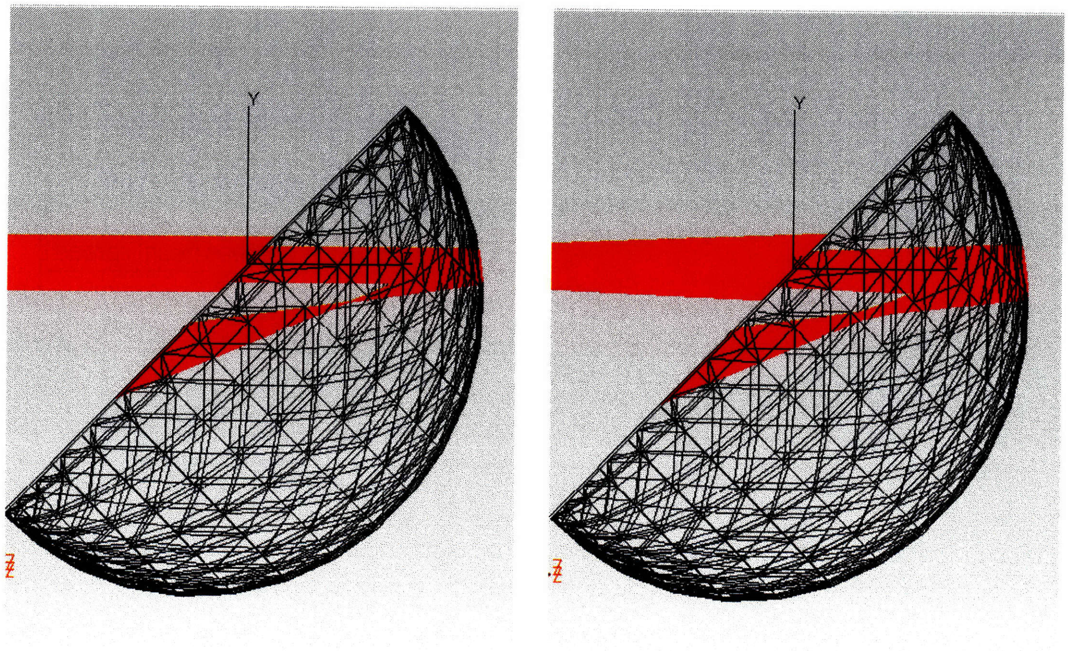

Figure 8.3: TracePro model at 0 degrees azimuth, 45 degrees zenith angle. Simulation with and without 2.4 degree beam spread

Because the spheroid's concentration and magnification potential is at its maximum along the major axis and at its minimum along the minor axis, the errors induced by this simulation should adequately describe the range of spot size divergence introduced by the beam's angular spread. As shown in Figure

8.4, the difference in irradiance or illuminance on the camera plane caused by the beam spread is small and not consistently an over or under estimate.

The maximum difference occurs at the extreme angle, 75 degrees, when the distance between the point of reflection on the spheroid to the camera port is the farthest. The spot size is magnified because of this greater distance traveled, and irradiance levels are at their lowest. Thus, the relative error introduced by rays hitting the camera plane or missing the camera plane due to their added angularity, is, at its highest, a 5% relative difference. Overall, the difference between beam spread irradiance and collimated beam irradiance was much lower, with an average magnitude of 1.34% for the major axis, and 1.32% for the minor axis.

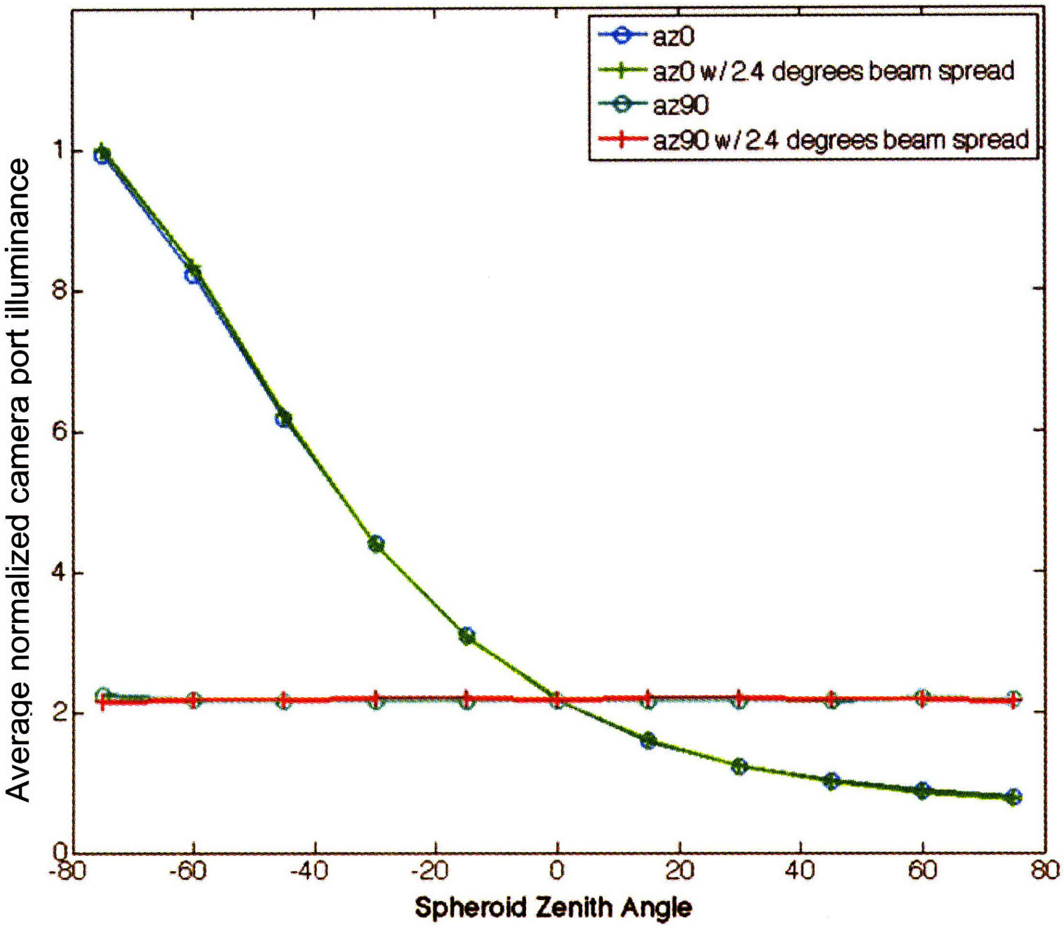

Figure 8.4: Beam spread effect on camera plane irradiance for reflection along spheroid's major and minor axis

Due to the mirror's complex conical reflectance properties, the effects of beam spread on the illuminance or irradiance at the camera port for a beam is not easily predictable. After reflection off the spheroid, the beam spread angle could cause rays to be exported out of the camera's fisheye area -- as was the case for twenty-eight rays in Figure 8.5. However, the beam spread can also redirect rays that would have been excluded from the camera plane post-reflection back closer to their original trajectory. Because of this phenomenon, this error cannot be corrected.

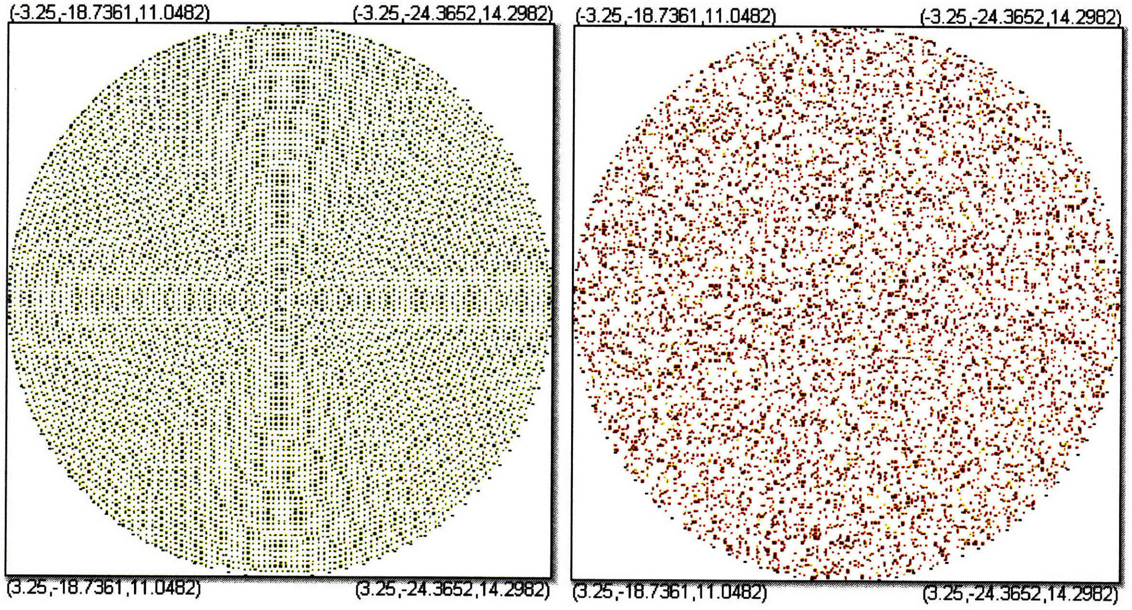

Figure 8.5: Ray-tracing of camera port for incident zenith an angle of 60 degrees. a) without beam spread: 8306 rays b) with beam spread: 8278 rays

8.2.2 HMI Illumination Uniformity over time

The HMI dedolight was also tested for constancy over time. The assumption of a fixed beam with one spectral exitance (M_{HMI}) measurement for each BSDF assessment supposes that the beam will not change in illuminance or spectral power distribution over the time it takes for a full assessment.

This supposition was first tested by monitoring the HMI lamp's changing illuminance levels from ignition to stabilization over the period of an hour. The illuminance levels were measured with a luxmeter held in a stable position perpendicular to the lamp's beam. The results are shown in Figure 8.6, showing lamp output stabilization occurring around 5-7 minutes after ignition.

Between the two tests, there was a relative difference between the two stabilization points of less than 2%. In each test, fluctuations in illuminance level after reaching stabilization were small, achieving less than a 1% difference between the lowest and highest illuminance level measured after minute seven.

This difference was verified through five additional trials, in which the lamp was ignited once, and the illuminance levels across the beam spot were measured every 20 minutes after stabilization. The average difference between each trial for each measurement point was 25 lux, a relative difference of 0.3%. These measurements assure a consistent illuminance level for each assessment period, and even suggest that a stabilized M_{HMI} might only need to be measured once, instead of for each assessment trial.

However, over several months, the lamp has been observed to be less stable spectrally, as shown in Figure 8.7. The four plots show the HMI spectral relative irradiance distributions, measured over the span of a year. Three of the four plots have been "smoothed" by averaging measurements over a 1nm boxcar width. Dramatic changing peaks and even slight shifts in the HMI's spectrum will significantly affect the radiance estimations and spectral estimation results. Thus, it is necessary to measure the HMI's filtered spectral exitance before each assessment period in order to achieve reliable sBSDF results.

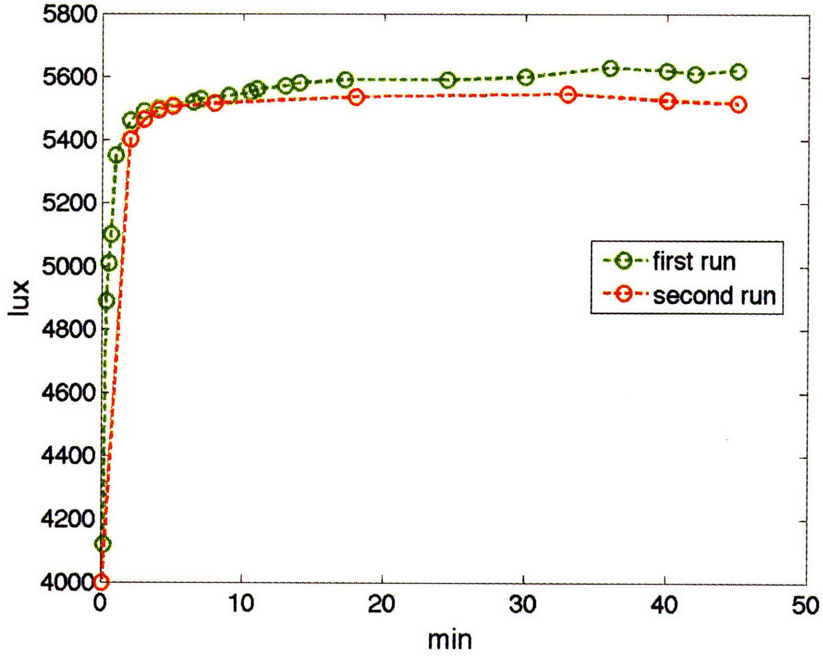

Figure 8.6 HMI Beam fluctuations for ignition and reignition

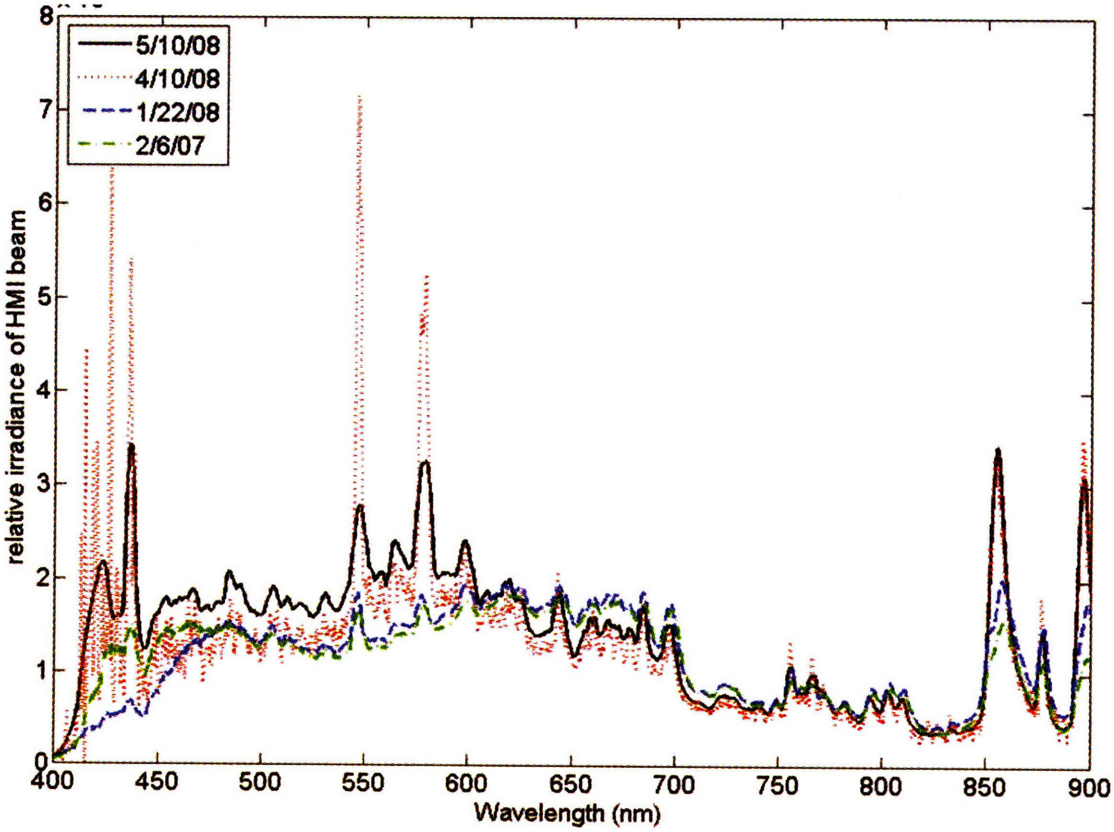

Figure 8.7 HMI lamp spectral relative irradiance changes over time

In summary, the errors contributed by the HMI lamp are as follows:

- The incident beam spread of the Heliodome was determined to be 2.4 degrees, the result of a compromise achieving a more uniform illuminance over the large sample plane. This beam spread resulted in a relative illuminance difference of 1.3% (8.2.1).

- The illuminance uniformity test measured an 8% relative variation across the sample area for the chosen 2.4 degree beam spread as described in section 8.2.2.

- The HMI also varied in illuminance over several trials of the same warm-up time. The beam showed a relative variation of 1.8% between trials at its maximum illuminance level. Spectrally, the HMI beam showed a less than 1% relative difference over the assessment period (8.2.3).

8.3 Spheroidal interception

Error is also introduced to the final BSDFs by the spheroid's transportation of radiation from the sample to the camera's fish-eye lens. While the spheroid's magnification effects, blind angles, and coating non-uniformities are addressed in the automation process, neither its specular properties nor its variance in spectral transmission or reflectance has been taken into account.

8.3.1 Polarization

Due to the mirrored qualities of the spheroid coating, it is expected that that the incident beam could be mildly polarized after reflecting off of the spheroid. The polarization of the beam could affect the radiance predicted by the camera if either:

1. the camera is more or less sensitive to different angles of polarized light.
2. the polarization of the beam causes less light to reach the camera than if it were unpolarized.

To measure the degree to which the camera is sensitive to polarized light, images were taken of a reflectance standard illuminated with a tungsten halogen lamp passing through a 500nm narrow passband filter, as shown in an image captured by the CCD camera in Figure 8.8. After reflecting off the standard, the beam was projected through one Ocean Optics mounted linear glass polarizing lens, which was rotated to polarize the reflected filtered radiation at 15 degree angle increments for each image.

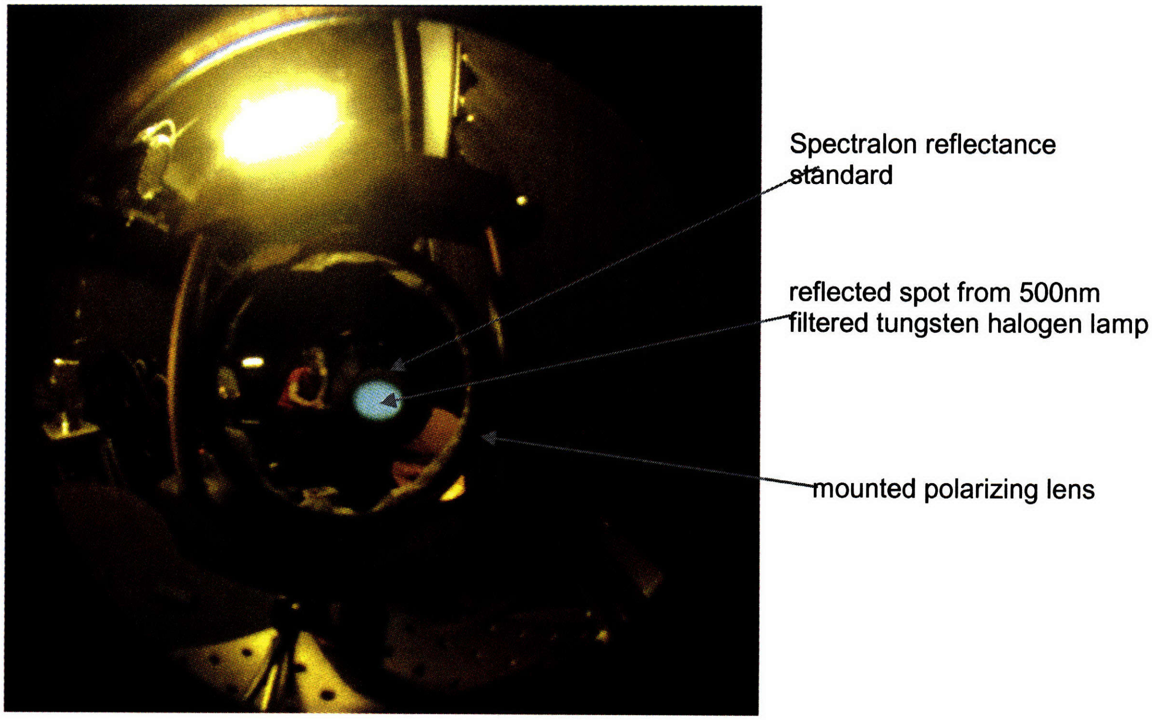

Figure 8.8 View of illuminated reflectance standard and polarizing lenses from the CCD camera, depicting the experimental set-up to determine the CCD camera's sensitivity to polarization

The reflectance standard was used to guarantee that the initial beam was unpolarized before passing through the polarizer, so as not to preferentially efface any polarized radiation from the initial beam. Figure 8.9 shows the average normalized digital level for the green channel at different angles of polarization for various integration times of the camera. Because there is little change in the perception of the camera for different angles of polarized light, the camera can be considered insensitive to polarization. Thus, any error introduced by polarization would be caused by an actual reduction in the amount of light reaching the camera, due to the spheroid's polarizing surface properties.

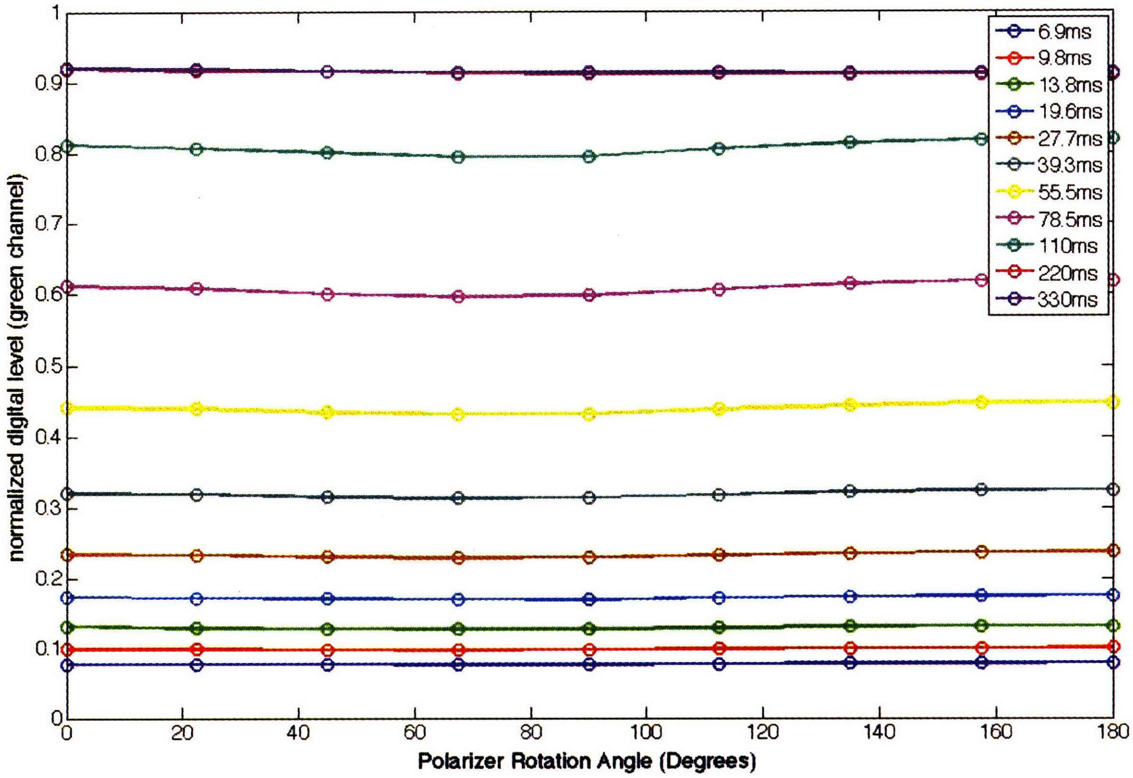

Figure 8.9 CCD camera sensitivity to polarization for different integration times

In order to measure the degree to which the second effect occurs, an experiment was conducted using a Labsphere integrating sphere calibrated to measure total radiant flux for monochromatic beams from 375 to 1100nm at 25 nm increments. The beam from a tungsten-halogen lamp with a 500nm narrow passband filter was projected through a mounted linear glass polarizing filter into the integrating sphere's port, as illustrated in Figure 8.10a. The polarizer was then rotated at 15 degree increments to give a baseline comparison before reflection off the spheroid. This experiment was also repeated for a diffuse initial beam using one layer of translucent white window shading material applied at the beam's exit port.

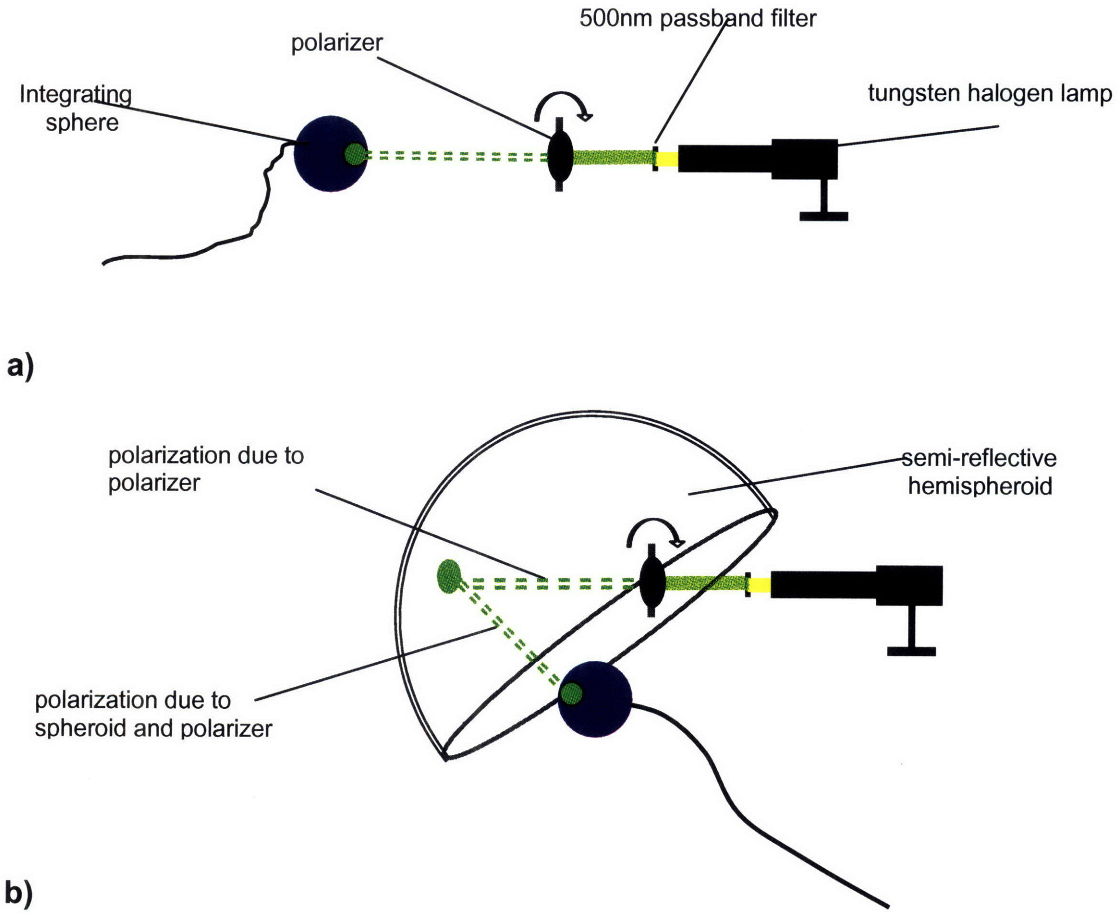

**Figure 8.10 a) baseline measurement for polarized radiation
b) effect of hemispheroid on polarization of reflected radiation**

The baseline for varying angles of polarization was then compared to the flux measured after reflection off the spheroid for the same angles of polarization, shown in Figure 8.10b. Even with a diffuser, the initial beam was polarized. Thus, in order to isolate the additional polarization caused by the spheroid, comparable magnitudes of the pre- and post-spheroidal fluxes for each polarization angle had to be compared, as in Figure 8.11, discounting any reduction in flux caused solely by spheroidal reflectance. A reflectance coefficient for the spheroid was derived by choosing the polarizer angle that yielded the minimum quotient of the post-spheroidal reflectance flux over the corresponding initial beam flux. For the experiment with a diffuse beam, the spheroid's reflection coefficient was 0.64, and for the polarized beam, 0.69.

The scaled initial flux measurements were compared with the post-reflectance flux measurements to isolate the spheroid's contribution to polarization. As shown in Figure 8.11 and Figure 8.12, at a polarizer angle of 160 degrees, the effect of polarization caused by the spheroid is at its peak. In both the diffuse and polarized beam case, the additional polarization effect attributable to the spheroid was 2.1%. This error will be accounted for in the final total error of the Heliodome, as the spheroid's polarization effect could cause the radiant flux of an unpolarized source to be slightly lessened after reflection.

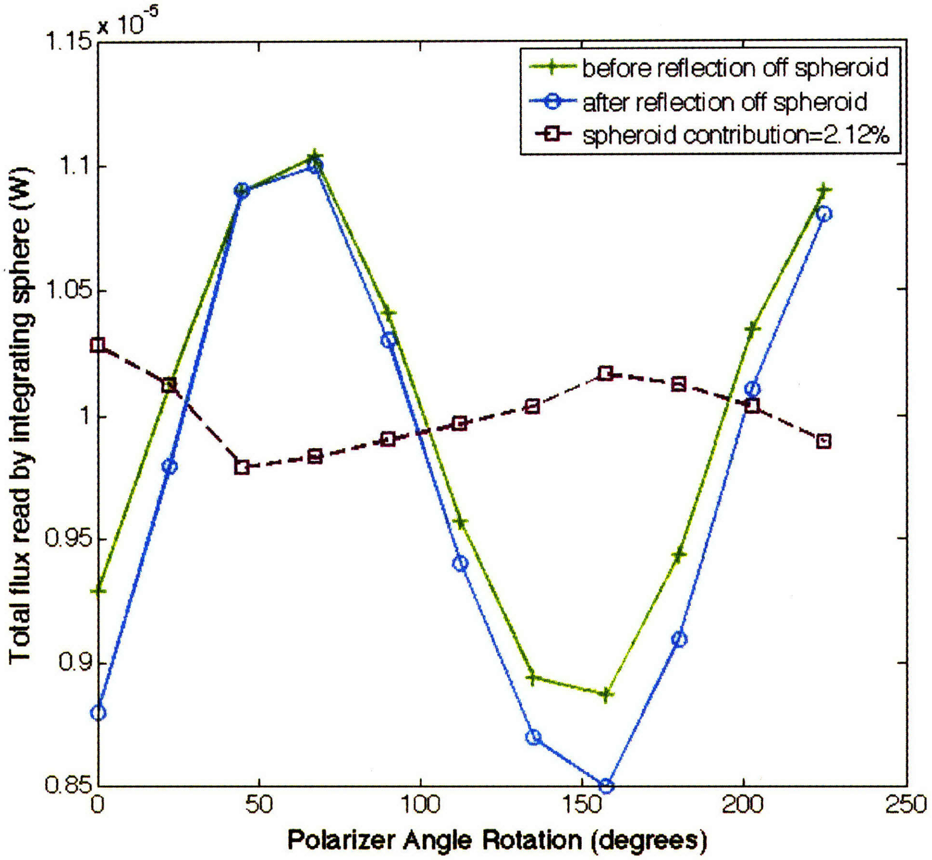

Figure 8.11: Integrating sphere's response to different angles of polarization before and after reflection off the spheroid for a polarized beam

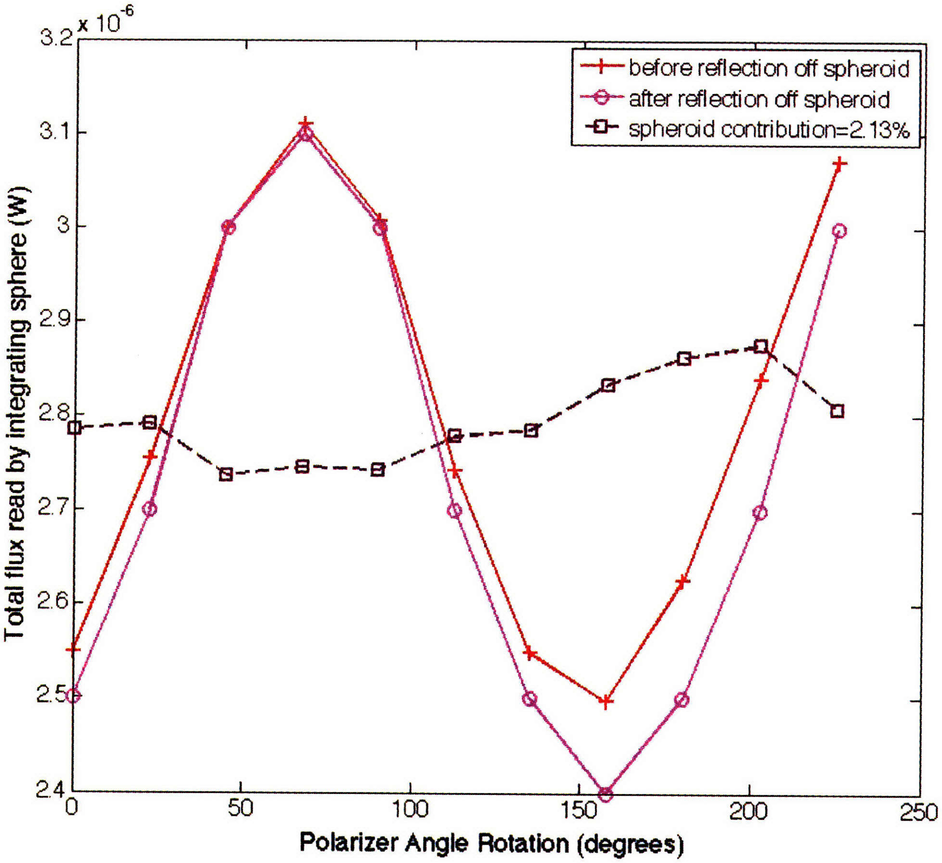

Figure 8.12: Integrating sphere's response to different angles of polarization before and after reflection off the spheroid for a diffuse beam

8.3.2 Reflectance and Transmission Interpolation

The errors from measurements of the spectral properties of the hemispheroid have also been measured. Because the table's positioning system is not yet complete, the spheroid's characterization process was simplified. Spectral measurements were collected along three axes-- the major axis, the minor axis, and along the 60 degree altitude--and trends were interpolated over the surface of the spheroid.

The major assumption that would introduce error in this assessment is that the spheroid has consistent transmission and reflection along any zenith cross-section. In actuality, the spectral measurements along the measured 60 degree altitude varied by 5.1% maximally, and by an average of .7%.

8.4 Total relative error for BSDF measurement

A summary of the sources of significant error contribution is displayed in Table 8.1.

Error source	Relative Error	Affected parameter
Photometric +Spectral Calibration	4.9%	L_{camera}
Spectral Radiometric Calibration	9.4%	$L_{e,camera}$
Spatial Calibration	1.25%	$L_{e,camera}$, L_{camera}
Point Spread Function	negl.	$L_{e,camera}$, L_{camera}
Beam Spread	1.3%	$L_{e,camera}$, L_{camera}
Beam non-uniformity	8%	$E_{e,sample}$, E_{sample}
HMI variance among trials	1.8%	$E_{e,sample}$, E_{sample}
Spheroidal polarization	2.1%	$L_{e,camera}$, L_{camera}
Spheroidal spectral characterization	.7%	$L_{e,camera}$, L_{camera}

Table 8.1 Sources of error contribution in BSDF measurement

The global relative error is calculated in Equation (8.3) where f_i refers to the different individually affected parameters, and N_f refers to their number.

$$\varepsilon_{BT(R)DF} = \frac{\Delta BT(R)DF}{BT(R)DF} = \sqrt{\sum_{N_f}\left(\frac{\Delta f_i}{f_i}\right)^2} \qquad (8.3)$$

This calculation was performed separately for photometric and spectral radiometric BSDF, as shown in Equation (8.4) and (8.5).

$$\varepsilon_{srBT(R)DF} = \frac{\Delta srBT(R)DF}{srBT(R)DF} \qquad (8.4)$$

$$\varepsilon_{pBT(R)DF} = \frac{\Delta pBT(R)DF}{pBT(R)DF} \qquad (8.5)$$

From Table 8.1, the global relative error for photometric BSDFs and spectral radiometric BSDFs was determined to be:

$\varepsilon_{srBT(R)DF} = 12.8\%$ $\varepsilon_{pBT(R)DF} = 9.9\%$

8.5 Results of Automation

As a validation of this automation procedure, two samples were characterized in the Heliodome, one in photometric mode and one in radiometric mode. The results of both tests are displayed and explained in the following section.

8.5.1 Photometric BSDF

For the photometric verification, five layers of diffuse typing paper were compiled and inserted into the sample port to be analyzed in reflection mode. The sample was chosen for its predictable angular properties, so that measured BSDFs could be compared to theoretical expectations for such a sample. Since the sample is less interesting spectrally, it is a good example of a situation that might be conducive to photometric BSDF (pBSDF) testing.

Following pBSDF protocol, the HMI was first transmitted through the V(λ) filter and reflection mode corset, and was measured for initial illuminance with a luxmeter at 2814 lux. The table was adjusted such that the incident beam impinged on the sample at chosen incident angle (0°, 90°). The pBSDF analysis requires the input of transmission or reflection mode and incident angle in order to account for the effect of the spheroid's transmittance on the incident beam before reaching the sample plane.

Images were taken at 38 integration times ranging from 10 microseconds to 3.4 seconds. A range of these images are shown in Figure 8.13, tinted green because of the V(λ) filter. Because the tested sample was diffuse, the lowest integration time detecting radiation was 7.1 milliseconds, much higher than for specular samples. The images are named after their integration time in milliseconds in order to easily identify them during calculation, and are corrected for vignetting effects and deviant pixels.

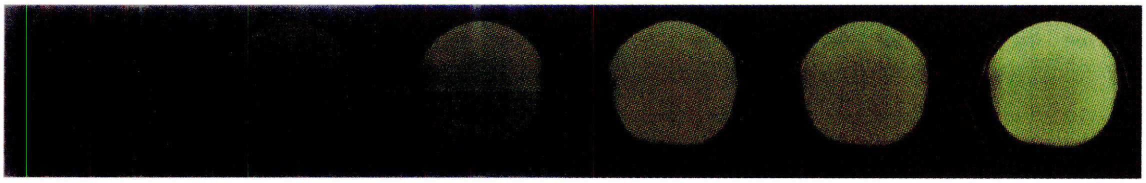

Figure 8.13 CCD camera images taken of a diffusing paper sample at integration times of 7.1ms, 14.2ms, 20.1ms, 56.9ms, and 110ms.

Using the photometric calibration to associate a luminance to each pixel, corresponding pixels from each image in the series are averaged for digital levels from detection to saturation. A high dynamic range image results, corresponding each pixel, and thus each emerging angle, to a luminance level. An example of this HDR image, normalized to the highest luminance level, is shown in Figure 8.14. The two bright spots in the center of the image are the parasitic light spots seen in reflectance mode, as described in chapter 7. Imperfections in the spheroidal geometry can also be observed, as dark spots near the edge of the image denote high altitude angles where the spheroid misdirects radiation. However, overall the image's uniformity demonstrates that the camera is detecting radiation that has been dispersed in all directions, as would be expected for a diffusing sample.

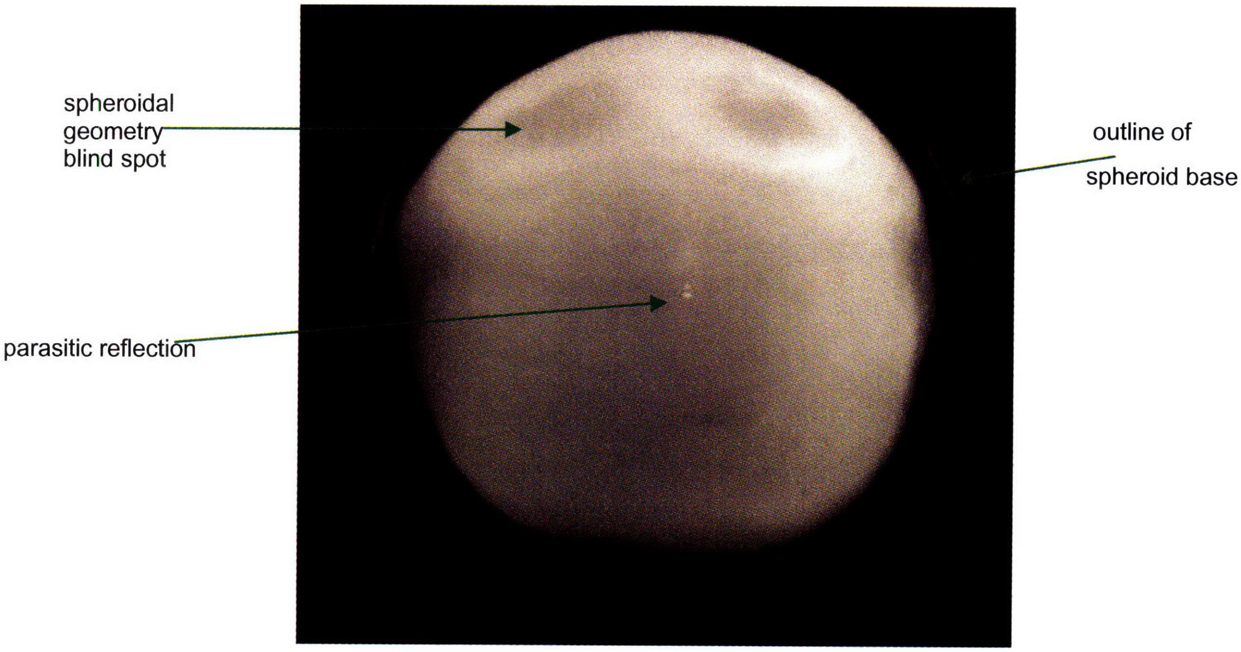

Figure 8.14 High Dynamic Range image showing luminance variance

Finally, the spatial calibration is applied, and the luminance values are divided by the spheroidal reflectance coefficients describing variances in the spheroid's coating for associated emerging angles. These luminances are then divided by the initial illuminance (scaled by $\cos\theta_{i,}$ in this case 1) to achieve a photometric BRDF.

As an end product, the photometric mode delivers a photometric solid (Ashdown 2000, Andersen 2002), an intuitive visualization tool commonly used in its two-dimensional form for the characterization of luminaries. In the photometric solid, the BSDF values are given as radial distances on a polar grid, positioned by their corresponding emerging angles ($\theta_{r,}\phi_r$). The photometric solids are rendered in one color or as a greyscale, with lighter shades indicating higher pBSDF values.

Four photometric solids of the tested diffuse sample are shown in Figure 8.15, at different view angles. The color scale, depicted in shades of yellow, is proportional to the BSDF range. Lighter shades portray greater radial distances from the origin for each emerging angle, exposing the directions in which the sample is most reflective. Because the paper sample is diffusing, it is expected to be similarly reflective in all emerging angles, creating a bulb-like photometric solid. Indeed, these solids verify the success of the photometric BSDF calculation in their conformity to the expected results. Additionally, the paper sample, being symmetric, would be theoretically expected to have a symmetric BSDF about the axis perpendicular to the sample plane. The photometric solid is also successful in this regard.

However, the asymmetry of the top view of the photometric solid clearly shows the limitations of the spheroid's geometry, as the edges bulge at azimuths where the spheroid is accurate for the highest altitude angles, and wane where the spheroid misdirects radiation for lower altitudes. As would be expected, for azimuths from 0 to 180, higher altitudes are visible since the sample is positioned farthest from this portion of the spheroid. Thus, in sample coordinates, the same altitude angle hits higher on the spheroidal surface for azimuths from 0 to 180 degrees, than it does for azimuths from 180 to 360 degrees. Since the spheroid becomes less accurate towards the base, higher spheroidal reflectance yields a greater probability that the rays will be redirected to the camera port.

However, this effect does not critically affect the results of the hemispheroid. It only limits the BSDF analysis to altitude angles from 0 to 75 degrees, which are the most interesting angles for fenestration transmission and reflection anyway. More important are the spheroidal imperfections that influence angles within the 0 to 75 degree range, such as the two indentations at ϕ_r=135 ° and 45 °.

Now that the spheroid is completed, these imperfections can be corrected and the spheroid can be characterized more continuously using the camera. By using a 10 cm diameter reflectance standard in the sample position, the Heliodome can be run in reflection mode to map a correction matrix that would account for smaller geometrical imperfections or coating abnormalities producing uneven digital levels in the image. Once this correction is applied, the photometric BSDFs will be in a usable state. In total, the imaging portion of the pBSDF assessment took 20 minutes and the computational portion of the pBSDF assessment took around 90 seconds. The imaging time, however, should be improved once the method is fully automated.

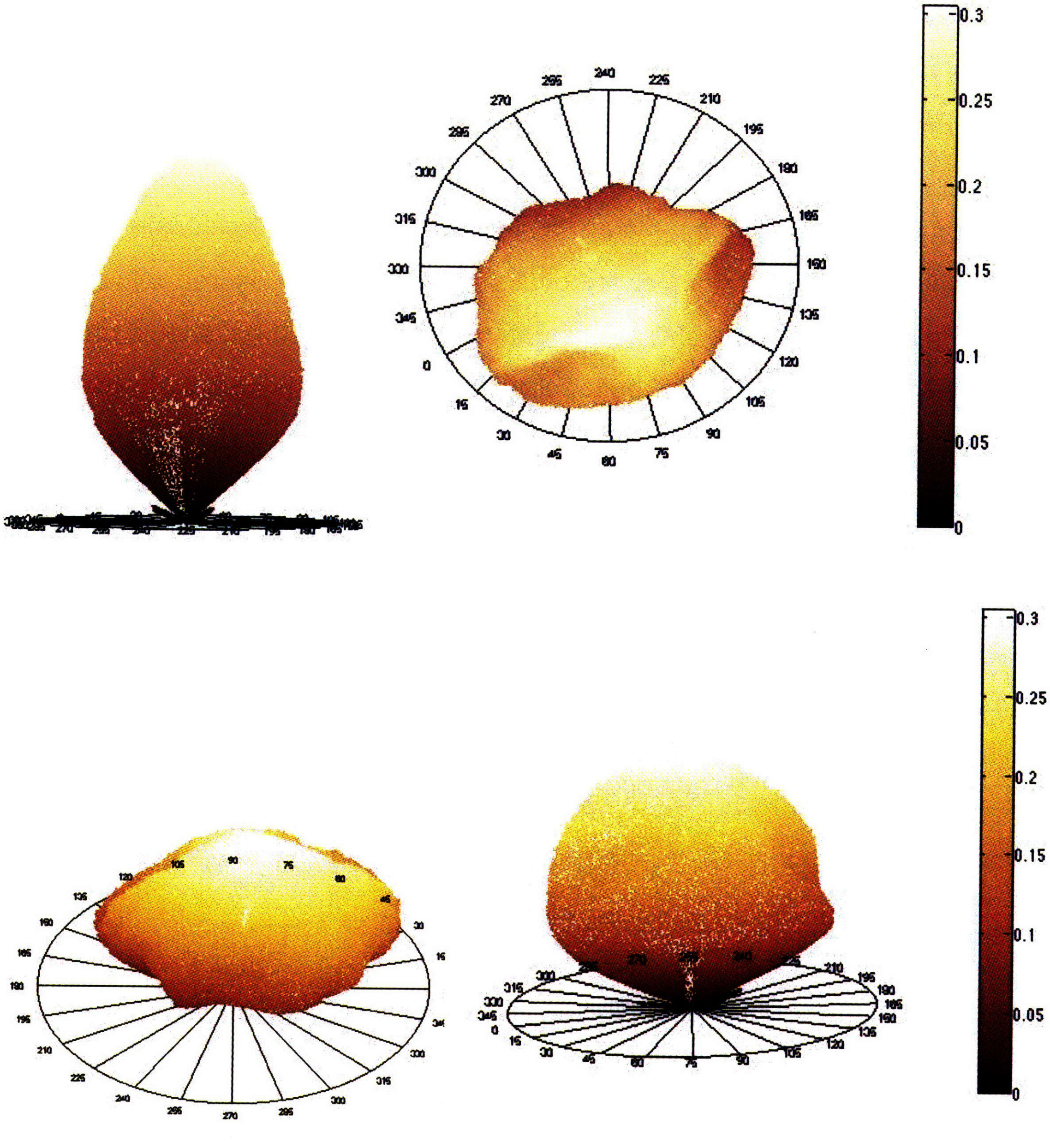

Figure 8.15 Four views of a photometric solid of the pBRDF of diffuse white paper.

8.5.2 Spectral BSDF results

In addition to photometric BSDFs, the Heliodome's ability to measure spectral BSDFs was tested using a holographic optical element (HOE) in transmission mode. Because HOEs dramatically modify incident light both angularly and spectrally, they make good test materials for the Heliodome's spectral BSDF assessment.

In spectral BSDF assessment, the HMI is transmitted through each of the eight filter combinations, and the absolute spectral irradiance is measured with an Ocean Optics USB2000 visible spectrometer. This measurement should happen at the beginning of each assessment period to assure the spectral stability of the HMI source.

Because of the intensity of the lamp, it was impossible to measure the absolute spectral irradiance at the table plane without saturating the spectrometer. Instead, the spectrometer was used to measure the relative spectral irradiance of filtered beam. These relative spectral irradiances were converted to total illuminance measurements, and compared with luxmeter measurements at the table plane. The luxmeter measurements were used to scale the spectral irradiance to ensure correct initial spectral absolute irradiance measurements for each filtered beam.

The table was adjusted such that the incident beam impinged on the sample at a chosen incident angle, in this case (45°, 180°). The spectral BSDF analysis (sBSDF) requires the input of transmission or reflection mode and incident angle, though the spheroid's transmittance was not a factor given the sample was assessed in reflection mode.

Images were taken at 38 integration times ranging from 10 microseconds to 3.4 seconds for each of the eight filter pairs. An example of a 40.8ms image for each filterband is displayed in Figure 8.16, along with the unfiltered transmitted beam for comparison.

As shown, the specular portion of the beam, imaged as the bright spot at the head of the spectral tail, is transmitted directly through the HOE and not significantly modified spectrally or directionally. The HOE image also shows a spectral tail, corresponding to the portion of transmitted radiation that is simultaneously spectrally modified and scattered forward in a narrow range of emerging angles. This tail appears different in each of the filtered images, as only the spectral portion of the tail corresponding to each filterband is imaged.

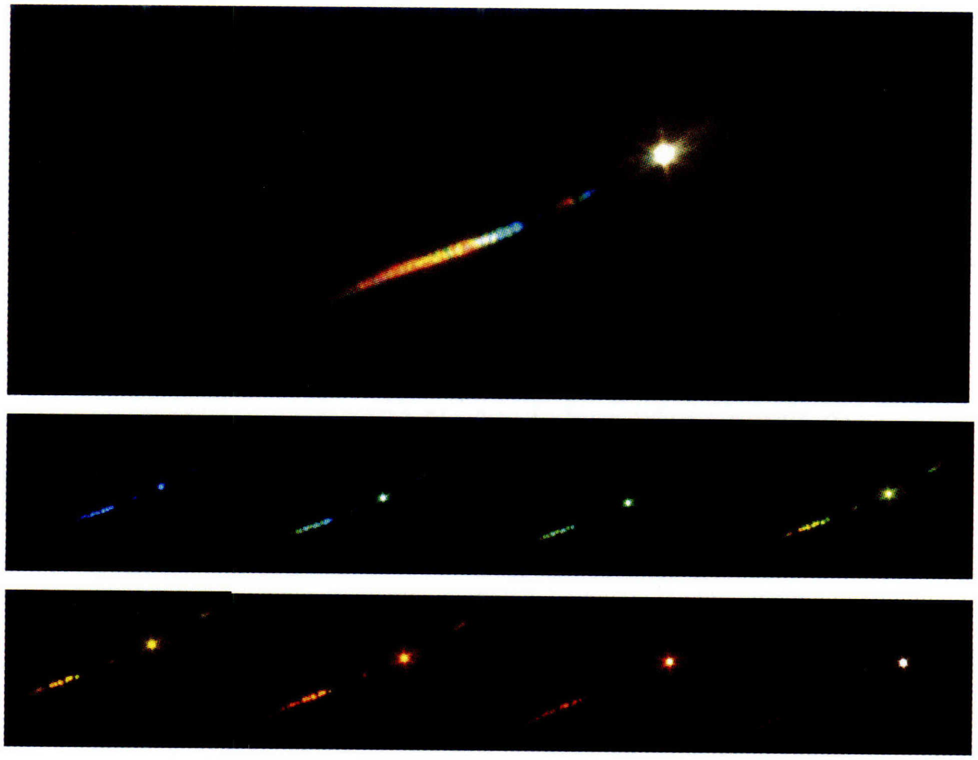

Figure 8.16 (from top left to bottom right) HOE transmission image at 40.8ms for: unfiltered beam, filter 1 (380-500nm) , filter 2 (450-590nm) , filter 3 (480-590nm), filter 4 (500-650nm) , filter 5 (550-640nm), filter 6 (570-690nm) ,filter 7 (650-850nm), filter 8 (800-945nm)

Corresponding pixels from each image in each filtered series were converted to radiances for digital levels from detection (NDL=0.2) to saturation (NDL=0.8).

The radiance estimations associated to each pixel were averaged to create eight HDR radiance maps, describing the emerging radiation through the sample.

The eight HDR images were used to create a digital response vector d (described in chapter 6) for each pixel. Using Interactive Supercomputing Corporation's Star-P parallel computing platform, the spectrum estimation method was applied to any pixel with detectable radiance levels, returning the sample's transmittance or reflectance spectrum for all meaningful emerging angles. Using 12 simultaneous processors, this calculation took around 100 seconds. The resulting file, a matrix of dimension 1027 x 1380 x 114, was saved for later analysis.

A radiometric solid was also produced for clear visualization of the sBSDF results. The saved file was converted to a 1027 x 1380 x 3 matrix, by calculating the R, G, and B values associated to the estimated transmittance spectrum at each pixel (as described in section 7.1). These R,G, and B values were used to color the radiometric solid such that each BSDF matched the color of light transmitted at its emerging angle when the fenestration system was illuminated by sunlight. The transmittance spectrum was also integrated over 400 to 900nm to get a total radiance estimate for each pixel, which determined the radial distance of each point on the solid from the origin.

The resulting radiometric solid is shown in Figure 8.17, at different view angles. Because of limited access to Star-P, this automation process could only be run once. Thus, the solid is the result of an early iteration of the automation codes, and does not depict accurate spectral information. The radiometric solid and color scale, however, are similar to what would be expected from the final version of the automation process.

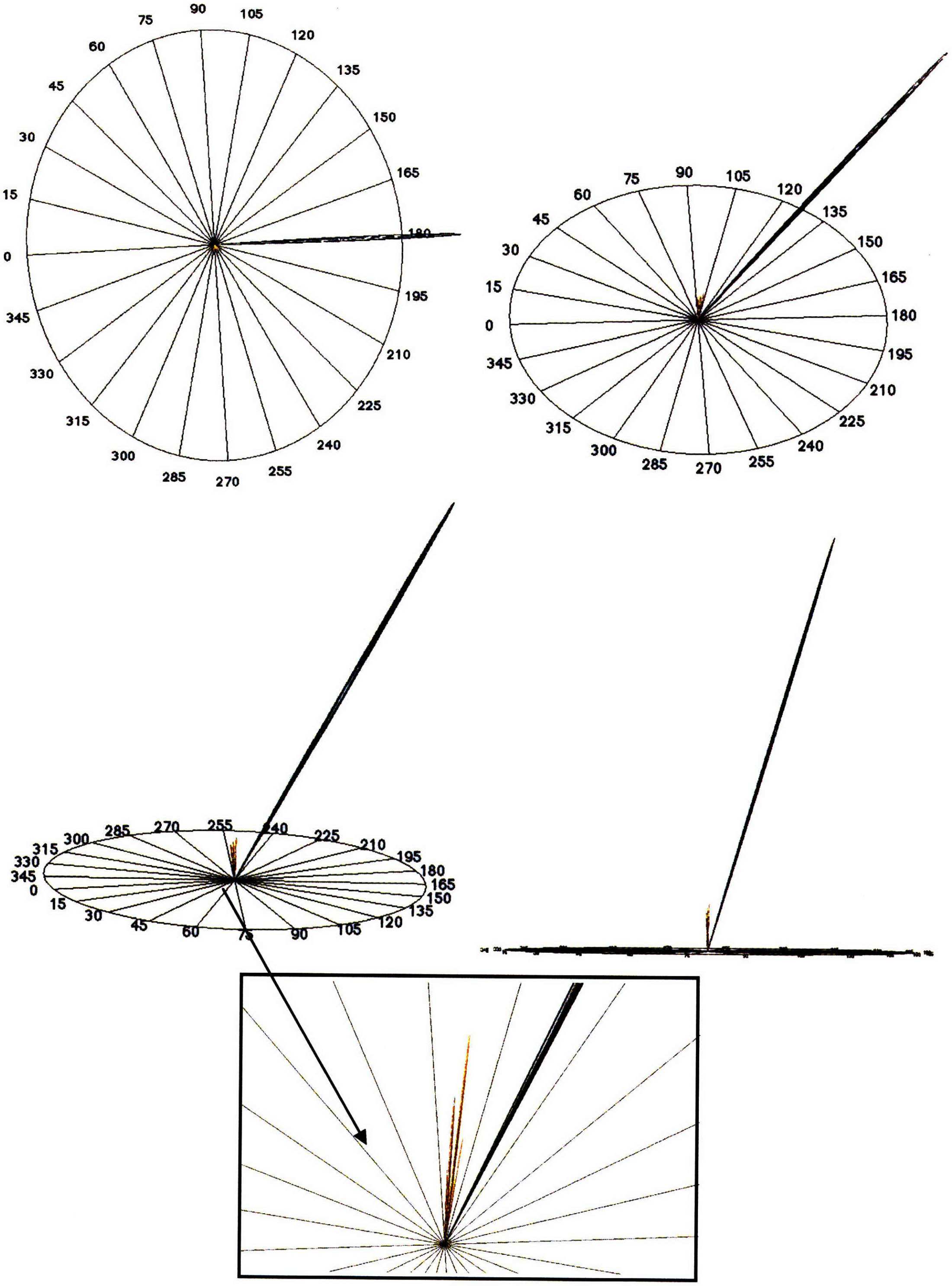

Figure 8.17 Four views of a radiometric solid from the sBTDF analysis of an HOE window element. Additional close-up view of scattered radiation

The sBTDF successfully calculates the specular portion of the beam, outlined in black. This portion is transmitted directly through the HOE without significant spectral or angular modification, and thus has a much greater magnitude and neutral color, as shown. The solid also successfully depicts the angles at which the sample scatters the transmitted radiation. The BTDF of these emerging angles are depicted in their respective colors close to the sample plane.

Though these graphics illustrate the success of the automation process and assure the eventual reliability of results, further work must be completed on the sBSDF calculation before these results are usable. A permanent computing method must be chosen, so that sBSDFs can be calculated easily and with less computing power. Also, spatial averaging methods must be completed so that BSDFs can be represented at any sr^{-1} resolution. Additionally, for both the sBSDF and pBSDF assessment, the results should be extensively tested on many types of fenestration systems and compared to documented results from other validated goniophotometers and goniospectrometers.

9. Conclusion

The inauguration of advanced fenestration systems into the daylighting toolkit has opened the door for daylighting design strategies that could significantly lessen energy consumption in buildings while enabling visual comfort and inherent natural lighting benefits. In order to effectively capitalize on these benefits, advanced fenestration system's spectral and angular properties must be better characterized, so they can be correctly integrated into specific façade designs.

An innovative video-goniospectrometer, the MIT Heliodome, was designed for this purpose—to measure the bidirectional angular and spectral properties of advanced fenestration systems quickly and completely. The Heliodome is novel in its ability to produce continuous photometric and spectral radiometric BSDFs across the visible and near infrared spectrum in a time-efficient manner.

9.1 Achievements

The major accomplishments outlined in this thesis pertain to the later stages of the Heliodome development—specifically the development and characterization of the final hemi-spheroid, the development of the spectral estimation method for spectral radiometric BSDF assessment, the calibration of the Heliodome for photometric BSDF assessment, and the automation and validation of the final instrument. The Heliodome has been used to calculate a spectral radiometric BSDF for a Holographic optical element and a photometric BSDF for a diffuse paper material, demonstrating the usefulness of the instrument and the deliverables expected from its employment.

One of the major obstacles to the development of the Heliodome was the production of a geometrically accurate hemi-spheroid for transportation of rays emerging from the sample to the fisheye lens of the camera. After assessing the problems with previous spheroid iterations and relying on a new acrylic forming method, a workable hemi-spheroid was produced and analyzed. The spectral transmission and reflection coefficients were measured across the full 380nm-1700nm visible and NIR spectrum and were interpolated to describe the spectral properties of all angles on the hemispheroid.

Building on a priori radiometric assessment methods (Gayeski 2007b), a spectral estimation procedure was also developed to reconstruct an unknown sample's angular reflectance and transmittance from quasi-spectral radiometric BSDFs. Known spectral information from each of the Heliodome's components were used to create an ill-posed system of equations connecting the camera's color channel output in each filterband in each pixel with the associated unknown spectral distribution reaching the camera from each emerging sample direction. Regulation methods and a smoothness constraint were applied to this ill-posed system to achieve a best "estimate" for the spectral angular properties of the sample. The method was validated for several real and hypothetical samples, achieving average improvements of 50% over the Heliodome's previous quasi-spectral method. As such, this method makes the Heliodome the first video-goniospectrometer, producing continuous spectral radiometric BSDFs.

Though this information can be produced in a time-efficient manner, a luminance calibration on the CCD camera made it possible to calculate photometric BSDFs with a less involved procedure, reducing the acquisition time by more a factor of eight. The camera's sensitivity curves were altered with cut-off filters and combined such that their scaled additive result was close to the human photopic sensitivity. The camera's grey levels were then correlated to luminance values for each camera integration time, and validated for a variety of spectral samples. The photometric calibration delivered accurate luminance estimations to within 10% in these validations, with an average error of 4.9%.

The procedures for the calculation of photometric BSDFs and spectral radiometric BSDFs were automated in MatLab codes. At each stage, predictable errors in the system were corrected, such that an accurate final result could be produced. The final global relative error for photometric BSDFs was 9.9%, and the global relative error for spectral BSDFs was 12.8%. This automation was tested through the BSDF assessment of two samples, a HOE for spectral BSDF assessment and a diffuse paper sample for photometric BSDF assessment. For both of these samples, the resulting total BSDF for the chosen incident angle was proved the success of the automation process and demonstrated the feasibility of achieving accurate and efficient BSDFs from the Heliodome.

The Heliodome was validated through an approach similar to the one used in (Andersen 2006b). At each stage the error contribution was appraised through a series of experiments that isolated the potential causes of radiometric, photometric, and spatial distribution uncertainties. A total relative global error was calculated based on each parameter's error contribution. This method predicted a photometric BSDF error of 10% and a spectral radiometric BSDF error of 13%, indicating that the instrument has the capability of providing reliable information about the light distribution characteristics of advanced fenestration systems.

9.2 Outlook

With the completion of this research, the Heliodome has just reached the stage where it has the ability to produce analyzable results. However, there is still work to be done on the instrument before it can easily assess the BSDFs of advanced fenestration materials.

To start, some mechanical elements and processing procedures must be solidified. Firstly, the accuracy of angular positioning with the table's azimuth and altitude motors must be improved. Once the table's motors are fully functional and validated for their precision, additional validation procedures will become simpler.

One such procedure is the final validation of the spheroid's spatial calibration. In this validation, the sample's emerging angular directions should be checked against pixel locations for accuracy. Since a high degree of angular accuracy is needed for this validation, it would be best performed with a stationary light source once the table is accurately able to position itself. This would ensure that the incident beam angle corresponds exactly to an individual pixel on the output image.

Additionally, while the spheroid has been characterized for visible and NIR spectral transmission and reflection, the characterization method relied on interpolation to simplify the measurement process. Once the table's positioning system is complete, it would be useful to validate this characterization for a finer angular grid, as insurance against local imperfections in the coating of the hemi-spheroid. Knowledge of the spectral characteristics of the dome to a higher degree of accuracy will directly enable more precise photometric and spectral radiometric BSDFs.

One easy method of completely characterizing the spectral reflectance of the dome, would be to apply the spectral estimation method developed in this thesis. Using a 10cm diameter reflectance standard as the sample, the CCD camera and filtering system could be used to capture images, as for a spectral radiometric BSDF assessment. However, since the sample's sBSDF is known, the spectral estimation method, instead, would solve for $\rho_{spheroid}$ at each pixel. Through the spatial calibration, these $\rho_{spheroid}$ estimations could then be associated to positions on the spheroid surface. Because the relationship between $\rho_{spheroid}$ and $\tau_{spheroid}$ is known, and because the relative spectrum of $\tau_{spheroid}$ has been measured, this one image could capture all of the information needed to characterize the spectral reflectance and transmittance coefficients for every position on the hemi-spheroid.

To enable the Heliodome to accurately evaluate radiation over the visible and near infrared spectrum, the NIR camera's calibration must also be validated. While some work has been done to establish the absolute spectral responsivity of the camera to polychromatic radiation, this calibration must be validated using the NIR 512 spectrometer. Furthermore, an application must be designed to enable remote NIR image capture and control of integration times, as was done with the Kappa visible CCD camera.

Finally, the image capture process must be automated, such that the filter wheel, beam shaper, camera, and table can be controlled from a user's interface. This interface should allow selection of incident angle, assessment mode (reflection or transmission), result type (pBSDFs or sBSDFs), angular resolution, and spectral range. It should also organize the results such that they can be easily integrated into existing databases, such as Windows 5.

At that phase, the true completion of the instrument, several additional fenestration materials should undergo a complete BSDF assessment. Especially for materials that have already been characterized with other validated goniophotometers, a deeper pool of results will allow the Heliodome to be critically evaluated. Additionally, the Heliodome should be validated through other more common methods, such as through the use of an Ulbricht sphere measurement or ray-tracing softwares (Andersen 2006b). Testing the Heliodome with a large range of fenestration samples will almost certainly illuminate problematic areas for improvement.

However, even before these tests are performed, there is much that can already be improved upon to enhance its accuracy, efficiency, and applicability.

One suggested improvement is an additional characterization of both cameras using a flat fielding technique. This method utilizes an integrating sphere to flood the camera's field of vision with equally distributed radiation. As such, small differences in the response of image pixels could be detected and corrected. However, if the characterization method of the spheroid, described above, were enacted, the information gleaned from flat-fielding would already be incorporated into the reflectance and transmittance coefficients of the spheroid.

Other possible future enhancements include the purchase of additional filters for quasi-spectral analysis of the NIR spectrum. While the spectral estimation method would have to be slightly altered to accommodate the change from three color channels to one channel in the NIR camera, the principles behind the method could still be applied. Even a few filters in the NIR spectrum may be useful in the characterization of layered fenestration systems meant to handle solar gains through spectral selectivity.

9.3 Applications

With the advent of more stringent building codes and a heightened awareness of energy efficiency in buildings, there is a greater reliance on passive lighting, heating, and cooling strategies. For energy, comfort, health, aesthetic, and even artistic means, advanced fenestration systems can be a medium enabling the graceful use of daylighting in a space.

The use of the Heliodome and the research documented in this thesis to further the understanding of these systems through complete BSDF characterization will prompt enhancements in CFS design and facilitate their integration into new and existing building facades. The fenestration industry is certainly interested in this kind of characterization, as it will provide them with a rapid less expensive feedback from window prototypes, detailed information on developed products, and a means for quantifying goals in new product performance.

As the industry changes to accommodate these new products, architects must also become informed about fenestration system performance. Without an objective representation of the product's function and performance, it will be difficult to choose which system most effectively addresses their specific design challenges. While new software databases, such as D-lite are being designed with a function based categorization system in mind, the database would be ineffective without correct and complete BSDF data to feed into the foundation of the database. Even if this data isn't applied directly by designers, its incorporation into simulation tools will considerably broaden the range of assessable daylighting strategies.

The goniospectrometer's rapid BSDF assessment could be interesting to a number of industries. Because our understanding of the physical world is largely based on the intersection of light and materials, understanding the details of how radiation is spectrally and angularly modified by objects and material combinations has applications in a number of fields--ranging from computer science to material science to mapping terrains and art archiving.

However, the instrument's development is justified by its immediate application alone—to foster the urgent and informed integration of CFS into our building stock. Through the invention of a tool that can rapidly characterize a window system's performance, the design of passive systems that stringently control visible light and solar gains can be easily advanced. By utilizing these advanced daylighting systems that can distribute light intelligently in a space, it is possible to take full advantage of our solar resources, improving our health, our comfort, and our environment.

Appendix A. NIR Calibration

The Heliodome uses an Indium-Gallium Arsenide camera in conjunction with the Kappa CCD camera to measure radiation between 900-1700nm. In order to use the output of the camera to estimate the radiance of a scene, the NIR camera must be calibrated in a similar manner as the CCD camera (described in chapter 5). However, unlike in color CCD cameras, there is only one channel to determine spectral sensitivity. While the radiometric response of the NIR camera has been determined for monochromatic beams, the camera's absolute spectral responsivity remains to be validated.

The NIR camera was calibrated for monochromatic beams in a similar manner as the CCD camera in (Gayeski 2007b). In both the NIR and CCD color camera the digital output of the camera is directly related to the spectral exposure h(λ), which is dependent on the number of photons exciting the camera's sensor area. The relation:

$$NDL_{NIR} = \frac{DL}{(2^{16}-1)} = f(h(\lambda)) \qquad \text{(A.1)}$$

links digital level (DL) and normalized digital level (NDL) to spectral exposure of the NIR camera through a dose response function. This function was determined experimentally by measuring the response of the camera against monochromatic beams of known radiances.

A 50W tungsten halogen lamp was used at power levels from 20% to 70% to vary the intensity of the beam at each wavelength. This source was transmitted through a monochromator, a shortpass filter cutting out second order peaks, and a series of lenses focusing the beam to achieve a bright even spot. The irradiance of the beam exiting the monochromator port was then measured with a germanium detector that had previously been calibrated.

As in the CCD camera calibration, ideally this beam would have then been reflected off a reflectance standard and captured by the camera to correlate pixel values with radiances. However, due to the low light levels exiting the monochromator port, it was impossible to achieve high enough NDLs to characterize the full dose response function accurately when this additional reflection was included. The results, instead, characterize the lower part of the dose response curve accurately, but do not provide adequate information to determine the camera's response at higher radiances as shown in Figure A.1.

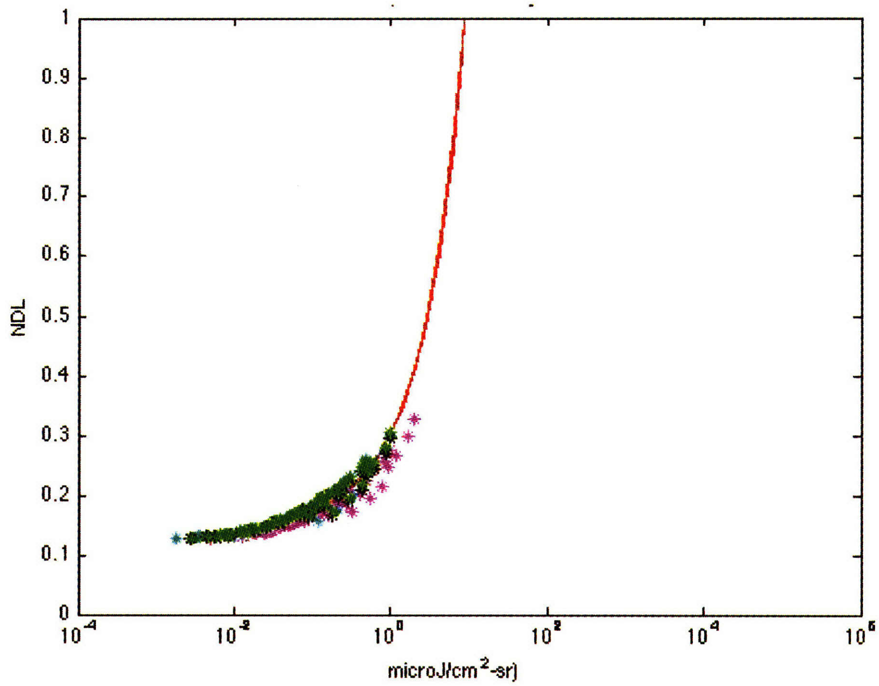

Figure A.1 Lower portion of the NIR logistic digital response curve

In figure A.1, the red line is a projected curve fit, whereas the green and pink dots are actual measured radiances.

To characterize the response function more completely, the camera was situated facing the monochromator port directly. The irradiance of the beam, measured by a germanium detector, was then compared with the pixel digital levels from the resulting image. The power level of the lamp and integration time of the camera were varied in order to capture images with pixel values that would span the full range of NDLs for each wavelength. These NDLs were then graphed against the beam's corresponding irradiances recorded by the germanium detector. This method eliminated the light loss caused by the reflectance standard, enabling a more certain curve fit shown in Figure A.2.

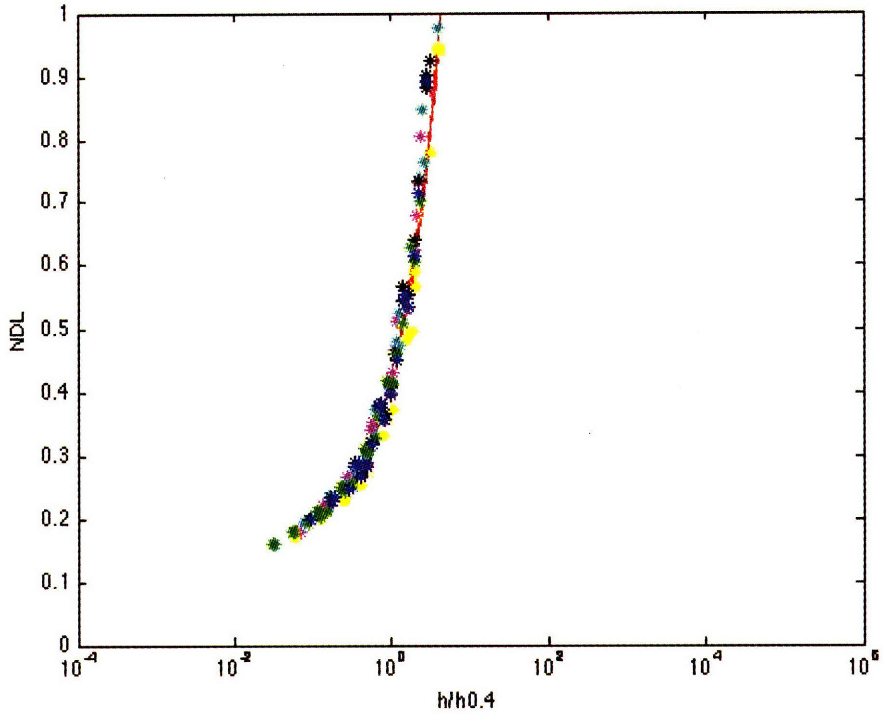

Figure A.2 Logistic dose response curve for the NIR camera defined by the relationship between spectral exposure and normalized digital level.

As with the CCD camera, this relationship was found to be the same for all wavelengths. That is, given an arbitrarily chosen NDL, for example 0.4, the ratio of $h(\lambda)$ to the $h(\lambda)$ corresponding to NDL 0.4, ($h^{0.4}(\lambda)$), is the same for any wavelength. This curve was determined to fit closest to a logistic curve, as opposed to the Gaussian fit used in preliminary assessments (Gayeski 2007b), defined by the equation:

$$NDL_{NIR} = \alpha' + \frac{\beta'}{1 + \left(\frac{h(\lambda) / h_{NIR}^{0.4}(\lambda)}{\gamma'} \right)^{\delta'}} \qquad (A.2)$$

where $\alpha,\beta,\gamma,\delta$ are experimentally derived constants:
$\alpha'=.141$, $\beta'=147.09$, $\gamma'=28897.04$, $\delta'=-0.664$

Once the digital response function was found for monochromatic beams, the relative spectral responsivity of the camera was determined. The NIR camera was positioned facing a reflectance standard illuminated by the same source, monochromator, filters, and lenses used to characterize the camera's dose response. For five different lamp power levels, the camera imaged monochromatic wavelengths at 25nm increments across the 900-1700nm spectrum, as shown in Figure A.3.

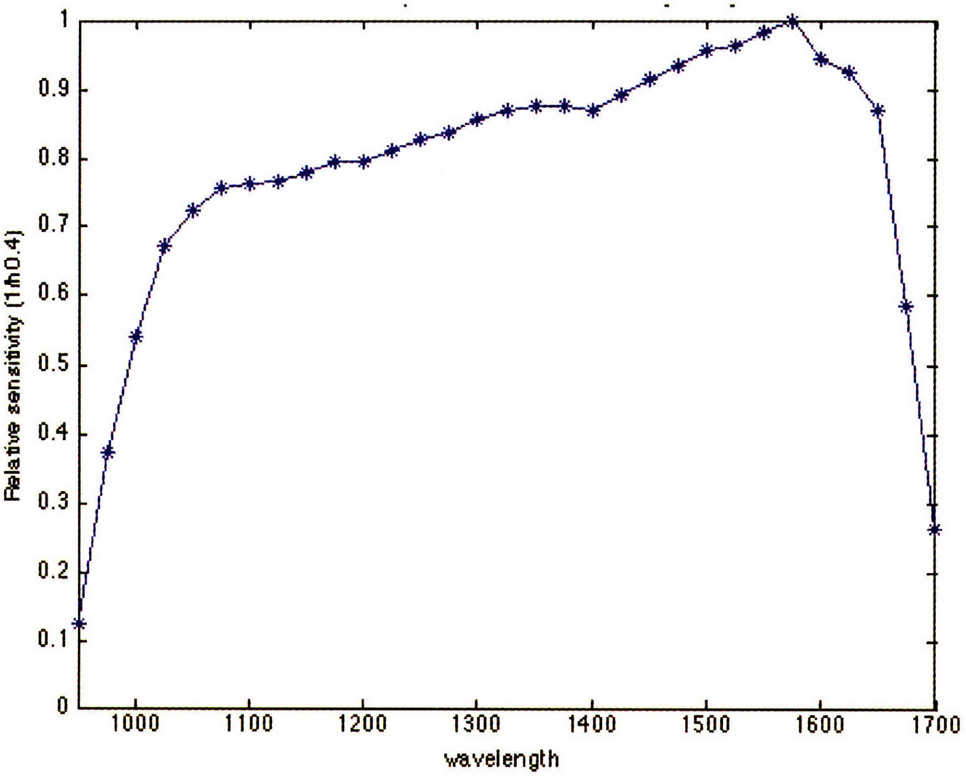

Figure A.3. Relative sensitivity of the NIR camera

The relative sensitivity closely matches the results from the manufacturer's specifications and from the preliminary assessment (Gayeski 2007b), despite the different chosen methods and dose response fits.

The absolute spectral responsivity of the NIR camera remains to be validated using the NIR spectrometer. Using monochromatic radiation, the NIR spectrometer can be used to scale the relative sensitivity curve to its appropriate magnitude. The NIR camera's dose response function must also be validated for polychromatic radiation using the spectrometer before it is usable in the Heliodome set-up.

Appendix B. Camera and Lamp Settings

The settings on the camera and HMI dedolight greatly influence the results achieved. Because all of the calibrations and experimentation were completed with assumed settings, these settings must not be changed during the BSDF assessment or the results and error analysis will not be valid.

The camera was calibrated with the least amount of photo manipulation, according to the settings in Table B.1.

Kappa	**Settings**
High	4095
Low	150
Gain	0
R,G,B	0
Gamma	50
Filters: Sharp Edge	0 0
Color mode	2
image size	1380 x 1024

B.1 ImageBase Control settings for Kappa CCD camera

The lamp was chosen to have a beam spread of 2.4 degrees and to be set on spotlight mode in order to induce maximum collimation.

Appendix C. Nomenclature

B_{major}	Magnification/concentration of irradiance spot hitting CCD camera fisheye due to spheroidal geometry
BRDF	Bidirectional Reflection Distribution Function (sr^{-1})
BSDF	Bidirectional Scattering Distribution Function (sr^{-1})
BTDF	Bidirectional Transmission Distribution Function (sr^{-1})
$CS_{j,\lambda}(\theta_i,\phi_i,\theta_r,\phi_r)$	discrete conglomerate spectrum (for filterset j) for designated incident and emerging angles (μW/m^2-sr)
d	digital response vector (components in units NDL/s
$\overline{d}$	digital response vector with randomly distributed noise
D	diameter of the fenestration sample (cm)
$D_{sampleplane}$	diameter of beam at sample plane (cm)
D_{lamp}	diameter of beam at lamp (cm)
e (subscript)	denotes a radiometric quantity
$E(\theta_i)$	total illuminance of incident beam (lux)
$E_{e,\lambda}(\theta_i,\sigma)$	spectral irradiance on the sample plane due to the incident beam's flux between 380nm and 945nm (μW/m^2) 380nm and 945nm
f_i	individually affected parameter error for global error assessment
f_1'	CIE (1987) measure of agreement between two spectra (percentage)
h	distance from lamp to sample port

$h^{0.3}{}_{R,G,B}(\lambda)$	spectral exposure required to yield a normalized digital level of 0.3 in the CCD camera
$h^{0.3}_{R,G,B,beam}$	total exposure of a polychromatic beam required to yield a normalized digital level of 0.3 in the CCD camera
j (subscript)	filter combination number
k (as index)	truncation parameter (constant)
$L_{e,j\lambda,cam}(\theta_i,\phi_i,\theta_r,\phi_r)$	discretized spectral bidirectional filtered radiance seen by the camera (μW/m^2-sr)
L_λ	spectral luminance viewed by the camera in discrete wavelength increments (cd/m^2)
$L_{sample}(\theta_i,\phi_i,\theta_r,\phi_r)$	total bidirectional luminance distribution emerging from sample (cd/m^2)
$L_{e,beam,380-945}$	total radiance of a polychromatic beam (μW/m^2-sr)
$L_{e,sample,\lambda}(\theta_i,\phi_i,\theta_r,\phi_r,\sigma)$	spectral bidirectional radiance of emerging from sample (μW/m^2-sr)
$L_{e,j\lambda,cam}$	spectral radiance viewed by the camera through filter j in discrete wavelength increments (μW/m^2-sr)
$M_{HMI,\lambda}$	spectral exitance of the HMI dedolight in discrete wavelength increments (μW/m^2)
n (index)	index identifying element in discretized vector
N	radiance matrix (components in units NDL/s) computed for an arbitrary pixel
$N(\theta_i,\phi_i,\theta_r,\phi_r)$	radiance matrix (components in units NDL/s) computable for every pixel
N^+	psuedoinverse of the radiance matrix
N_f	number of individually affected parameter errors

NDL_{NIR}	normalized digital level (digital level divided by 2^{16}) for the NIR camera
$NDL_{R,G,B}$	normalized digital level (digital level divided by 2^{8}) in the red, green, or blue channel
$NDL_{R,G,B,j}$	normalized digital level (digital level divided by 2^{8}) in the red, green, or blue channel for filtered radiation from the filterset j
P	function used to translate spectra into X,Y,Z coordinates
$pBSDF$	photometric BSDF (cd/m^2-sr)
Q_f	flatness quotient, where spectral flatness is defined as having a $Q_f<0.1$
Q_s	smoothness quotient, where spectral smoothness is defined as having a $Q_s<0.1$
$r_{R,G,B}(\lambda)$	absolute spectral responsivity of CCD camera in the red, green, and blue channel (NDL/(μJ/m^2-sr))
$r_{R,G,B,\lambda}$	discretized absolute spectral responsivity measured for all three channels in 5nm intervals
S	second difference smoothing matrix
s	distance between sample and point of reflection on spheroid (cm)
$S(\lambda)$	modified camera sensitivity for pBSDF measurement
sBSDF	spectral radiometric BSDF (μW/m^2-sr)
t_{int}	integration time for the camera (ms)
U	orthonormal vectors to V from TSGVD of N
V	orthonormal vectors to U from TSGVD of N
X	vectors resulting from GSVD decomposition
X,Y,Z	chromaticity coordinates

x_n	n^{th} vector of matrix X from the generalized singular value decomposition.
$\bar{x}, \bar{y}, \bar{z}$	CIE standard 2° observer functions
$\alpha, \beta, \gamma, \delta$	experimentally derived CCD camera calibration constants
$\alpha', \beta', \gamma', \delta'$	experimentally derived NIR camera calibration constants
$\ell(\lambda)$	standard CIE daylight D65 spectral distribution ($\mu W/m^2$)
ε	error added to digital response vector
$\varepsilon_{BT(R)DF}$	BSDF global assessment error
$\varepsilon_{pBT(R)DF}$	photometric BSDF global assessment error
$\varepsilon_{srBT(R)DF}$	spectral radiometric BSDF global assessment error
Γ_{calib}	spectral radiance of light source used for photometric calibration
Γ_{meas}	spectral radiance of light source used for pBSDF measurement
$\Delta\lambda_j$	wavelength interval corresponding to filterband j for quasi-spectral estimation
λ (subscript)	indicates a spectral distribution of a radiometric quantity recorded in discrete wavelength increments
ϕ_i	incident azimuth angle (radians)
ϕ_r	reflected azimuth angle (radians)
σ	polarization state of incident and emerging radiation
$\bar{\rho}$	estimated spectral reflectance or transmittance with error component in d
ρ_{box}	average reflectance or transmittance for each waveband determined by the camera's filtered radiance predictions

ρ_k	estimated spectral reflectance or transmittance using TSVD, truncating at k singular values
ρ_{reg}	estimated spectral reflectance or transmittance of the fenestration sample using regulation methods
ρ_{sample}	measured spectral reflectance or transmittance for the sample for a single pixel
$\rho_{sample,\lambda}(\theta_i,\phi_i,\theta_r,\phi_r)$	discretized bidirectional "reflectance" of the sample (the same as a spectral radiometric BSDF)
$\rho_{spheroid}(\theta_i,\phi_i,\theta_r,\phi_r)$	bidirectional spectral reflectance of the spheroid for characterization
$\rho_{spheroid,\lambda}(\theta_r,\phi_r)$	spheroidal reflectance for radiation emerging from the sample (transmission and reflection measurements)
$\emptyset_n$	nth singular value from the truncated singular value decomposition
$\tau_{filter,j,\lambda}$	filterset j discretized spectral transmittance
Σ	The singular values vector of N, with the singular values in non-decreasing order
$\tau_{spheroid}(\theta_i,\phi_i,\theta_r,\phi_r)$	bidirectional spectral transmittance of the spheroid (for characterization)
$\tau_{spheroid}(\theta_i,\phi_i)$	discretized spectral transmittance of the spheroid for an incident beam (reflectance mode)
ξ	Tikhonov regulation parameter
θ_i	incident altitude angle (radians)
θ_r	reflected altitude angle (radians)
$(\theta_i,\phi_i,\Delta\theta_r,\Delta\phi_r)$	spatial grouping determined by the angular resolution

References

American Society for Testing and Materials (ASTM). (2008). Reference Solar Spectral Irradiance: Air Mass 1.5. Internet WWW page at URL: <http://rredc.nrel.gov/solar/spectra/am1.5/> (Accessed 04.08.08).

American Society for Testing and Materials (ASTM). (1996). Standard Practice for Lighting Cotton Classing Rooms for Color Grading. *D1684-96*, Philadelphia, Pa.

Ander, G. (1995). Fundamentals of Daylighting. *Daylighting Performance and Design*, New York: Van Nostrand Reinhold. 1-5.

Andersen, M., Kleindienst, S., Yi, L., Bodart, M., and Cutler, B. (2008). An intuitive daylighting performance analysis and optimization approach. *Building Research and Information*, In Press.

Andersen, M. and de Boer, J. (2006a). Goniophotometry and assessment of bidirectional photometric properties of complex fenestration systems. *Energy and Buildings*, 38(7):836-848.

Andersen, M. (2006b). Validation of the performance of a new bidirectional video-goniophotometer.*Lighting Research and Technology*, 38 (4):295-311.

Andersen, M., Rubin, M., Powles, R., Scartezzini, J.-L. (2005a). Bi-directional transmission properties of Venetian blinds: experimental assessment compared to ray-tracing calculations. *Solar Energy*, 78 (2): 187-198.

Andersen, M., Ljubicic, D., Browne, C., Kleindienst, S., Culpepper, M. (2005b). An automated device to assess light redirecting properites of materials and perform sun course simulations: the Heliodome project. In *Proceedings of the 2005 Solar World Congress*, Paper #1220, Orlando, August 6-12.

Andersen, M. and Scartezzini, J.-L. (2004a). Inclusion of the specular component in the assessment of bidirectional distribution functions based in digital imaging. *Solar Energy*, 79 (2):159-167.

Andersen, M., Rubin, M., Scartezzini, J.-L. (2004b). Comparison between ray-tracing simulations and bi-directional transmission measurements on prismatic glazing. *Solar Energy*, 74(2): 157-173.

Andersen, M., (2004c). *Innovative Bidirectional Video-Goniophotometer for Advanced Fenestration Systems.* Ecole Polytechnique Federale de Lausanne, Ph.D in Physics Thesis.

Andersen, M. (2002). Light distribution through advanced fenestration systems. Building Research and Information, 30 (4): 264-281.

Andersen, M., Michel, L., Roecker, C., Scartezzii, J.-L. (2001). Experimental assessment of bi-directional transmission distribution functions using digital imaging techniques. *Energy and Buildings* 33: 417-431.

Apian-Bennewitz, P. (2006). pab gonio-photometer ii. Internet WWW page at URL< http://www.pab-opto.de> (Accessed 03.20.08).

Apian-Bennewitz, P. and von der Hardt, J. (1998). Enhancing and calibrating a goniophotometer. *Solar Energy Materials and Solar Cells* 54 (1–4):309–322.

Apian-Bennewitz, P. (1994a) Designing an apparatus for measuring bidirectional reflection/transmission, In *Proceedings of the SPIE: Optical Materials Technology for Energy Efficiency and Solar Energy Conversion XIII*, 2255: 697–706.

Apian-Bennewitz, P., von der Hardt, J., and Goller, M. (1994b). Characterization of aerogels for computer simulations. In *Seventh International Meeting on Transparent Insulation Technology.*

Arasteh, D., Selkowitz, S., Apte, J., and LaFrance, M. (2006). Zero Energy Windows. In *Proceedings of the 2006 ACEEE Summer Study on Energy Efficiency in Buildings*, Pacific Grove, CA.

Arasteh, D., Mitchell, R., and Kohler, C. (2001). Improving Information Technology to Maximize Fenestration Energy Efficiency, In *Performance of Exterior Envelopes of Whole Buildings VIII: Integration of Building Envelopes Proceedings*, Berkeley, CA.

Ashdown, I. (2000). Comparing Photometric Distirbutions, *Journal of the Illuminating Engineering Society*, 27 (1): 67-79.

Aydinli, S. (1996). Short description of the spiral goniophotometer for bi-directional measurements. In *Report for IEA SHC Task 21, ECBCS Annex 29, Subtask A*, Technische Universität Berlin (TUB), Berlin.

Badia, P., Myers, B., Boecker, M., and Culpeper, J. (1991). Bright light effects on body temperature, alertness, EEG and behavior. *Physiology and Behavior*, 50: 583-588.

Billmeyer, F. and Saltzman, M. (1981). *Principles of Color Technology, 2nd edition*, New York: John Wiley & Sons.

Browne, C. (2006). *Development of a light detection system for bidirectional measurements over the solar spectrum and sun course simulations with scale* *models*. Massachusetts Institute of Technology, Master of Science in Building Technology Thesis.

Berson, D.M., Dunn, F.A., Takao M. (2002). Phototransduction by retinal ganglion cells that set the Circadian clock. *Science* 295: 1070-1073.

Boyce, P.; Hunter, C.and Howlett, O. (2003a). The Benefits of Daylight through Windows. Lighting Research Center, Rensselaer Polytechnic Institute, Sponsored by the U.S. Department of Energy.

Boyce, P., Akashi, Y., Hunter, C. , and Bullough, J. (2003b). The impact of spectral power distribution on the performance of an achromatic visual task, *Lighting Research and Technology*, 35: 141-161.

Boyce, P.(2003c). *Human Factors in Lighting*. CRC Press.236.

Boyce, P., Beckstead, J., Eklund, N., Strobel, R., and Rea, M.(1997). Lighting the graveyard shift: the influence of a daylight-simulating skylight on the task performance and mood of night-shift workers. *Lighting Research and Technology*, 29:105-142.

Boyce, P., Lloyd, C., Eklund, N. and Brandston, H. (1996). Quantifying the effects of good lighting: the Green Hills Farms project. In *Proceedings of the Illuminating Engineering Society of North America Annual Conference*, Cleveland, IESNA: New York.

Brainard, G., Hanifin, J., Greeson, J., Byrne, B., Glickman, G., Gerner, E. and Rollag, M. (2001). Action spectrum for melatonin regulation in humans: evidence for a novel circadian photoreceptor. *Journal of Neuroscience*, 21: 6405-6412.

Breitenbach, J. and Rosenfeld, J.L.J. (1999). Goniospectrometer measurements of the optical performance of a holographic optical element. *Solar Energy*, 68(5): 427-437.

Breitenbach, J. and Rosenfeld, J.L.J. (1998). Design of a photogoniometer to measure angular dependent optical properties. In *Proceedings of International Conference on Renewable Energy Technologies in Cold Climates*. Solar Energy Society of Canada Inc., Ottawa, 386–391.

Browne, C. (2006). *Development of a light detection system for bidirectional measurements over the solar spectrum and sun course simulations with scale models*. Massachusetts Institute of Technology. Master of Science in Building Technology Thesis.

Building Owners Managers Association International (BOMAI) (1988). *Office Tenant Moves and changes: Why Tenants Move, What They Want, Where they Go*, BOMAI: Washington DC.

Campbell, S., Dijk, D., Boulos, Z., Eastman, C., Lewy, A., and Terman, M., (1995). Light treatment for sleep disorders: consensus report III: Alerting and activating effects. *Journal of Biological Rhythms*, 10(2): 771-82.

Carmondy, J., Selkowitz, S., Lee, E., Arasteh, D., Willmert, T. (2004). Window Systems for High Performance Buildings. *The Regents of the University of Minnesota*, New York, NY.

Chain C, Dumortier D, Fontoynont M. (2001). Consideration of Daylight's color. *Energy and Buildings*, 22: 193-198.

Chen, Allan (2004). The New York Times Building: Designing for Energy Efficiency through Daylighting Research. *Science Beat,* Feb. 17. Lawrence Berkeley National Lab.

Collins, L. (1975). Windows and people: a literature survey--Psychological reaction to environments with and without windows. *NBS Buildings Science Series*, 70.

Commission Internationale de l'Eclairage (CIE) (1991). CIE standard colorimetric illuminants. *CIE*, 10526.

Commission Internationale de l'Eclairage (CIE) (1987). Methods of characterizing illuminance meters and luminance meters—Performance, characteristics and specifications. *CIE*, 69.

Commission Internationale de l'Eclairage (CIE) (1977), Radiometric and photometric characteristics of materials and their measurement. *CIE*, 38 (TC-2.3).

Commission Internationale de l'Eclairage (CIE) (1971), Colorimetry: Official Recommendations of the International Commission on Illumination. *CIE*, 15 (E-1.3.1).

Commission Internationale de l'Eclairage (CIE) (1932). *CIE Proceedings,1931.* Cambridge University Press, Cambridge.

Connah D, Westland S, Thomson MGA (2001). Recovering spectral information using digital camera systems. *Color Technology*, 117: 309-312.

Cutler, B., Martin, S., Yu, S., Glaser, D., Andersen, M. (2008). Interactive Selection of Optimal Fenestration Materials for Schematic Architectural Daylighting Design. *Automation in Construction*, In Press.

Cuttle, C. (1983). People and windows in workplaces. In *Proceedings of the People and Physical Environment Research Conference*. Wellington, New Zealand.

Dasgupta, U. (2003). *The impact of windows on mood and the performance of judgemental tasks*. Rensselaer Polytechnic Institute. Masters of Science in Lighting Thesis.

Denial, J.-M., (2002) Modélisation des luminaires et des BRDF: réalisation, mesure et compression. Université de Rennes 1. PhD thesis.

Dijk, D.-J., Boulos, Z., Eastman, C., Lewy, A., Campbell, S., and Terman, M. (1995). Light treatment for sleep disorders: Consensus report II Basic properties of circadian physiology and sleep regulation. *Journal of Biological Rhythms*, 10: 113-125.

Energy Center of Wisconsin (2005). *Energy Savings from Daylighting: A Controlled Experiment*. ECW Report Number 233-1.

Eklund, N., (1999). Exit sign recognition for color normal and color deficient observers. *Journal of the Illuminating Engineering Society*, 28: 71-81.

Figueiro, M., Rea, M., Stevens, R., and Rea, A. (2002) Daylight and Productivity: A Possible Link to Circadian Regulation. In *Light, and Human Health: EPRI/LRO 5th International Lighting Research Symposium*, Palo Alto, CA,185-193.

Gayeski, N. and Andersen, M. (2007a). New Methods for Assessing Spectral, Bi-directional Transmission and Reflection by Complex Fenestration Systems. In *Proceedings of SOLAR 2007: Sustainable Energy Puts America to Work*, Cleveland, 7-10.

Gayeski, N. (2007b). *New Methods for Measuring Spectral, Bi-directional Transmission and Reflection using Digital Cameras*. Massachusetts Institute of Technology. Master of Science in Building Technology Thesis.

Glickman, G., Hanifin, J.P., Rollag, M.D., Wang, J. Cooper, H. and Brainard, G.C. (2003). Inferior retinal light exposure is more effective than superior retinal exposure in suppression melatonin in humans. *Journal of Biological Rhythms*, 18 (1): 71-79.

Hansen, V., Lund, E. and Smith-Sivertsen, T. (1998). Self-reported mental distress under the shifting daylight in the high north. *Psychological Medicine*, 28: 447-452.

Hansen, P. (1998). *Rank-deficient and Discrete ill-posed problems: Numerical Aspects of Linear Inversion.* Philadelphia: SIAM.

Hansen, P., and O' Leary, D. (1993). The Use of the L-curve in the regularization of discrete ill-posed problems. *Journal of Scientific Computing*, 14:1487-1503. SIAM.

Hansen P. (1992a). *Regularization Tools: A Matlab Package for Analysis and Solution of Discrete Ill-Posed Problems.* Technical University of Denmark.

Hansen P. (1992b). Analysis of Discrete Ill-posed problems by means of the L-curve. *SIAM Review*, 34: 561-580.

Hansen P. (1988). Regularization GSVD and Truncated GSVD. Oak Ridge National Laboratory, TM 10779.

Hansen P. (1987). The truncated SVD as a method for regularization. *BIT*, 27: 534-553.

Hardeberg, J. (1999). *Acquisition and reproduction of color images: colorimetric and multispectral approaches*. Ecolé Nationale Superieure des Telecommunicationes. Ph.D. Thesis.

Heerwagen, J. and Heerwagen, D. (1986) Lighting and Psychological Comfort. *Lighting Design and Application*, 16(4): 47-51.

Heerwagen, J. and Orians, G. (1986). Adaptations to windowlessness: a study of the use of visual décor in windowed and windowless offices. *Environment and Behavior*, 18 (5): 623–639.

Hernandez-Andres, J., Nieves, J., Valero,,E., Romero, J. (2004). Spectral-daylight recovery by use of only a few sensors. *Journal of the Optical Society of America*, A 21: 13-23.

Heschong, L. (2002a). Daylighting and Human Performance. *ASHRAE Journal.* June.

Heschong, L., Wright, R., and Okura, S. (2002b). Daylight impact on retail sales performance. *Journal of the Illuminating Engineering Society*, 31: 21-25.

Heschong-Mahone Group (2003). Windows and Offices: A Study of Office Worker Performance and the Indoor Environment. Sacramento, CA: California Energy Commission.

Heschong-Mahone Group (1999a). Daylighting in Schools: An Investigation into the Relationship between Daylighting and Human Performance. Sacramento, CA: Pacific Gas and Electric Company.

Heschong-Mahone Group (1999b). Skylighting and Retail Sales: An Investigation into the Relationship between Daylighting and Human Performance. Sacramento, CA: Pacific Gas and Electric Company.

Hitchcock, R. and Carroll, W. (2003). DElight: A Daylighting and Electric Lighting Simulation Engine. In *Eighth International IBPSA Conference Proceedings.* Netherlands.

Hong, D. and Voss, K. (2004). Effects of point-spread function on calibration and radiometric accuracy of CCD camera. *Applied Optics*, 43 (3): 665-670.

Huang, C., Townshend, J., Liang, S., Kalluri, S., and DeFries, R. (2002). Impact of sensor's point spread function on land cover characterization: assessment and deconvolution. *Remote Sens. Environ.* 80: 203-212.

Imai, F., and Berns, R. (1999). Spectral estimation using trichromatic digital cameras. In *Proceedings of the International Symposium on Multipectral Imaging and Color Reproduction for Digital Archives.* Society of Multispectral Imaging of Japan.

Inanici, M. (2006). Evaluation of high dynamic range photography as a luminance data acquisition system. *Lighting Research & Technology*, 38: 1-14.

Jewett, M., Rimmer, D., Duffy, J., Klerman, E., Kronauer, R. and Czeisler, C. (1997). Human circadian pacemaker is sensitive to light throughout subjective day without evidence of transients. *American Journal of. Physiology*, 273: R1800-R1809.

Johnson, R., Sullivan, R., Selkowitz, S., Nozaki, S., Conner, C. and Arasteh, D. (1984). Glazing Energy Performance and Design Optimization with Daylighting. *Energy and Buildings*, 6: 305-317.

Kasper, S., Rogers, S., Yancey, A., Schulz, P., Skwerer, R., and Rosenthal, N. (1989). Phototherapy in individuals with and without subsyndromal seasonal affective disorder, *Archives of General Psychiatry*, 46: 837-844.

Koch, T. (2007). *Device for Selecting Lightwave Ranges via Computer Control for Studying Building Material Properties.* Massachusetts Institute of Technology. Bachelor's Degree in Mechanical Engineering Thesis.

Kruiithoff, A. (1941). Tabular luminescence lamps for general illumination. *Phillips Technology Review* 6(3):65-73.

Lawrence Berkley Lab (LBL) (2008). Chromogenic Materials. Internet WWW page at URL< http://windows.lbl.gov/materials/chromogenics/default.htm > (Accessed 04.28.08).

Leslie, R. (2003). Capturing the daylight dividend in buildings: why and how?. *Building and Environment* 38(2):381-385.

Li, C. and Luo, M. (2001). The estimation of spectral reflectances using the smoothness constraint condition. In *Proceeding of the 9th Color Imaging Science Conference*, Society for Imaging Science and Technology, Springfield.

Ljubicic, D. (2005). *Automated Support for Experimental Approaches in Daylighting Performance Assessment.* Massachusetts Institute of Technology. Bachelor's Degree in Mechanical Engineering Thesis.

Loftness, V. (2004*). Improving Building Energy Efficiency in the U.S.: Technologies and Policies for 2010 to 2050.* Pew Center on Global Climate Change. 2-3.

Maloney, L. (1986). Evaluation of linear models of surface spectral reflectance with small numbers of parameters. *Journal of the Optical Society of America*, A 3: 1673-1683.

McCluney, R. (2002) US Dept. of Energy Fenestration Research Grant Final Report. Florida Solar Energy Center, DE-FC36-96GO10136.

McCluney, R. (1998) Advanced Fenestration and Daylighting Systems. In *Daylighting '98 Conference Proceedings*, Ottawa.

McIntyre, I., Norman, T., Burrows, G., and Armstrong, S. (1989a). Human melatonin supression by light is intensity dependent. *Journal of Pineal Research*, 6(2): 149-156.

McIntyre, I., Norman, T., Burrows, G., and Armstrong, S. (1989b). Quantal melatonin suppression by exposure to low intensity light in man. *Life Science*, 45 (4): 327-332.

Moore, E., (1981). A prison environment's effect on health care service demands. *Journal of Environmental Systems*, 11:17-34.

National Research Council (NRC) (2007). *Green Schools: Attributes for Health and Learning.* Committee to Review and Assess the Health and Productivity Benefits of Green Schools.

National Sleep Foundation (2005). Sleep in America Poll. Internet WWW page at URL< www.sleepfoundation.org/atf/cf/{f6bf2668-a1b4-4fe8-8dla-a5d39340d9cb}/2008POLLSOF.pdf >(Accessed 3.19.08).

Neumaier, A. (1998). Solving ill-conditioned and singular linear systems: A tutorial on regularization. *SIAM Review*, 40: 636-666.

Nickerson, D., (1948). The illuminant in textile color matching. *Illuminating Engineering*, 43: 416-467.

Nieves, J., Valero, E., Hernandez-Andres, J., Romero, J. (2007) Recovering fluorescent spectra with a n RGB digital camera and color filters using different matrix factorizations. *Applied Optics*, 46: 4144-4154.

Osterhaus, W. (2004) Discomfort glare assessment and prevention for daylight applications in office environments. *Solar Energy*, 79(2): 140-158.

Pacific Northwest National Laboratory (1998). Spectrally Selective Glazings. U.S. Department of Energy, DOE/EE-0173, Berkeley.

Papamichael, K. , Klems, J., Selkowitz, S. (1988). Determination and application of bidirectional solar-optical properties of fenestration materials. Technical report LBL-25124, Lawrence Berkeley National Laboratory, Berkeley.

Pilkington NSG Group Flat Glass Business (2008). Glass Manufacturing. . Internet WWW page at URL<http://www.pilkington.com/about+pilkington/company+briefing/glass+manufacturing/floatprocess.htm> (Accessed 4.28.08).

Puleo, S. and Leslie,R. (1991) Some effects of sequential experience of windows on human response. *Journal of the Illuminating Engineering Society*, 20 (1)::91-99.

Rea, M., Figueiro, M., and Bullough, J. (2002). Circadian photobiology: An emerging framework for lighting practice and research. *Lighting Research and Technology*, 34 (3):177-190.

Rea, M., Bullough, J., and Figueiro, M. (2001) Human melatonin suppression by light: a case for scotopic efficiency. *Neuroscience Letter*, 299: 45-48.

Rea, M. (Ed.) (2000). *IESNA Lighting Handbook: Reference and Application (9th ed.)*. New York: Illuminating Engineering Society of North America.

Rea, M. and Ouellette, M. (1991). Relative visual performance: a basis for application. *Lighting Research and Technology*, 23: 135-144.

Romero, J., Garcia-Beltran, A., Hernandez-Andres, J. (1997). Linear bases for representation of natural and artificial illuminants. *Journal of the Optical Society of America*, A 14: 1007-1014.

Richter, F., Kranrich, G., Kuhn, M., Peter, S., Spaeth, Ch. (1998). Cathodic Arc Evaporation—A Versatile Tool for Thin Film Deposition. *Materials Science Forum*, 287-288: 193-198.

Selkowitz, S. (1999). High Performance Glazing Systems: Architectural Opportunities for the 21st Century. In *Proceedings from Glass Processing Days Conference*. Tampere.

Selkowitz, S. and Lee, E. (1998). Advanced Fenestration Systems for Improved Daylight Performance. In *Daylighting '98 Conference Proceedings*, Ottawa.

Simonson, M. and Brozek, J. (1948). Effects of illumination level on visual performance and fatigue. *Journal of the Optical Society of America*, 38: 384-387.

Smith, T and Guild, J (1931). The C.I.E. colorimetric standards and their use. *Transactions of the Optical Society* 33 (3): 73-134.

Snail, K. (1987). Reflectometer design using nonimaging optics. *Applied Optics* 26 (24): 5326-5332.

Swan, J. (1893) *Electrician*, 38. November 10.

Terman, M., Lewy, A., Dijk, D-J., Boulos, Z., Eastman, C., and Campbell, S. (1995). Light treatment for sleep disorders: Consensus report. IV. Sleep phase and duration disturbances. *Journal of Biological Rhythms*, 10: 135-147.

Thapan, K., Arendt, J., and Skene, D. (2001). An action spectrum for melatonin suppression: evidence for a novel non-rod, non-cone photoreceptor system in humans. *Journal of Physiology*, 535: 261-267.

Tikhonov, A., and Arsenin, V. (1977). *Solution of Ill-posed Problems.* Washington: Winston.

Townshend, J., Huang, C., Kalluri, S., DeFries, R., Liang, S., and Yang, K. (2000). Beware of per-pixel characterization of land cover. *International Journal of Remote Sensors*, 21:839-843.

Ulrich, R. (1984). View through a window may influence recovery from surgery. *Science*, 224.

Urbano Gutiérrez, R. and Andersen, M. (2008). Searching and selecting advanced façade technologies as a designer: a new perspective. Submission to *PLEA 2008 conference*, Dublin, October 22-24.

U.S. Department of Energy (USDOE) (2007). 2007 Building Energy Databook. Internet WWW page at URL< http://buildingsdatabook.eren.doe.gov> (Accessed 03.18.08).

U.S. Department of Energy (USDOE) (1998). *Spectrally Selective Glazings,* DOE/EE-0173 .

van Bommel, W. (2006). Non-visual biological effect of lighting and the practical meaning for lighting for work. *Applied Ergonomics*, 37(4): 461-466.

van Trigt, C. (1990). Smoothest reflectance functions I: definition and main results. *Journal of the Optical Society of America*, A 7: 1891-1904.

Veitch, J. (1993). End user knowledge, beliefs, and preferences for lighting. *Journal of Interior Design*, 19: 15-26.

Versluis, R., Prowles, R., Rubin, M. (2007). *Optics version 5.1.01.* Lawrence Berkley National Laboratory. Internet WWW page at URL< http://windows.lbl.gov /software>(Accessed 20.11.07).

Ward, G. (1992). Measuring and Modeling Anistropic Reflection.*Computer Graphics*, 26(2): 265-272.

Watts, M. (2005). Comparing the Energy Conservation Capabilities of Spectrally Selective and Conventional Applied Window Film. *Energy Engineering*, 102 (4):70-78.

Wehr, T., and Rosenthal, N., (1989). Seasonality and affective illness. *American Journal of Psychiatry*, 146: 829-839.

Wibom, R. and Carlsson, W., (1987) Work at visual display terminals among office employees: Visual ergonomics and lighting. In *Selected papers from the International Scientific Conference on Work with Display Units 86.* North Holland: Amsterdam.

Wilkins, A. (1995). *Visual Stress.* Oxford: Oxford UP.

Williams, L. (1966). The effect of target specification on objects fixating during visual search. *Perception and Psychophysics*, 1: 315-318.